SOFT HADRON PHOTOPRODUCTION AT 20 GEV FROM PROTONS

by

Michael John Harwin

A Ph.D thesis submitted to
the University of London for the degree of
Doctor of Philosophy in the Faculty of Science
and Diploma of Membership of Imperial College

March 1986

Imperial College
London

ABSTRACT

During 1980 to 1984 experiments BC72/73 and BC75 were performed at the Stanford Linear Accelerator Centre (SLAC) Hybrid Facility, in which the hydrogen filled bubble chamber was exposed to a linearly polarised 20 GeV photon beam. There was also an experiment (BC76) using a 10 GeV beam. All stages of these experiments were primarily interested in charmed particle photoproduction, however during BC72/73 all hadronic data were recorded to allow studies of photoproduction in general. This thesis presents results on: the performance of the gas Cerenkov counters, elastic and inelastic photoproduction of the $\phi(1020)$ vector meson (including cross sections), and single particle inclusive distributions (pions and kaons) considered within the framework of the Recombination (and Fragmentation) approaches to soft processes. An unexpected charge asymmetry is understood in terms of an extended Recombination model.

ACKNOWLEDGEMENTS

HENP experiments require the efforts of an increasingly larger (multi-national) body of people, numbering over 100 in our particular collaboration, and included: the bubble chamber crew, technicians, scanners and physicists (not forgetting the taxpayer). For fear of offending anyone I might omit, I would like to thank collectively all those who have given help, advice, guidance and friendship during my three and a bit years of postgraduate toil. It's been fun (often), it's been painful (very often), but certainly it's been a privileged opportunity.

Certain members must be singled out for all their patient help and suggestions, and in this respect, I would like to thank my supervisor Dr. Trevor Bacon, Dr. Bill Cameron, and especially Dr. Geoff Hall. Also, I wish to extend special thanks to my fellow 'conspirators' in the 'inclusives subgroup': Dr. George Yost, Dr. Patricia Rankin and Vivian O'Dell.

The general staff and students at Imperial College also receive my gratitude for their discussions and co-operation, in particular: Mark Burchell, Marco Cattaneo, John Dixon, Ian Godfrey, Fereidoun Hamisi, and also Drs. Phil Noon, Chris Seez, Paul Gregory and Tim Axon.

My thanks also to our HEP computing staff: Dr. Ron Campbell, Geoff Fayers, Betty Moynihan, with operators: Charles Beale, Sam Keri, Peter Ruane and Shuaib Sheikh. Also to Janie Coghill, Linda Jones (Group Secretary), and Piera Brambilla.

Grateful thanks are extended to Professor Ian Butterworth for allowing me to join the HEP group, and to the Science and Engineering Research Council for financial support. Also, I would like to thank Queen Mary College, where I earned my B.Sc, and Lincolnshire Education Authority for the funding. Not least I thank my wife, Hilary, for suffering with me, especially since my grant ended and she has supported me financially as well.

Finally, I would like to thank all those who made my visits to SLAC more enjoyable, in particular Karl Bouldin, Peter Dingus, and Dave and Jane Kelsey. This also includes: Oasis burgers, the Dutch Goose, Dragon's Lair, Star Wars, the cast of M*A*S*H (courtesy TV Channel 2), all of which helped to get me through the many midnight to breakfast shifts.

Mike Harwin
Blackett Laboratory
December 1985

CONTENTS

Appendix page

LIST OF FIGURES

LIST OF TABLES

Chapter I

INTRODUCTION AND BACKGROUND

This thesis presents an analysis of data obtained by the SLAC Hybrid Photon Collaboration at SLAC as outlined in the abstract. High Energy Nuclear Physics is a very specialised and large branch of 'pure' research. With the approach of higher energy machines and in view of the recent successes at CERN, it is worthwhile to describe where this thesis fits into the current state of Particle Physics today.

1.1 PARTICLE PHYSICS BACKGROUND

Particle Physics is the study of the ultimate constituents of matter and the nature of the interactions between them. Fifty years ago only the proton and neutron, the electron and neutrino, and the photon were known. Today an ever increasing wealth of particles has been discovered [1]. The electron with its partner the electron-neutrino are now considered to form the lightest doublet in a family of pointlike spin $\frac{1}{2}$ (fermion) 'Leptons'. The last decade has also seen the general acceptance of the Parton Model as more than mathematically convenient. In this model, pointlike 'partons' come in two kinds: fractionally charged quarks with spin $\frac{1}{2}$ carrying properties such as isospin, flavour and colour, and also neutral coloured gluons with spin 1 (see table 1). The familiar particles of nuclear physics such as the proton, neutron, and the pion, are now considered as composites of these quarks and gluons. However, despite huge successes many problems still remain, such as confinement and the apparent pattern of 'xerox copies' of quark and lepton flavours. Over the 1950s and 1960s the proliferation of particles was grouped into 'multiplets' with the recognition of symmetries. The mesons and baryons which interact strongly became collectively known as 'hadrons'.

TABLE 1

Leptons, Partons and Forces

QUARKS		LEPTONS	
name	charge	name	charge
up	$+\frac{2}{3}$	electron	-1
down	$-\frac{1}{3}$	e-neutrino	0
charm	$+\frac{2}{3}$	muon	-1
strange	$-\frac{1}{3}$	μ-neutrino	0
top	$+\frac{2}{3}$	tau	-1
bottom	$-\frac{1}{3}$	τ-neutrino	0

FORCE	QUANTUM/FIELD
Gravity	graviton
Electro-weak -electromagnetic -weak	photon $W^{\pm}$,Z^{0}bosons
Strong	gluon

In 1935 Yukawa advanced the concept of forces by postulating the 'meson' as the carrier of the nuclear force. Present understanding is that the basic constituents interact via the exchange of various fundamental bosons (integral spin) which are the carriers (or quanta) of the four fundamental forces (or fields). On the scale of the universe, gravity may be the most significant, but at energies achievable today it has a very small role in experimental particle physics. It is the Strong force which dominates at short distances for which the theory of Quantum Chromodynamics (QCD) is the most promising. The four forces are believed to be aspects of a Grand Unified Force which would be evident at some very high energy, where their strengths would approach a common value. This is encouraged by the successful unification of the Weak force with Electromagnetism (the theory of which, Quantum Electrodynamics (QED), is the most successful theory we have). This unified electroweak theory is a renormalisable gauge theory (part of the 'Standard Model' SU(3)xSU(2)xU(1) [2]) whose gauge bosons are the three weak bosons W^+,W^-,Z^0 and of course the photon.

1.2 MOTIVATION AND SYNOPSIS

The data analysed in this thesis resulted from the interactions between protons in a bubble chamber and a photon beam. Even though the photon is the propagator of the electromagnetic force it exhibits the remarkable property of interacting as if it had two components: a weaker pointlike component and a dominant hadronic component [3]. Crucial to an understanding of photoproduction are the concepts underlying the hypothesis of Vector Meson Dominance (VMD) [4]. During high energy interactions the photon (with $J^P = 1^-$) can couple directly to a vector meson (with $J^P = 1^-$) and then interact as that meson. The hadronic component of the photon can then be regarded as a mixture of vector mesons: ρ,ω,ϕ ...etc. The production of heavier mesons, neutral strange particles, and the charmed mesons in this experiment have already been reported and in general are not discussed in this thesis.

ϕ production is particularly interesting, not least because of the almost pure strange quark content of the ϕ, but also because the proton contains no strange valence quarks. Thus ϕ photoproduction must arise from the photon interacting as a vector meson (ϕ,ϕ'), or from the proton sea, or less likely as a decay product. Recently, renewed and intense interest has been focussed on this familiar particle because of the possibility of resonant $\phi\phi$ states being a signature for those exotic states of nature dictated to exist by QCD - glueballs. Also the recently found $\phi\pi$(1970) signal is believed to be the charmed F meson, previously believed to have been at about 2020 MeV/c^2. The Cerenkov counters in this experiment which provided charged particle identification presented a good opportunity to study the ϕ 'inclusively'.

Since the 1970s the investigation of particle interactions has been dominated by the 'inclusive' approach arising from certain practicalities. At high energies the final state is quite complicated with many particles produced (typically 18 hadrons at the ISR (CERN) $\sqrt{s}$=63GeV) some of which may miss any detectors set up. The 'exclusive' approach of looking at specific final states was therefore difficult and so a selective procedure was desired. The convenient method proposed was to regard reactions as A + B --> C + X where C represents the observed particle(s) and X represents everything else (not necessarily observed). This 'inclusive' approach can then be described using either the variables: s, t, M^2 , where s and t are the familiar Mandelstam variables, and M^2 the missing mass squared (figure 1); or we may use s, Xf, Pt, where Xf and Pt are Feynman-x and transverse momentum.

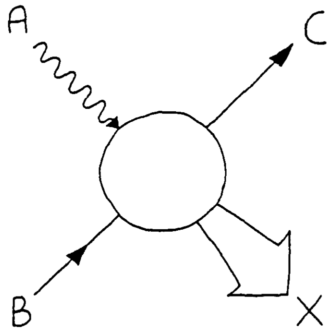

$$S = (P_A+P_B)^2 = (P_C+P_X)^2$$
$$t = (P_C-P_A)^2 = (P_X^2-P_B)^2$$
$$M^2 = (P_A+P_B-P_C)^2$$

Figure 1: Inclusive Approach

The major theoretical stimulus for the study of inclusive reactions came from Feynman (1969)[5], who predicted that cross sections would 'scale', i.e, become a function of Xf and Pt and not of the energy $\sqrt{s}$ directly. This scaling phenomenon is equivalent to saying that the quarks appear pointlike (at present energies). It is not known whether very much higher energies would reveal a substructure to the quarks (preons?) where another level of scaling may set in. This would continue the progressive levels of scaling witnessed from atomic physics down to 'elementary' particles as the distance scale probed has shortened (ie, higher energy). It has become conventional to study single particle inclusive distributions mainly in the variables Feynman-x and sometimes rapidity y.

With the success of the parton approach to high Pt (hard) scattering processes, its possible applications to soft processes (low Pt) at high energy prompts investigation. This area has been traditionally the realm of Regge Theory where perturbative QCD cannot be applied because of the low Q^2 (ie, four-momentum transferred squared $\equiv t$). Though this important realm of particle physics is not much emphasised today, during the last few years there has been a great deal of activity with interest concentrating on explaining fast hadron distributions at low Pt. However, the field is somewhat confusing owing to a variety of very different dynamical models all claiming success. These include: the quark fragmentation model (Andersson et al 1977), the recombination/valon model (Das and Hwa 1977), the quark chain model (Cappella et al 1979), and the dual topological unitarisation approach (Cohen-Tannoudji et al 1980) [6]. Particles with low transverse momentum ($Pt<1.0$ GeV/c) dominate the final states in our experiment and thus puts this analysis within the realm of soft processes.

The synopsis is now outlined. This chapter briefly describes the material in this thesis and how it fits into the overall picture of particle physics today. Chapter two details our experimental apparatus at the SLAC Hybrid Facility. The processing of the enormous amount of data (both film and magnetic tape) is the subject of chapter three. Chapter four concentrates on the gas Cerenkov counters, which became my responsibility during BC75. The theory relevant to photoproduction and the results in the remaining chapters is presented and discussed in chapter five, including the models of Fragmentation and Recombination. Chapter six then concentrates on the production characteristics and cross sections for elastic and inelastic ϕ photoproduction. Chapter seven describes studies of pion and kaon inclusive distributions and in particular an unexpected charge asymmetry is discussed in terms of an extended recombination model.

1.3 SPECIAL CONSIDERATIONS FOR OUR EXPERIMENT

The BC72/73 experiment was performed at the SLAC Hybrid Facility situated near Stanford in the San Francisco Bay area of California (near to the San Andreas Fault!). Though it was intended to study photoproduction in general, its main motivation was the study of photoproduced charmed particles. BC75, the extension and improvement of the experiment, was designed solely to enlarge the charm sample already obtained.

A unique feature of our experiment was the use of a high resolution camera which enabled the detection of charged and neutral charm decays. A beam energy of 20 GeV (considered 'low') meant that event multiplicities were small and the forward cone of charged particles wide so that the majority of decays seen were topologically unambiguous.

The weak decays of heavy quarks have been studied extensively in the last few years; an effort stimulated mainly by the work done by the DELCO(1980) and the Mark II(1981) collaborations [7]. They reported lifetimes for the charged and neutral D mesons which were not equal - upsetting the early light quark Spectator Model. It is now supposed that two types of mechanism dominate the decays of D mesons [8] (see figure 2):

1. the spectator picture, in which the charm quark decays independently of any other quarks present, and
2. non-spectator diagrams in which the other quarks couple to the decaying quark, for example annihilation.

At the Cabibbo-favoured level the spectator mechanism affects D^0 and D^+ decays equally whereas the non-spectator mechanism only applies to D^0 decays. Therefore, the deviation from unity of the charged to neutral lifetimes ratio is a measure of the relative contributions of the two mechanisms.

Our experiment (BC72/73/75) measures lifetimes of $(8.6\pm1.3\pm^{0.7}_{0.4})$ x 10^{-13}s for the charged D and $(6.1\pm0.9\pm0.3)$ x10^{-13}s for the neutral D giving a ratio of $1.4\pm0.3\pm^{0.2}_{0.1}$ in line with the spectator picture dominating.

During the autumn of 1983 the experiment also ran as BC76 with a lower beam energy (10.6 GeV). This was to search for an enhancement in the charm cross-section predicted by Rubinstein and Stodolsky in 1978. More precisely this was to have been of several microbarns for $\gamma p \rightarrow$ charmed baryon + charmed meson somewhere a few hundred MeV above threshold. (Note that our measured charm cross-section at 20 GeV is only $62\pm^{15}_{10}$nb). The cross-section measured showed no such enhancement and this result has now been published [9].

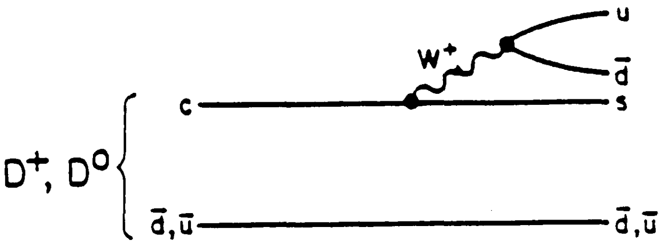

SPECTATOR

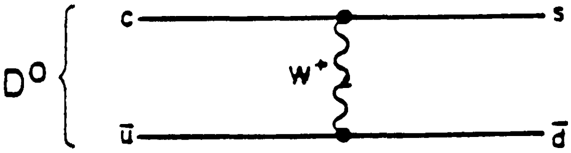

EXCHANGE

Figure 2: Spectator and Non-Spectator Decays

Chapter II

EXPERIMENTAL DETAILS OF THE SLAC HYBRID FACILITY

2.1 INTRODUCTION

Approximately 100 physicists from 18 institutions spread over Israel, Japan, the United States and Great Britain formed the SLAC Hybrid Photon Collaboration and performed the experiments BC72/73 and BC75. The initial experiment completed data taking in 1982 and has published results on charmed particle lifetimes, cross-sections, and production mechanisms along with other hadronic topics [10]. Results from BC75 have been combined with the earlier results and submitted for final publication.

Briefly our experiment was arranged such that a linearly polarized 20 GeV photon beam was incident on the SHF 1m hydrogen filled rapid cycling bubble chamber. This was both the target and the main detector, and was equipped with a special high resolution optics system (HRO). In front, or 'upstream' of the bubble chamber, were the main beam monitors comprising of two devices: a so-called quadrant detector and a pair spectrometer. Downstream were several electronic detectors: four sets of multi-wire proportional counters (PWCs), two Cerenkov counters, and a lead glass electromagnetic calorimeter. The bubble chamber cameras were 'triggered' using information from the PWCs and/or the Lead glass wall. The overall system was continually improved during the four years of operation of BC72/73 and BC75.

2.2 THE PHOTON BEAM

2.2.1 The SLAC Electron Beam

The Stanford Linear Accelerator (or LINAC) generated an electron beam accelerated to 29.5 GeV by operating in what is known as its 'SLED 1 mode' [11]. Acceleration formed bunches (or pulses) of electrons each lasting about 100ns and containing about 10^{11} electrons (supplied to our experiment along beamline 27).

The electron beam was then aimed at the bubble chamber while being steered towards an interaction region. Here it intersected a laser beam head-on such that (Compton) backscattered photons formed a beam incident on the bubble chamber. This was achieved using a series of collimators, bending dipole magnets, and focussing quadrupole magnets positioned along the beampipe (shown schematically in figure 3). Some brief examples (precise details are not given) of the various tasks performed by the components are listed:

a) C1, D1, Q1, Q2, SL1, Q3, D2 (refer to figure) filtered through electrons with the correct energy;

b) A1, A2 (orthogonal dipole magnets) steered the electron beam so as to intersect the laser beam;

c) A3, A4, Q4, Q5 also steered and focussed the beam to ensure the photon beam was incident on the bubble chamber;

d) A5, A6 helped to minimise the bremsstrahlung and synchrotron contamination to the photon beam;

e) and finally, a series of magnets (permanent magnets for safety reasons) deflected and dumped the electron beam.

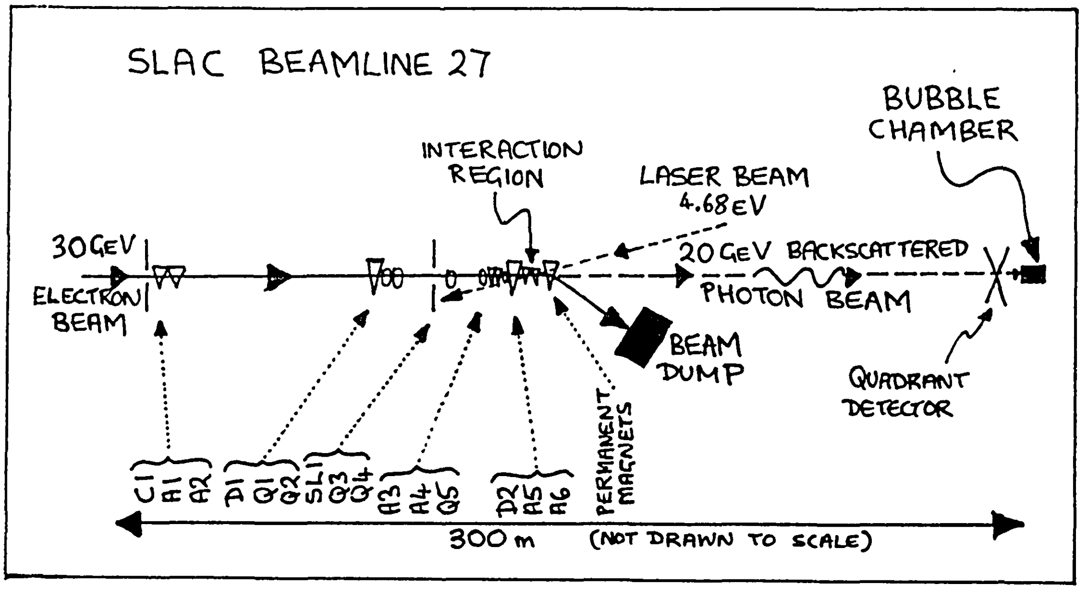

Figure 3: Beamline 27

2.2.2 The Laser Beam

The initial source of photons (at 4.68 eV) was a neodymium doped yttrium aluminium garnet (Nd:YAG) solid state pulsed laser followed in series by two harmonic generating crystals (See figure 4).

The laser, which was required to generate intense (~75mJ) short pulses to ensure an acceptable backscattered photon beam, had its lasing action controlled by the 'Q-Switching' technique with a system of thin film polarizers. In this laser the Q-Switch itself was a Pockels Cell: an electro-optical crystal which could polarize light depending on an applied voltage. The laser output was controlled by the orientation of the $\frac{1}{4}$ wave plate resulting in ~75% vertical and ~25% horizontal polarized light. The polarizer reflected (or 'coupled out') only the

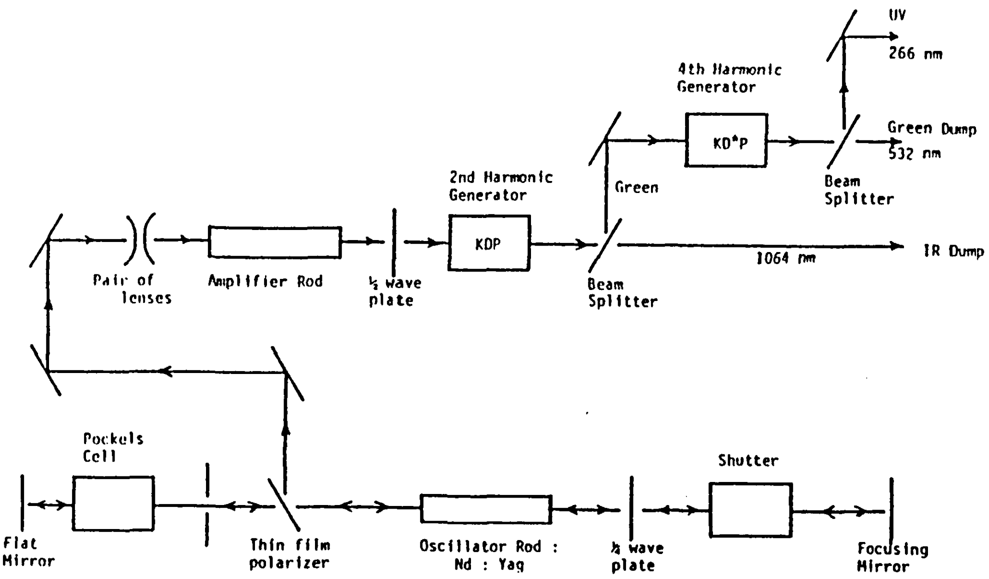

Figure 4: Laser Optical Cavity and Harmonic Crystals

vertical component, and therefore, while pumping the ND:YAG laser rod the horizontal component passing through was shifted to vertical by the Pockels cell, and so prevented from returning and stimulating further emission. This allowed the population inversion to build up such that when the voltage on the cell was removed lasing took place in a burst and a beam pulse emerged.

The output infrared light (λ=1064nm) was first amplified and then 'frequency doubled' to green (λ=532nm) by passing through the first crystal, and then frequency doubled again to ultraviolet (λ=266nm) by passing through the second crystal. Each crystal converted about one third of the incident power into the doubled frequency. 'Frequency doubling' can be understood as an atom absorbing two incident photons before re-emitting the excitation energy as a single photon.

The laser was run at a repetition rate of 10Hz and later 12Hz to match the bubble chamber and generated about 10^{17} 100% linearly polarized photons per pulse. Each pulse was directed 60m upstream where it intersected the electron beam over a crossing angle of two milliradians. The kinematics of this collision are presented in Appendix A. Once collimated, the backscattered photons were the beam for our experiment.

2.2.3 The Photon Beam

The energy spectrum of this backscattered photon beam was measured using a pair spectrometer and is shown in figure 5 for BC72/73 [12] with a similar spectrum for BC75.

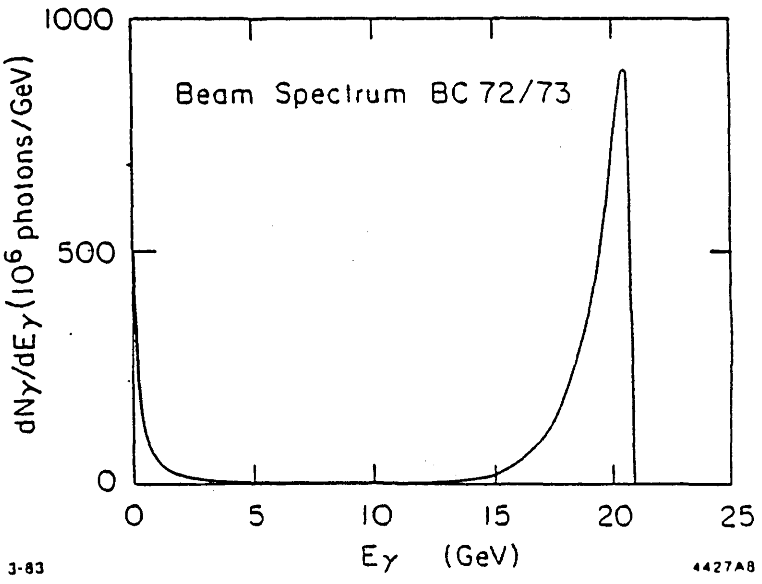

Figure 5: Photon Beam Spectrum

The maximum energy was 20.5 GeV peaking at 19.6 GeV with less than 10% of the photons reaching the bubble chamber having energies less than 15 GeV. The few events above the peak are probably bremsstrahlung from the LINAC electron beam. The range 3 - 15 GeV was measured using events fitted to $\gamma p \rightarrow p\pi^+\pi^-$ whereas below 3 GeV e^+e^- pairs in the bubble chamber were used. The beam spectrum originated as a result of a spread in the electron energy, the electron/laser beam crossing angle, and the collimator.

The photon yield varied throughout - typically about 25 photons per pulse for BC72/73, and 25 - 30 for BC75. The beam had a final linear polarization of about 52% with the axis of polarization alternated between vertical and horizontal.

2.3 THE SLAC HYBRID FACILITY

The SHF can conveniently be described in three sections: the upstream system, the SLAC 1m bubble chamber, and the downstream system. The changes made during the running of BC72/73 and BC75 were aimed primarily at improving the resolution achieved with the high resolution camera. The most significant of these will be described below.

2.3.1 The Upstream Beam Monitors

The upstream detectors consisted of a quadrant detector and a pair spectrometer and were used to monitor the beam. A third device, the beamstop counter, also monitored the beam but was the final detector positioned downstream.

The quadrant detector consisted of a tungsten cylinder with a central 3mm collimating hole. Embedded in the tungsten were four

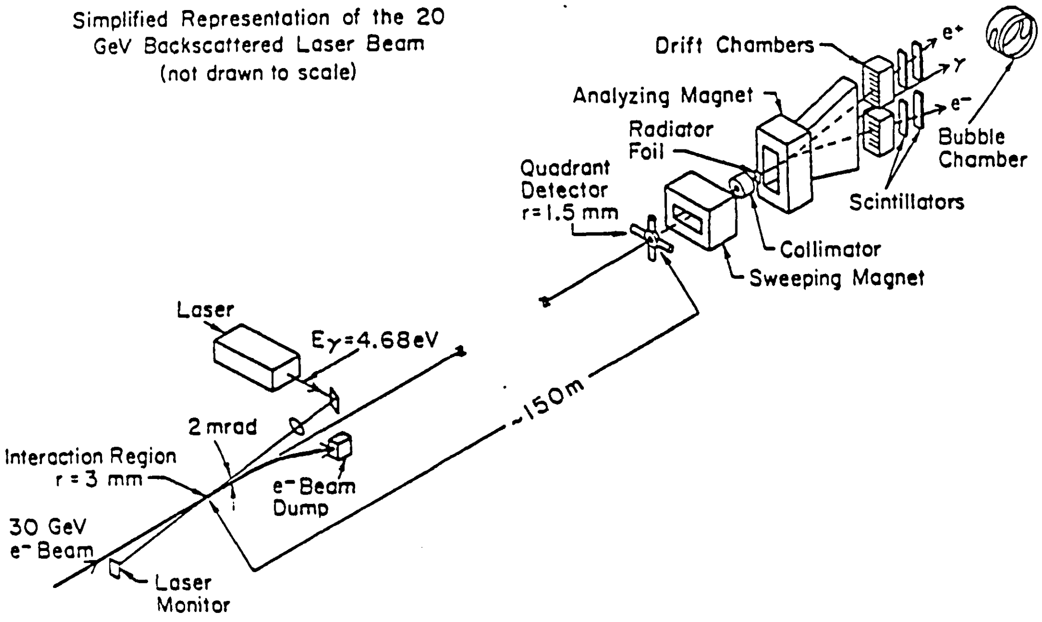

Figure 6: The Upstream System

scintillator counters orthogonal to the beam. This detector served a dual role. Firstly, the majority of backscattered photons were absorbed by the tungsten producing electromagnetic showers. By aiming to balance the signals in the scintillators the beam could be continuously and automatically steered correctly. Secondly, the collimating hole shaped the beam spectrum and the beam size of approximately 3mm diameter.

The pair spectrometer monitored both the beam spectrum and the beam flux. A thin copper foil placed in the beam path converted about 1% of the photons into e^+e^- pairs. A bending magnet then allowed the energy of the e^+e^- pairs to be measured via deflection into a set of drift chambers while information on the intensity came from the scintillators [12].

Alternating layers of lead and lucite formed the beamstop counter which was viewed by a phototube. The electromagnetic showers produced consequently generated Cerenkov light dependent on the beam's intensity.

2.3.2 The Bubble Chamber and High Resolution Camera

In brief, the bubble chamber technique [13] is to require the liquid hydrogen to be 'superheated' when the photon beam enters the chamber. The passage of a charged particle initiates the formation of gas bubbles by ionization which then grow when the 'overpressure' is removed. Trajectories of charged tracks are then rendered visible by the trail of bubbles produced. After these bubbles have grown sufficiently the tracks can be photographed with an array of cameras. To aid the detection of charm decays our bubble chamber was run with a high expansion ratio and at a temperature of 29K rather than the more normal 26K. This gave a slower rate of bubble growth leading to a bubble size of about 50μm after 150μs, and also a higher bubble density of about 70 bubbles cm^{-1} compared with 15 cm^{-1} under normal operation. This placed speed constraints on the Trigger.

The normal stereo optics system of the bubble chamber consisted of three cameras (125mm,f22) which were operated with a flash delay of 3.5ms. These three strategically placed views allowed the tracks in an event to be geometrically reconstructed when the film was measured. In addition, a high resolution camera (HRO)[14] was centrally mounted to enable the direct observation of charm decays at the HRO flash time (150μs for BC72/73). BC72/73 had a single 360mm lens fitted (Schneider Componon S) which at f11 with a ±6mm depth of field achieved a resolution of about 55μm. For BC75 this single lens was replaced by a pair of Nikon Apo-Nikkor 610mm lenses which for a depth of field of ±2mm gave a resolution of about 40μm close to the diffractive limit of 30μm for a depth of field of ±2mm.

The bubble chamber itself was improved towards the end of BC72/73 by replacing the glass window with a new thicker window. This reduced the amount of turbulent hydrogen through which pictures were taken. The reduced volume of hydrogen allowed for better control of the chamber operating conditions. A shutter was also introduced to prevent light from the secondary flashes entering the HRO camera.

A large electromagnet surrounded the bubble chamber to provide momentum determination from track curvature; at first with a field of 26kG, but later with a field of 18kG for reasons of economy. However, despite the 4π solid angle acceptance of the bubble chamber, its finite length limited the momentum resolution for higher momentum tracks especially if the production vertex occurred towards the downstream end of the chamber. This was partially alleviated by the measurements made by the proportional wire chambers.

2.3.3 The Downstream Detectors

The downstream system served two very important functions. Firstly, to provide data for an on-line decision to trigger the bubble chamber cameras, and secondly, to provide extra information on particles produced in an event in the bubble chamber. All the detectors were made insensitive to the background e^+e^- pairs in the central (vertical) region, (pair production is about 200x more frequent than hadronic events).

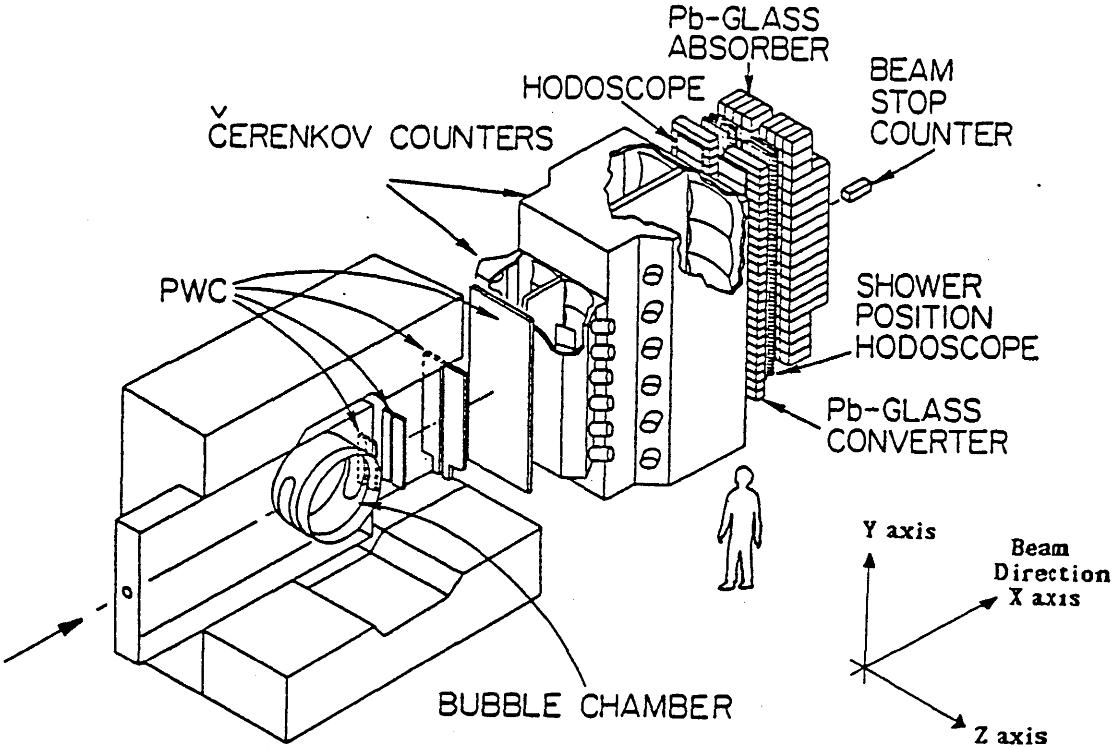

Figure 7: The SLAC Hybrid Facility

Directly behind the bubble chamber were four multi-wire proportional chambers. Each of the first three chambers (α,β,γ) contained three planes of wires (horizontal (z), vertical (y), diagonal (u)) which formed a 3:4:5 triangle. The fourth chamber δ was a prototype and was removed before BC75. Hits in the z planes (non-bend plane of the magnetic field) were used to provide a trigger for the cameras. Offline the hit information was used to improve the momentum measurements of tracks extrapolated from the bubble chamber after film measurement. The momentum resolution of these 'hybridised' tracks was determined to be:

$$\sigma(p)/p = \surd(\ (0.008)^2 + (0.00085p)^2\ )\ \text{(p in GeV/c)}\ [15]$$

Following behind the PWCs were two atmospheric gas threshold Cerenkov counters. During BC72/73, C1 and C2 were filled with Freon-12 and Nitrogen respectively. This allowed partial particle identification above 3 GeV (see table 2). To lower the pion threshold for BC75 both counters were filled with Freon-114. The performance of the Cerenkov counters during BC72/73 and BC75 will be discussed in detail in chapter four.

Next, a 'Lead glass wall' built of: a filter hodoscope, a lead shield, an active converter, vertical and horizontal hodoscopes, and an array of lead glass absorber blocks provided shower detection and π^0 reconstruction[16] (see figure 8) and also a fast trigger.

TABLE 2

Cerenkov Threshold Momenta

	C1 (BC72/73) (FREON-12)	C2 (BC72/73) (NITROGEN)	C2 (BC75) (FREON-114)
electron	0.011 GeV/c	0.021 GeV/c	0.0096 GeV/c
muon	2.3	4.3	1.997
pion	3.0	5.7	2.637
kaon	10.6	20.2	9.327
proton	20.2	38.3	17.726

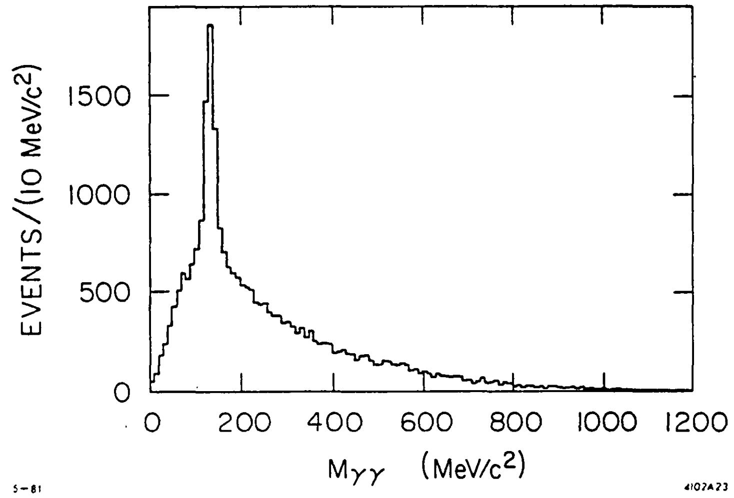

Figure 8: $\gamma\gamma$ Mass Spectrum

2.4 THE TRIGGER

Bubble chamber experiments can be triggered by events or untriggered (ie, pictures taken whenever the beam pulse arrives). Untriggered experiments should yield an unbiased sample of the total cross-section. At 20 GeV the total hadronic cross-section from photoproduction is 115 ± 2 μbarns [17] and therefore in our bubble chamber fiducial volume of 75cm length the probability of a hadronic event is about 0.0003 (since in a hydrogen bubble chamber 1 barn ≅28cm). Consequently, running at a typical flux of 30 photons per pulse would yield 1 hadronic interaction every 100 pictures - very quickly an unmanageable amount of film! Coupled with the nearly ½ second deadtime after each picture the decision to trigger the cameras was an obvious one. In general one hadronic event occurred about every four frames.

The hardware decision to trigger picture taking was made using the results from two independent triggers OR-ed together: the slower PWC trigger, and the faster Lead glass trigger. The major constraint on the PWC trigger was the time available to make a decision. This arose from the bubble growth rate and the required HRO flash time for the necessary bubble size. In contrast, this presented no problem to the Lead glass trigger since it used fast analogue electronics. To speed up the PWC algorithm it was run on a set of IBM 168/E microprocessors [18]. The time available was reduced by about 30μs for BC75 since 40μm bubbles were to be recorded. This required a dedicated hardware line-processor (built at Imperial College [19]) to replace the software algorithm (written at IC).

The PWC trigger condition was satisfied if a set of 3 z hits (ie, in the non-bend plane of the magnetic field) was found to be compatible with a track originating from within the fiducial volume of the bubble chamber (see figure 9). This needed about 100μs in contrast to the Lead glass trigger which was available in 2μs. The Lead glass required a signal corresponding to an

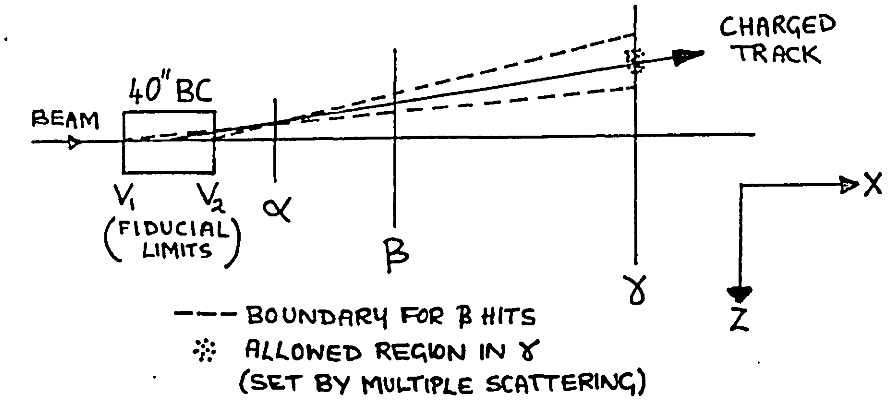

Figure 9: PWC Trigger Strategy

energy deposition of more than 2 GeV in the total absorber blocks or 0.8 GeV in the active converter. Both the PWCs and the Lead glass wall were desensitised in their central vertical regions. The width of this 'dead region' essentially controlled the trigger rate. In addition, every fiftieth frame was taken untriggered (ie, whether a trigger was requested or not). This enabled the triggering efficiency to be calculated in an unbiased manner; for instance, as a function of topology (table 3).

TABLE 3

Hadronic Trigger Efficiencies (BC72/73)

Prongs	PWC Trigger	Pb Trigger	Combined Trigger
3	59±4%	89±3%	92±2%
5	71±4%	90±3%	98±1%
7+	76±6%	71±5%	95±3%
Overall	66±3%	86±2%	95±1%

2.5 DATA ACQUISITION

The acquisition of data and recording on magnetic tape was controlled by a Data General NOVA 4/X computer. Coupled to this as 'slaves' for BC72/73 were three 168/E IBM microprocessors, and for BC75 a dedicated hardware line-processor. During actual data taking runs, programs on the NOVA ran in a Foreground/Background mode. The Foreground program constantly controlled critical functions such as recognising a beam pulse arrival, accepting a trigger, firing the flashes, advancing the film, writing to tape, and avoiding another trigger while one was being processed. The Background program allowed physicists on shift to monitor the performance of the equipment on-line. It provided a menu of tasks such as resetting any high voltages which may have drifted from their preset values. However Background tasks interrupted and slowed the Foreground. If necessary the Background allowed interaction with the Foreground by means of a special area of memory known as the communications array.

Chapter III

DATA PROCESSING AND DST PRODUCTION

3.1 INTRODUCTION

The raw data existed in two complementary forms. Firstly, bubble chamber photographs consisting of the three normal views (70mm film) and the high resolution views (35mm film), and secondly, the NOVA magnetic tapes containing information from the downstream detectors. BC72/73 had only one HRO view whereas BC75 had two. The film was developed at SLAC and then distributed amongst the collaboration together with copies of the NOVA tapes. The long and laborious processing chain necessary to transform this raw data into a multi-volume Data Summary Tape (DST) for physics analysis differed from laboratory to laboratory and also during the lifetime of the experiment. The general procedures will be described with emphasis on those used at Imperial College.

3.2 ORDINARY HADRONIC EVENTS (BC72/73)

All the 70mm film was scanned twice for hadronic interactions by specially trained people. Based on the information as to whether events were found on the first scan and/or the second scan the combined scanning efficiency for finding multi-prong hadronic interactions was found to be (99±1)%. These hadronic interactions were then scanned twice on the HRO film to find charm candidate events. An event then followed one of two processing chains depending on whether it was regarded as an ordinary hadronic event or a possible charm event.

Until Spring 1982 Imperial College used a machine called a Hough Powell Device [20] to measure events on the 70mm film. The output from this machine and (later others) was transformed into the format necessary for the geometry reconstruction program HYDRA Geometry [21]. The output from HYDRA consisted of the vertex co-ordinates and the mass dependent parameters momentum (1/p), dip, and azimuthal angles (λ,ϕ) for each track together with errors and correlations.

In the next stage called 'hybridisation' bubble chamber measurements were combined with the information from the downstream detectors using the HYBRID program [22]. This involved projecting or 'swimming' fast tracks through the magnetic field out of the bubble chamber and through the downstream system. The hit information in the PWCs was then used to increase the accuracy of the track parameters determined from the bubble chamber measurements by means of a joint fit to both measurements.

With the best estimates of the various track parameters the events were then run through a kinematic event fitting program called GRIND [23]. This attempted possible permutations of fits to the event topology which conserved four-momentum and relevant quantum numbers (eg, for 3 prongs $\gamma p \rightarrow p\pi^+\pi^-$ and $\gamma p \rightarrow pK^+K^-$ were always attempted). The data record now existed as an incomplete DST and required only results from the Cerenkov counters, the Lead glass wall and ionization information. The ionization for low momentum tracks (<1.5GeV/c) was also predicted by GRIND for e,π,K,p hypotheses. It was therefore possible to identify some tracks by examining the HRO film and comparing their ionization with that of a minimum ionizing track or even by counting bubbles. However, dipping tracks, difficulties in estimating track densities, and a varying photographic quality made this process arguably somewhat subjective and casts doubt on its accuracy and consistency.

Finally, book-keeping was very important to ensure that events did not go 'astray' during processing. To this end the measurement status of each event was recorded on a 'masterlist'. From this re-measurement lists were drawn up for those events which failed to be reconstructed after measuring. At Imperial College third re-measures were done on a semi-automatic machine called SWEEPNIK [24]. These lists also made the calculation of quantities such as scanning efficiencies easier.

3.2.1 Kinematic Event Fitting

Since fitted events are used later in this thesis it is worthwhile to present here a brief qualitative description of the fitting program GRIND which was originally written in the 1960s at CERN specifically for bubble chambers. Given a geometrically reconstructed event it had to search for possible final states consistent with explaining the event and to test each hypothesis by a statistical fit. The calculation of a χ^2 probability indicated the likelihood of a fit and had to pass a preset value to be acceptable and included on the DST.

Obviously finding a successful fit would be most likely if everything were known, ie, the mass and momentum-vector of each and every particle. Unfortunately the measurement of the momentum-vectors may not be complete, for instance due to short tracks, or not known at all due to missing neutrals. The masses are not measured of course, but usually there is a limited number of possible mass assignments to a track. Typical measurement errors are shown in figure 10.

The basis of any complete description of an event has to be the conservation of energy and momentum. In general however, the raw measurements will not satisfy these constraints. The fitting procedure, which uses a least squares technique, computes corrections (if possible) which have to be applied to the measured values for the event hypothesis to become physically possible. These corrections, which have to be small to minimise the χ^2, are found by varying track parameters within their respective errors. This is done not with the momentum components Px,Py,Pz (which have to be calculated) but with the measured variables 1/p, λ and ϕ since these have nearly gaussian errors. At the level of 'fine tuning' the errors on the fitted quantities are checked and adjusted such that the 'Stretch' (or 'Pull') distributions had the correct form, ie, gaussian, centred on zero with unit standard deviation (See [25]).

The resulting fits are of various grades depending on the number of kinematic quantities assumed unknown. If everything is known (ie, resultant $E,1/p,\lambda,\phi$) then we have a 'four constraint fit': a 4C fit. If there are no missing neutrals and no unmeasured tracks then since in our experiment the beam energy is the only unknown (its direction is well known), we have a '3C fit'. A '2C fit' is possible if, for instance, all directions are measured but at least one track has no 1/p measurement. If one particle is missing or unmeasured then all the quantities are unknown and the fit becomes a '0C fit' or unconstrained. In the roll range 300 to 2531, where all events were recorded on the DST, 26198 3 prong events (22% of the 3 prong data) had successful 3C fits, and 10707 5 prong events (11% of the 5 prong data). The analysis in this thesis uses 3C fits to: $\gamma p \rightarrow p\pi^+\pi^-$, $\gamma p \rightarrow pK^+K^-$, $\gamma p \rightarrow pK^+K^-\pi^+\pi^-$.

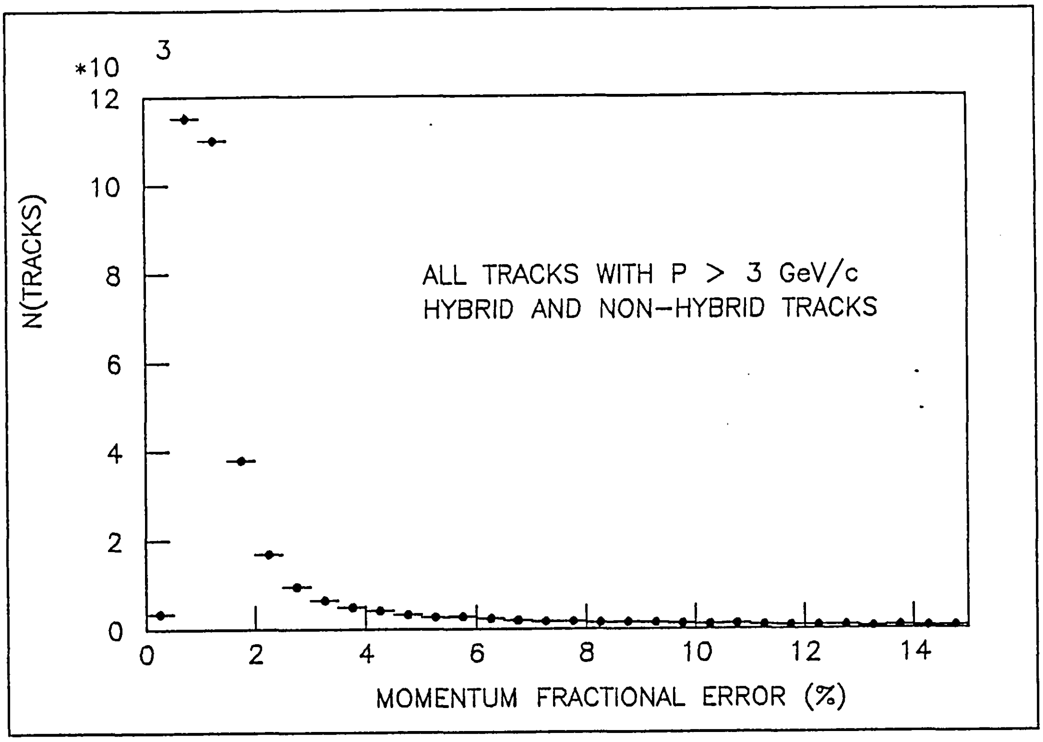

Figure 10: Track Measurement errors

3.3 CHARM EVENTS (BC72/73)

Charm candidates were searched for on the HRO film and when found were subject to a set of cuts. Originally a 'charm box' was defined for the scanning table in which over 90% of the charmed decays were expected to occur, based on assumptions about the kinematics of a charmed particle produced at 20 GeV [8]. Scanners searched for a secondary vertex and/or a kink within this charm box, and any such events found had a HRO print made directly from the table for 'scrutiny' by physicists. After measurement, decays consistent with strange were removed. Our famous 'Christmas Card' event is shown as figure 11.

3.4 CHARM EVENTS (BC75)

As already mentioned BC75 was interested solely in charm events and so little 'ordinary' event processing occurred; indeed this had been the case since the spring 1982 run of BC72/73. With the improved high resolution camera the charm search technique was modified: the charm box became a charm semi-circle. At Imperial College [26] this had a radius of 30cm on the scanning table where the space to table magnification was about x20. Charm candidates were now measured on I.E.P machines (Instruments for the Evaluation of Photographs, affectionately known as Bertha and Willie). The event measurements were still run through the programs HYDRA and HYBRID, after which cuts were made on decays consistent with being strange, but no GRIND or ionization processing was done at Imperial.

Experience gained during BC72/73 allowed the scanning procedures to be updated. Only the HRO was scanned with two independent scans followed by a third check scan. For BC75 as a whole 35% of the film was scanned three times. The scanning efficiency for finding decays was then calculated using a maximum likelihood method (which had advantages over the method previously used [27]).

At Imperial College appproximately 120 BC75 rolls were scanned (62 from the spring run, 61 from the fall, with 850 pictures per roll) resulting in 1210 candidates (651+559) all of which went through a streamlined processing system [26] resulting in a DST, of which 4 proved to be charm events. The combined charm sample for the collaboration is 136 events after cuts [28].

3.5 DATA SUMMARY

The data analysed in this thesis has been collected over seven runs during 1980 to 1984 and constitutes the combined experiments of BC72/73 and BC75 together with BC76, which were performed by the SLAC Hybrid Photon Collaboration. A summary of the data recorded is listed in table 4. The data were triggered using the PWCs and/or the Lead glass wall resulting in the following distribution of topologies: 1:3:5:7:9:11+ prongs occurring 4.4%:42.6%:34.4%:14.8%:3.5%:0.35% of the time. The trigger efficiencies are listed in table 3. Scanning efficencies were typically 97%:98%:99% for 3:5:7+ prongs, with typically 98%:98%:97% measuring efficiencies (SLAC).

The bubble chamber with its 4π acceptance and high resolution camera enabled the direct observation of charm decays. The PWCs improved momentum measurements. Partial charged particle identification came from the Cerenkov counters, with π^0 and photon detection being provided by the Lead glass wall. The data processing involved geometrical reconstruction, hybridisation, and kinematical fitting. During analysis a fiducial volume cut was imposed on the production (or primary) vertex where the fiducial volume was that volume defined for measurement within the chamber. The experimental Sensitivity has been estimated to be 2.7 ± 0.1 ± 0.2 events per nanobarn where the first error is statistical and the second systematic [10.5, 16.2]).

As a final comment, I wrote and maintained a software package in the interests of speed and convenience for the analysis of DST subsets at Imperial College [29].

TABLE 4

Summary of Data Recorded

Run	Roll range	Pictures Taken	Events on DST
Summer 1980	89- 216	92000	8384
Autumn 1980	300- 810	445000†	60463
Spring 1981	900-1620	636000†	118171
Autumn 1981	1622-2531	806000	101019
Spring 1982	2550-3024	429000	19016
Total (BC72/73)		2408000	307053
Spring 1983	4000-4796	625000	4580
Autumn 1983	4800-5580	600000	4650
Total (BC75)		1225000	9230‡
Total (BC76)	7000-7126	98000	2796§

1) † including rolls 217-276 and 811-850 at energy 13 GeV
2) polarization: rolls 1152-1620 vert-, 1622-2531 horizontal
3) magnetic field: rolls 89-1620 26 kG, 1622-7126 18 kG
4) general photoproduction: rolls 300-2531
5) ‡ from 310000 hadronic events
6) § mostly 3 prongs, no charm events were found

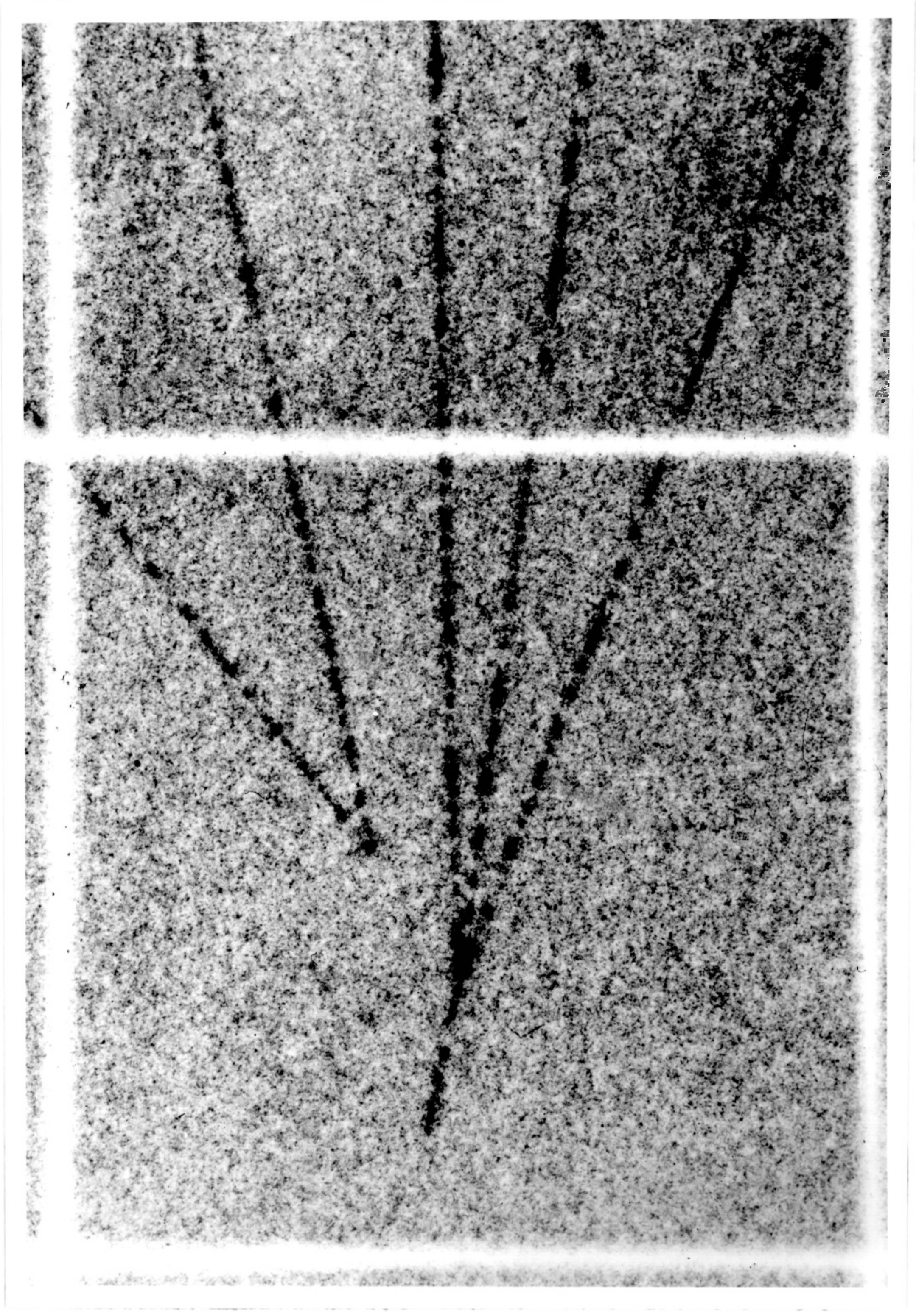

Figure 11: The "Christmas Card" charm event
The superimposed grid represents 1mm spacing.

Chapter IV

THE GAS THRESHOLD CERENKOV COUNTERS

4.1 CERENKOV RADIATION AND THRESHOLD COUNTERS

All detection methods can be described as either destructive or non-destructive depending on whether the detected particles are destroyed in being observed. All neutral particles are detected by destructive means, whereas the electromagnetic interaction allows charged particles to be detected in a non-destructive manner. Cerenkov radiation [30] provides a non-destructive technique which is particularly useful in the relativistic range where it is most sensitive to particle velocity, and where the traditional methods of particle identification at low energies (<1GeV), such as time-of-flight counters, or simply dE/dx measurements coupled with a momentum measurement, have become increasingly difficult.

For thresholds at relativistic energies, the Cerenkov effect is best employed in a gas counter because the refractive indices of gases are much lower than those of liquids and solids and therefore lead to correspondingly higher threshold energies. However, a consequence of this is that the major limitation to the gas counter becomes the very low yield of light, usually so low that the photoelectron pulses in the photomultiplier cannot be distinguished from its 'dark current'†. For this reason counters normally have their phototubes positioned out of the particle line-of-flight and are operated in coincidence with others. The effect of dark current noise is negligible in our counters due to a narrow time gate (~100ns) on the ADCs.

Tamm and Frank (1937)[31] developed a classical theory of Cerenkov radiation based on the idea that if a charged particle moves through a medium faster than the velocity of light in that medium then it will emit radiation along a conical wavefront at an angle determined by its velocity and the refractive index of of the medium. The expression $\cos(\theta)=(\beta n)^{-1}$ is known as the 'Cerenkov relation'. A little later a quantum theory was developed by Ginsburg (1940)[31].

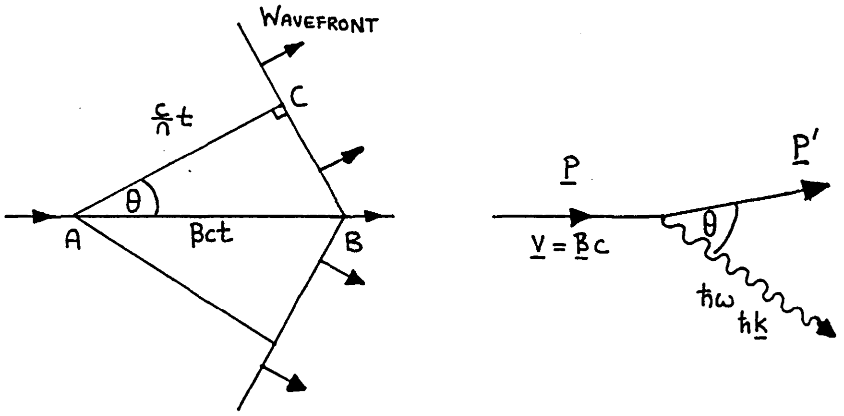

Figure 12: Cerenkov Radiation (Classical and Quantum)

The fundamental equation for radiation output per unit length of a radiator of length L in the Tamm-Frank theory is given by:

$$dW/dL = (Ze/c)^2 \int(1 - (\beta n)^{-2})\nu d\nu$$

---

†This is the residual current that flows in a phototube in the complete absence of light [30 Jelley chapter 5].

Energy loss is typically ~0.1% of collision loss and is proportional to $\nu d\nu$ (in contrast to $d\nu$ for bremstrahlung), and consequently Cerenkov radiation is found mainly in the blue/UV regions. From this equation the number of Cerenkov photons emitted per unit length of radiator within the spectral range bounded by λ_1 and λ_2 is given by:

$$dN(\gamma)/dL = 2\pi\alpha Z^2(\lambda_2^{-1} - \lambda_1^{-1})\sin^2(\theta)$$

Threshold counters, which are used in our experiment, detect particles which have a velocity sufficient to produce Cerenkov light in the radiator. The threshold velocity β_0 is that velocity corresponding to a Cerenkov angle $\theta=0$, ie $\beta_0=1/n$. In practice a finite value of θ is required before the efficiency of the photodetector reaches an acceptable value, but is normally attained in a small (or adequate) momentum range. The mean number of photo electrons detected is given by:

$$\langle n\rangle = AL\sin^2(\theta)$$

where A, typically ~90cm^{-1} in our experiment, characterises the photodetector taking into account such things as: the Cerenkov light spectrum, the transmission of the optics and the phototube quantum efficiencies (typically ~15%). In BC72/73 only a small number of photoelectrons were produced (~10 maximum). Due to statistical fluctuations in the emission of photoelectrons Poisson statistics can be used to define a detection efficiency ϵ (or probability of detecting light) as:

$$\epsilon = 1 - \exp(-\langle n\rangle)$$

4.2 DESCRIPTION OF THE CERENKOV SYSTEM

I joined the SLAC Photon Collaboration in November 1982, after the last data-taking run of BC72/73, but before the first run of BC75, and inherited certain responsibities for the Cerenkovs. The precise details of the design, construction and implementation of the detector had already been reported [32], but the main features of the system are summarised below.

Various design constraints were placed on the Cerenkov counter system which had to provide charged particle identification over a wide momentum range with high acceptance. Primarily it had to be compact and the close proximity of the counters to the bubble chamber magnet required the phototubes to be shielded from the fringe field of about 40 Gauss. These considerations and others resulted in the construction of two gas threshold counters using a focusing mirror system (see figure 13). Both counters were operated at about atmospheric pressure which consequently avoided the need for a complex and costly gas circulation system and allowed the use of thin, low mass materials for the entrance and exit windows (particularly important with the Pb-glass wall behind). Inside each counter were two adjustable opaque blinds positioned on either side and parallel to the beam path. These were intended to confine the Cerenkov light produced by the large electron pair background from beam γ conversions.

In each counter there were 12 spherical mirrors stacked close to the exit window. These reflected and focused the light generated in the gas into the entrance aperture of cone-shaped

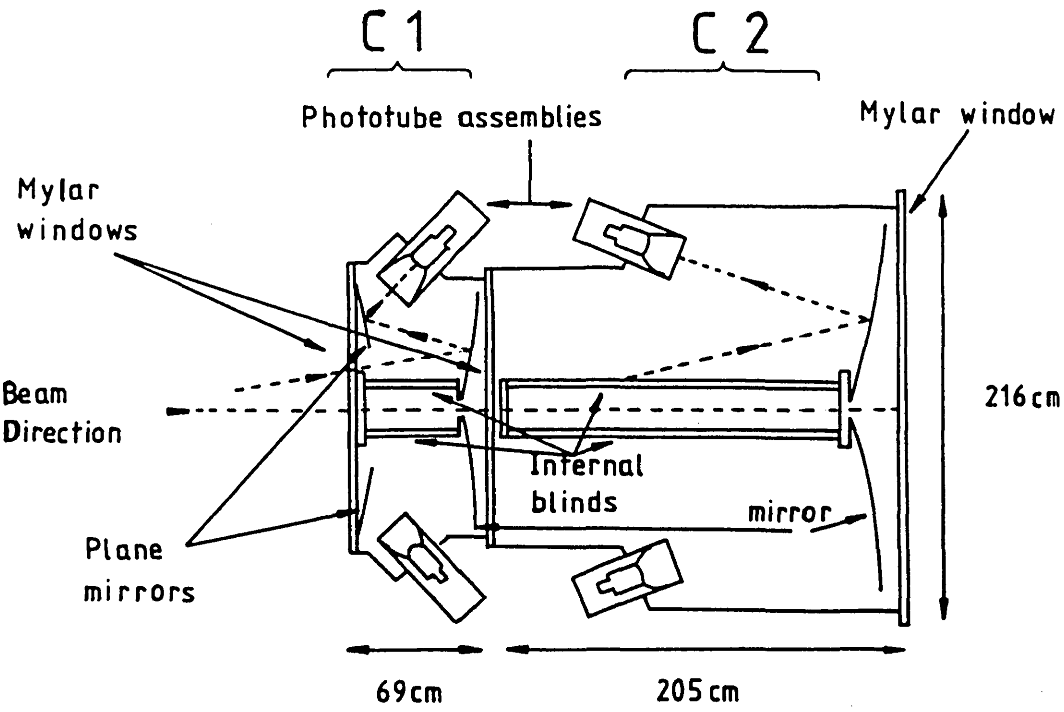

Figure 13: Cerenkov layout

light collecting funnels (of Hinterberger-Winston design [32]). Light generated in the upstream counter C1 underwent a second reflection before entering the H-W cones, which not only minimised the angle of reflection from the primary mirror and thus distortions, but also allowed the counter to be positioned closer to the bubble chamber without obstruction from the phototube housing and so also aided magnetic shielding. The smaller counter C1 had an effective collecting area of $2.2m^2$, while the larger downstream counter C2 had $5.0m^2$. Each mirror was viewed by its own phototube which was aimed horizontally at approximately the centre of the facing mirror and positioned out of the line-of-flight of particles contained within the exit windows. Table 5 summarises the material in the counters. The optical layout of the counters was optimised by a Monte Carlo ray tracing program [33]. Using this program I checked predictions for the BC75 gas prior to the first run in April 1983.

COMPONENT	POSITION x cm
Bubble Chamber Centre	0.0
Cerenkov C1	
Entrance Window	310.0
Plane Mirror Centre	318.0
Spherical Mirror Centre	370.5
(Mirror size 37 x 50 cm^2)	
Cerenkov C2	
Entrance Window	381.5
Spherical Mirror Centre	565.5
(Mirror size 55 x 75 cm^2)	
Exit Window	586.5

GAS	FREON-12 (CCl_2F_2)	NITROGEN (N_2)	FREON-114 ($C_2Cl_2F_4$)
Refractive Index at S.T.P.	1.00108	1.00030	1.00140
Maximum Cerenkov Angle	2.66°	1.40°	3.03°
Radiation Length X_0	48m	300m	35m
Normal Boiling Point	-30°C	-196°C	4°C

COMPONENT	MATERIAL	THICKNESS x	x/X_0 (%)
Entrance window	Melinex	120 μm	0.0
Plane mirror	Glass	2 mm	1.9
Gas (BC72/73)	Freon-12	~55 cm	1.1
Gas (BC75/76)	Freon-114		1.6
Spherical mirror	Glass	3 mm	2.8
Mirror support	Aluminium	3.2 mm	3.6
Gas (BC72/73)	Freon-12	~12 cm	0.2
Gas (BC75/76)	Freon-114		0.3
Window	Melinex	120 um	0.0
Gas (BC72/73)	Nitrogen	~180 cm	0.6
Gas (BC75/76)	Freon-114		5.1
Spherical mirror	Glass	3 mm	2.8
Mirror support	Aluminium	3.2 mm	3.6
Gas (BC72/73)	Nitrogen	~20 cm	0.1
Gas (BC75/76)	Freon-114		0.6
Exit window	Aluminium	0.8 mm	0.9

Plane mirrors occupy 30% of the entrance aperture.
Mirror supports cover 8% of the effective mirror area.

TABLE 5

Cerenkov Counter Vital Statistics

The gases selected for BC72/73 were Freon-12 and Nitrogen for C1 and C2 respectively. However, this left a gap in particle identification in the momentum interval ~1.5-3.0 GeV/c. To maximise the range of particle identification Freon-114 was chosen to fill both counters for BC75, which would lower the pion threshold to 2.6 GeV/c (see table 2).

4.3 HYBRIDISATION

Using information from the Cerenkovs depends entirely on 'hybridisation'. We recall that this process attempted to identify charged tracks projected from the bubble chamber with 'hits' in the PWC stations. All hybrid tracks were further projected out to the mirror planes of each Cerenkov - allowing a prediction of a hit position and consequently a predicted mirror or 'cell'. Given a predicted cell, a test could then be made as to whether or not the track produced light in that cell. A minimum of 3 hits in different PWC stations was required to define a hybrid track so that errors caused by track interactions in the window, PWCs etc, were avoided. However, two further criteria were required for Cerenkov tracks: at least one y hit, and at least one hit in the PWC γ station. In general 92% of hybrid tracks had a γ hit rising to 97% for those above 3.0 GeV/c. (Each event with hybrid tracks had a 'Hybrid Block' added to the DST data record.)

The close relationship between hybridisation and the PWCs would seem to suggest an event with a hybrid block implies a PWC trigger. However, this was not entirely true since 18% of BC72/73 hadronic hybrid events were not PWC triggers. For example, a fast charged track could produce a lead glass trigger. Also, the PWC dead region used for off-line hybridisation was narrower, in general, than that used by the on-line trigger. This difference in dead region was possible since off-line genuine tracks from hadronic interactions were being projected through the PWCs whereas on-line background triggers from e^+e^- pairs also occurred frequently.

Shortly after the spring run of BC75 a problem with SLAC hybridisation [34] became evident in that the distributions of predicted hits at the mirror planes were asymmetric and further shown to be correlated in time with the introduction of the new thicker bubble chamber window during BC72/73. Normally a symmetric distribution centered on the shadow of the PWC dead region was observed, but with this sample there was a distinct lack of hits on the right hand side of the counters (as viewed by the beam). A possible explanation, hardware 'saturation' in the PWCs (too many hits for the digitisers), was discounted after the PWC hit distributions were examined. Further investigation ultimately revealed a software problem and consequently most of the data since spring 1980 (roll 2550) had to be re-hybridised.

4.4 MONITORING THE CERENKOVS

On-line monitoring was limited to an option provided by the Background program which counted the light in cells over some time interval. The light count was expected to peak symmetrically in the central cells of each counter, and therefore any asymmetry could be acted upon promptly. Normally sufficient counts would have built up over an hour for light to occur in each cell. This kind of monitoring was very limited in that it was only really sensitive to obvious problems, eg, failed power supply or bad alignment. At the beginning of each run the counters, which were movable transverse to the beamline on stainless steel runners, were positioned centrally using a plumb line and a marker line drawn on the floor of the experiment building. Figure 14 shows the probability of light per cell per hybrid event.

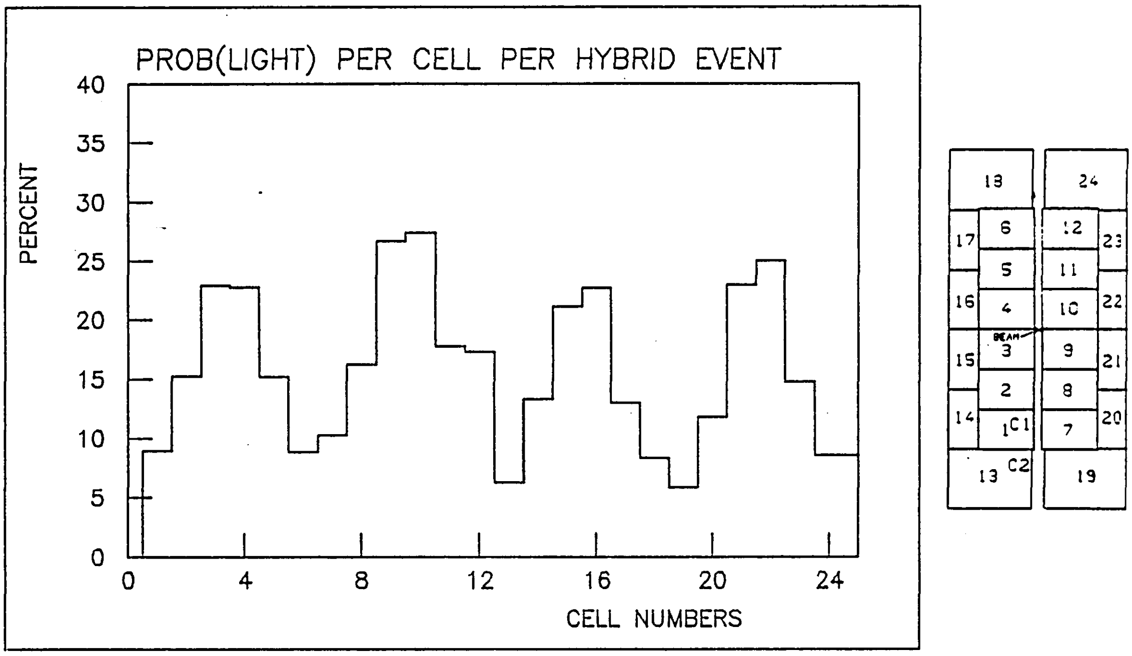

Figure 14: Cell Light Distribution (BC72/73)

Immediately off-line it was possible, for instance, to examine the raw pulse heights in each cell stored on the NOVA tapes. Importance was given to locating the one photoelectron peak for each cell (~ADC channel 50), primarily to ensure that the phototube was functioning correctly, but also to determine a cut to be placed between it and the pedestal so that a cell could be flagged as containing light or not (typically pedestal+25 where the pedestal is an ADC channel representing no signal).

Detailed examination of the Cerenkovs always had to wait for sufficient events to be processed (usually post-run). The performance of the counters is discussed in the following sections with emphasis on BC72/73.

4.5 CERENKOV PERFORMANCE (BC72/73)

The results of hybridisation and kinematic fitting allowed detailed investigation of the Cerenkov counters by providing ~23400 hybrid 3 prong events with 3C fits. Requiring the χ^2 probability >2% leaves ~19700 with ~95% fits to $\gamma p \rightarrow p\pi^+\pi^-$ and ~4.2% to $\gamma p \rightarrow pK^+K^-$, which makes available a source of 'identified' pions and kaons.

4.5.1 Pulse Heights and Threshold Behaviour

Pulse height identification of tracks was not possible in our counters because of a maximum of only 8-10 photoelectrons at the highest energy. Figure 15 shows a typical pulse height spectrum (with pedestal subtracted) for all hybrid tracks above the pion threshold in C1. A peak corresponding to single photoelectrons is clearly visible with possibly other peaks. Some fluctuations in the gain of phototubes occurred, of course, but the pulse height spectrum shown is a result of the particles having a range of energies and hence smearing the peaks. A general trend can be seen if we plot the pulse heights for hybrid tracks as a function

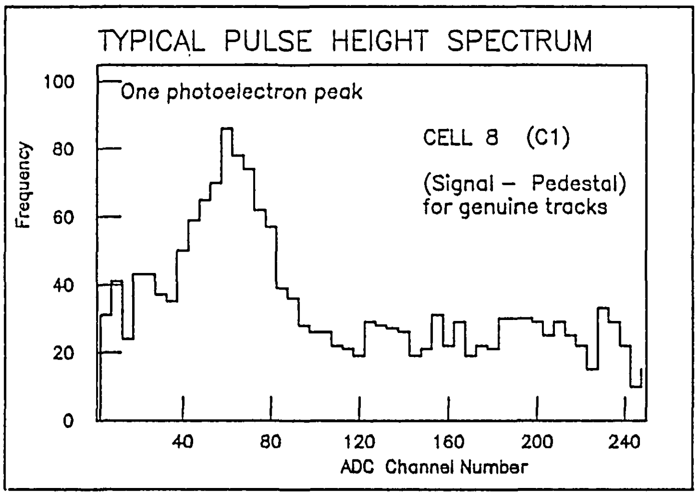

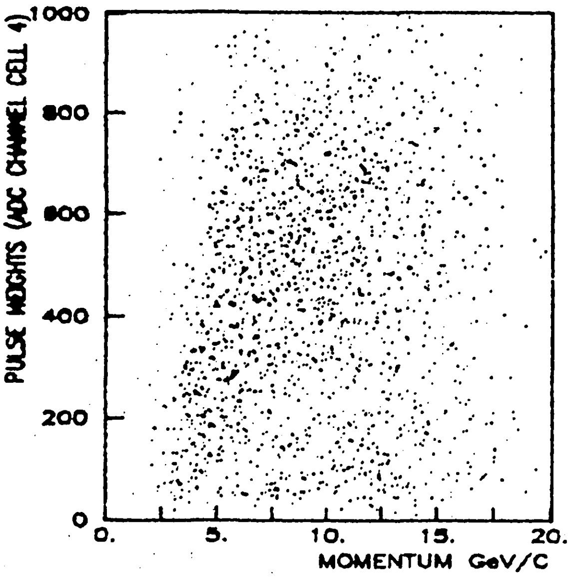

Figure 15: Typical pulse height spectrum

Figure 16: Pulse Height v. Momentum

of momentum (figure 16). There is clearly a wide spread (a consequence of Poisson statistics) and furthermore no 'band' structure is visible above the kaon threshold, illustrating that pulse heights can only be used in a threshold manner.

The threshold region is very important in that it indicates/confirms the presence of the gas and consequently allows subsequent particle identification with confidence.

Recall that the probability of producing photoelectrons (detecting light) was given by $P(n\neq 0) = 1 - \exp(-\langle n\rangle)$ and so comparing this with the probability of producing light (figure 17) calculated using fitted pions shows striking differences in the threshold behavior of each counter.

There is good agreement between expectations based on Poisson statistics and data in C2 which is everywhere within 10% (lower) of the predicted value, peaking at about 90-95%. In contrast, the threshold rise is much more gradual in C1 and is everywhere much lower, reaching only ~85%. The principal explanation of these curves arises from consideration of the mirrors in each counter. The Cerenkov angle is larger (due to Freon-12) and the mirror sizes smaller in C1 than they are in C2 (containing Nitrogen). Consequently there is a larger probability that in C1 a light cone (diameter ~5cm maximum for pions in C1 and ~8.5cm in C2) will spread beyond the edge of a mirror than there is in C2, where it is more likely to be confined to one mirror. This suggests that boundary cuts, defining sensitive regions of the mirrors, may improve efficiency but at a cost to the data sample to be discussed below.

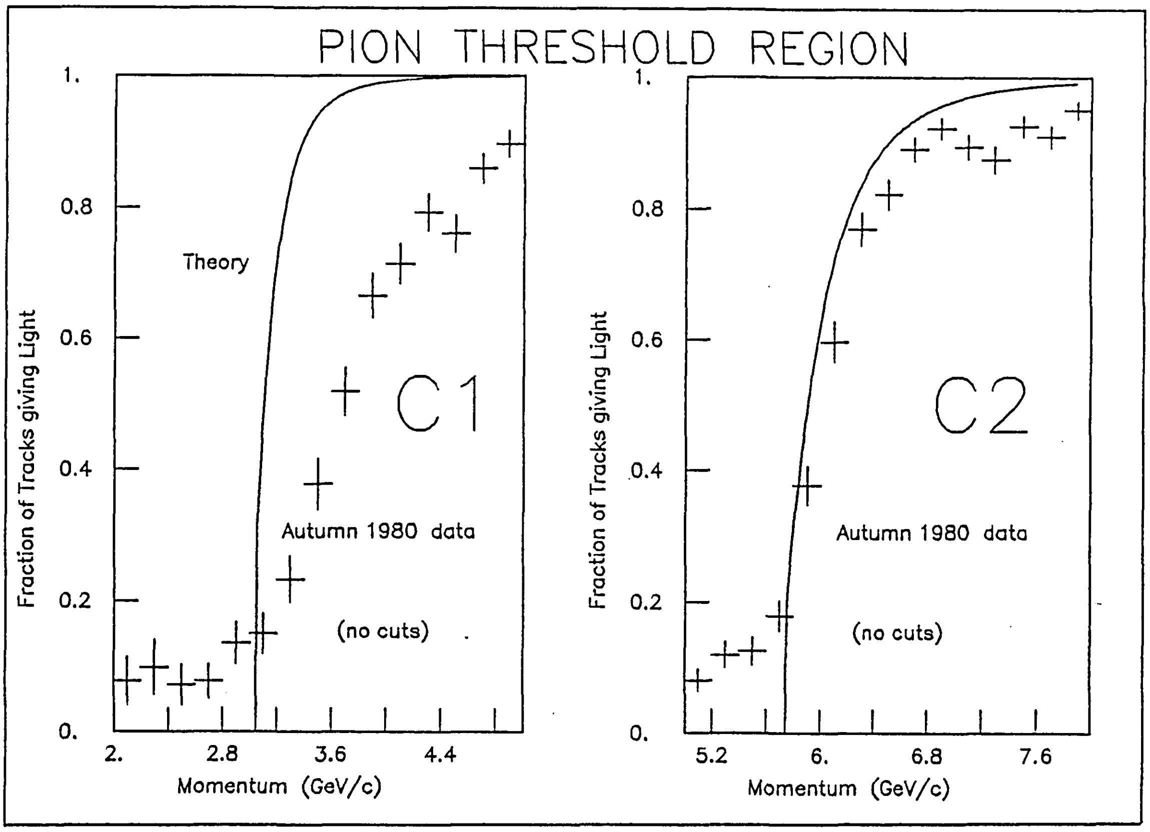

Figure 17: Threshold Behavior

4.5.2 Acceptance

Acceptance curves for the Cerenkovs were calculated using actual data and are shown in figure 18. At higher momenta a larger fraction of tracks enter the dead region and so lower the acceptance. Figure 19 shows that above 2 GeV/c >80% of tracks hybridised. The main loss of acceptance was due to tracks passing through the blinds. The dip at low Pt (<200 MeV/c) for all tracks was a consequence of a loss in trigger efficiency on events with only low Pt forward tracks.

Using the same data sample it was determined that the probability of two tracks entering the same cell was less than 0.9%. Averaging over all events 87% of tracks hit C1 (4% C1 only) and 83% hit both counters, but note that this is multiplicity dependent.

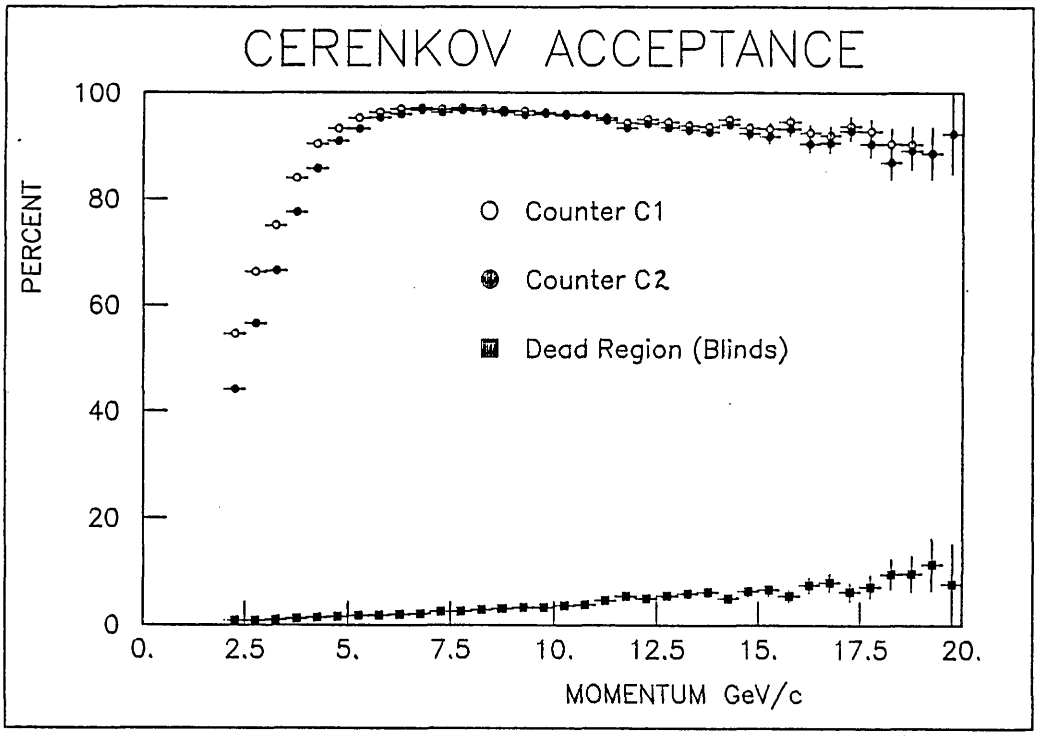

Figure 18: Acceptance curves for C1 and C2

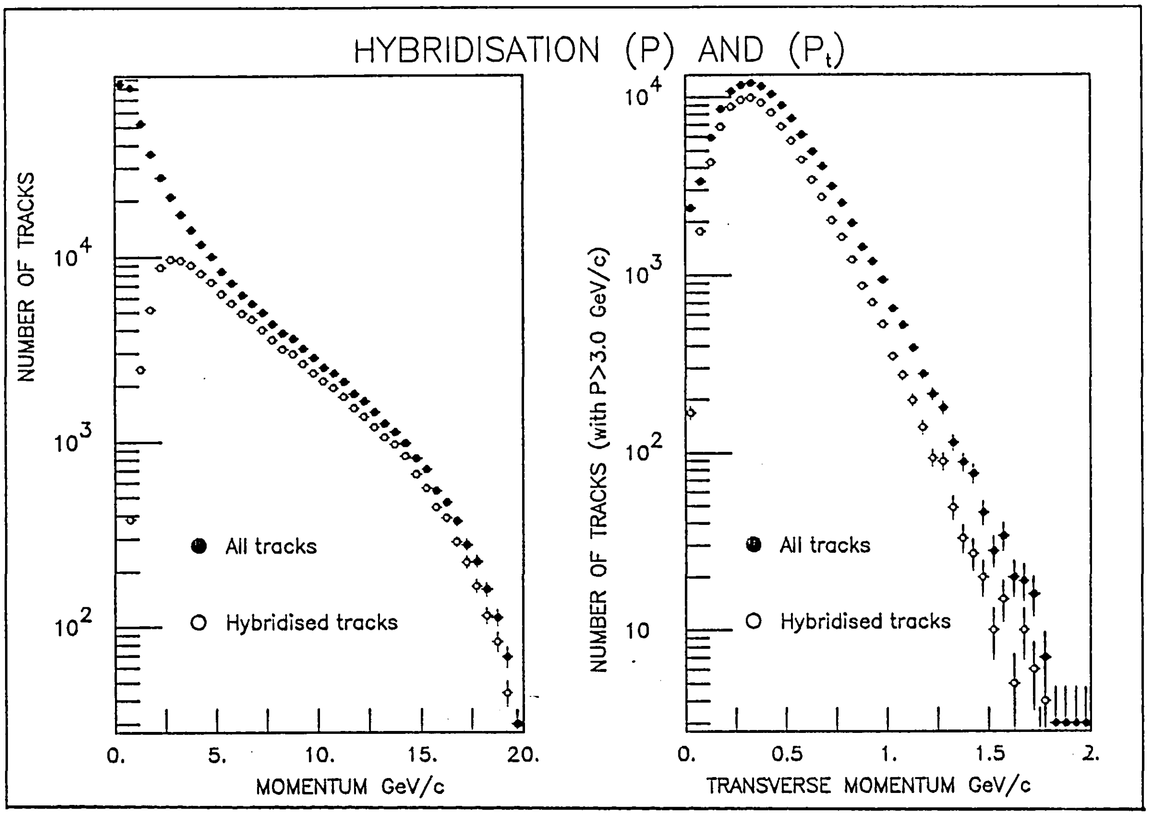

Figure 19: Hybridisation rates

4.5.3 Pion Efficiency

The vast majority of final state hadrons passing through the counters will be pions and therefore by plotting as a function of momentum the fraction of hybridised tracks which reach the Cerenkovs and give light a "pseudo-efficiency" curve for each counter is obtained (see figure 20 for BC72/73 gases). A clear rise at the pion threshold in the number of tracks producing light, to ~80% above 4 GeV/c in C1 and to ~80% above 7 GeV/c in C2, confirms that the majority of tracks were pions and that the counters functioned correctly. However, some tracks below threshold apparently gave light. The main reason for this was π^0 decays producing photons, which with a ~30% probability of

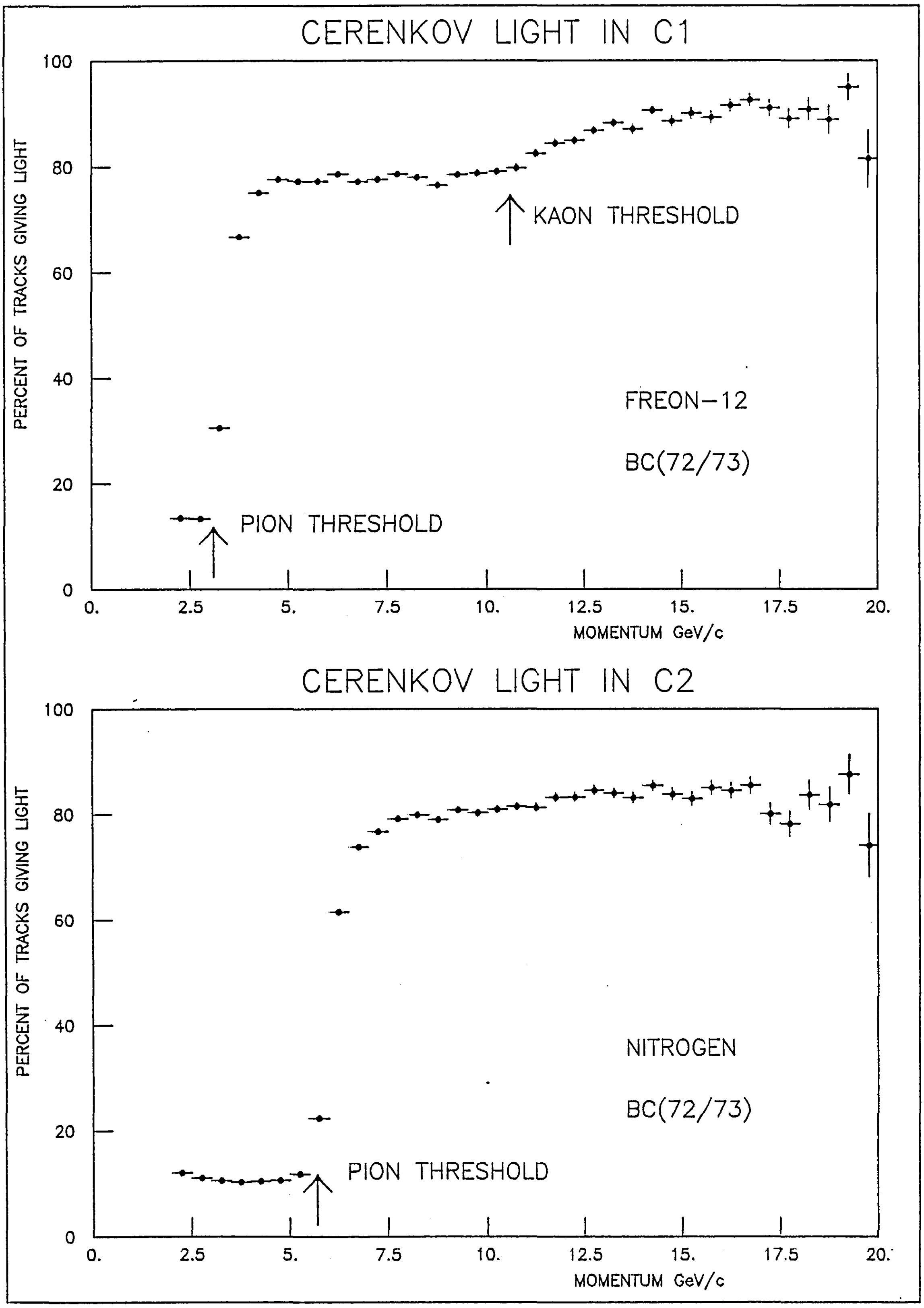

CERENKOV LIGHT IN C1

CERENKOV LIGHT IN C2

Figure 20: Light Rates in C1 and C2 (BC72/73)

converting between the production vertex and the Cerenkovs would produce e^+e^- pairs above threshold. The distribution of light in the cells in events without hybrid tracks suggests the probability of background light from beam conversions is ~0.2% per cell per hybrid event. A further rise in C1 of the number of tracks giving light above 10.6 GeV/c (to ~90% above 12 GeV/c) corresponds to the kaon threshold and clearly indicates the presence of kaons. Dividing this C1 curve by acceptance suggests that at high momenta the charged π:K ratio is 8:1 [35].

The probability of detecting light from pions as a function of momentum is shown in figure 21 for each counter. Calculated using the fitted pions this represents the pion efficiency for producing detectable light. Examination of the plots shows that C1 reaches ~90% efficiency above ~4 GeV/c and C2, slightly more efficient, reaches ~93% above ~7 GeV/c, in both cases ~1GeV/c above threshold. Both counters have a background rate of ~9% below threshold. Combining the data from C1 and C2 by counting whether the pions gave light correctly figure 22 shows the combined pion efficiency for the Cerenkov system as a whole. This is everywhere >90% except in the threshold regions of 3.0 and 5.7 GeV/c as expected and indicated earlier. These efficiencies can be improved upon at some cost to the data sample as can be seen in the following section.

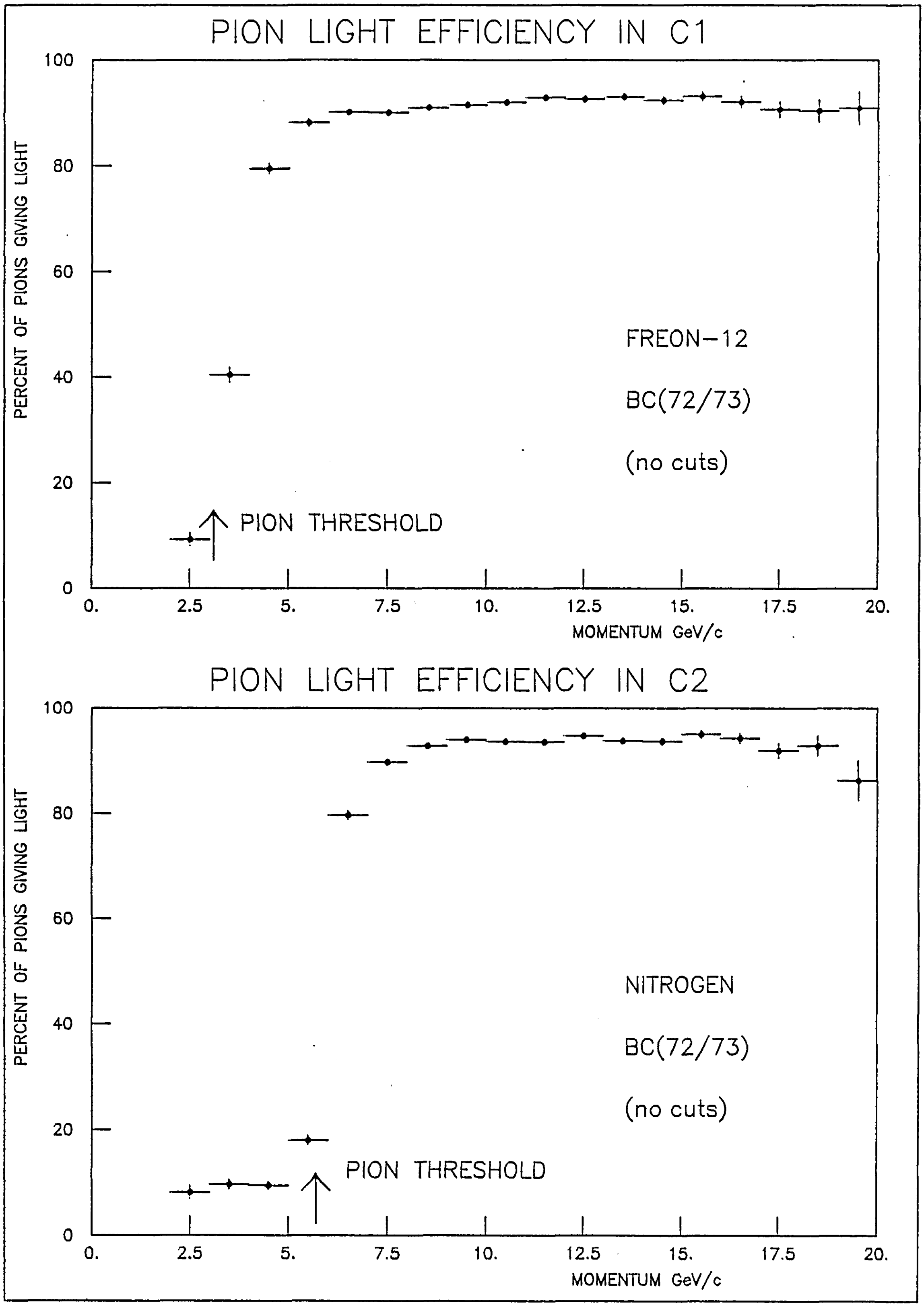
PION LIGHT EFFICIENCY IN C1

PION LIGHT EFFICIENCY IN C2

Figure 21: Pion Efficiencies in C1 & C2 (BC72/73)

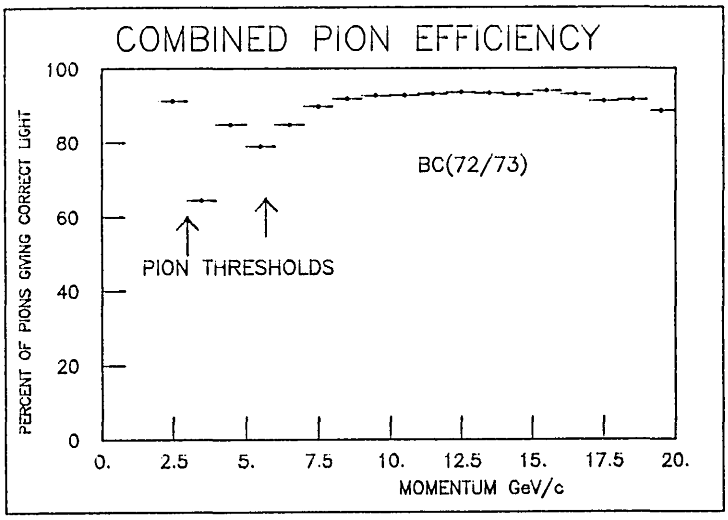

Figure 22: Combined Pion Efficiency in Cerenkov System

4.5.4 Counter Characteristics and Mirror Effects

The lower than expected efficiency, as shown by the threshold plots, results from the light collection not being equally efficient over the entire mirror area as will be demonstrated. Consequently a potential for track misidentification exists, with a higher probability in C1 than in C2, as demonstrated by an investigation of 'edge effects' near mirror boundaries. This was achieved by examining the probability of light as a function of the distance in y and z from the mirror boundary.

The z distribution at the mirror planes for hybrid tracks above 3 GeV/c is shown in figure 23. The distribution peaks towards the blinds, falling away sharply on either side towards the outer edges of the counters. The 'hole' in the distribution was a consequence of the PWC dead region. Only 1% of the tracks are within 7cm of the outer edges of C1 and also only 1% are within 18cm of the outer edges of C2, from which it is reasonable to assume that these tracks make a negligible contribution to the overall inefficiency, in sharp contrast to those tracks hitting near to the blinds.

The effects of the blinds are evident in figure 25 where the contents of the predicted cell (light/no light) has been plotted as a function of the projected horizontal position (z) at the mirror planes of each counter. The plots show a rapid fall in the probability of producing light for tracks close to the blinds, suggesting the following cuts: dz~2.5cm in C1 and dz~3.5cm in C2. However, these cuts throw away ~18% of the data in each counter corresponding to an improvement of only ~3% in pion efficiency. Tracks passing between the blinds apparently produced light some of the time [32] in the nearest cell, indicating the blinds not to be completely efficient at confining light. This effect was still present when only tracks below threshold were used and so has been attributed to accidental occurrences of electrons from γ conversions.

Another potential source of misidentification is for tracks to pass close to cell boundaries between mirrors, where light may be split between two cells or even be directed mainly into the nearest adjacent cell. The investigation of these boundary effects (in the y direction) required a slightly more complex

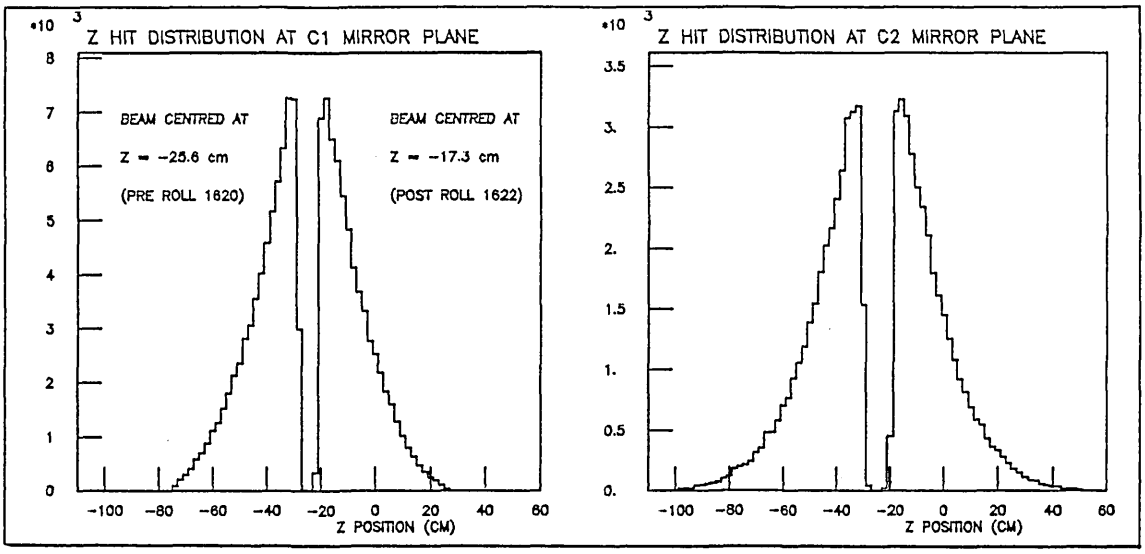

Figure 23: Z hit distribution at Mirror Plane

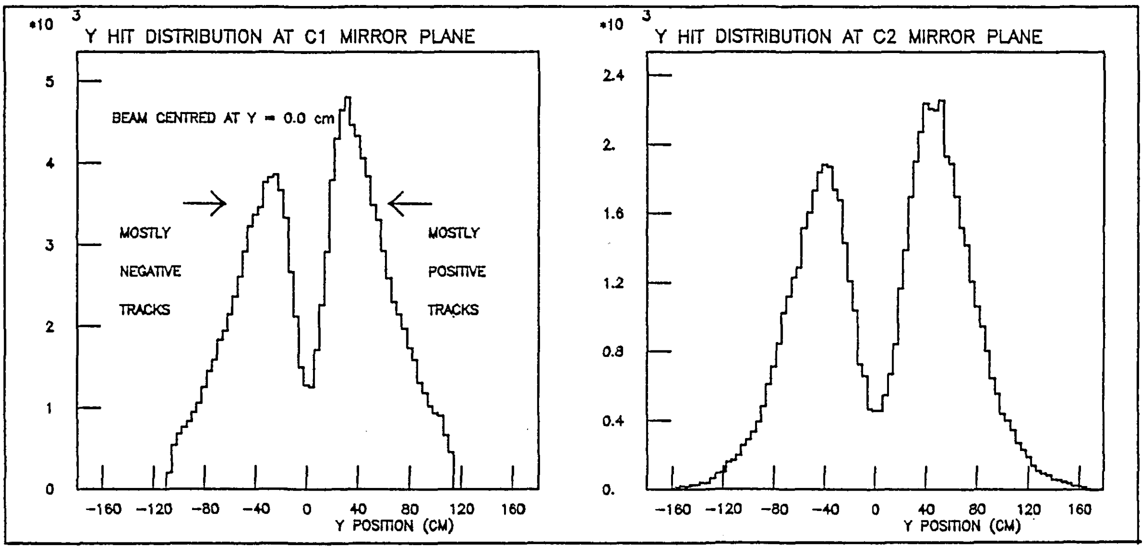

Figure 24: Y hit distribution at Mirror Plane

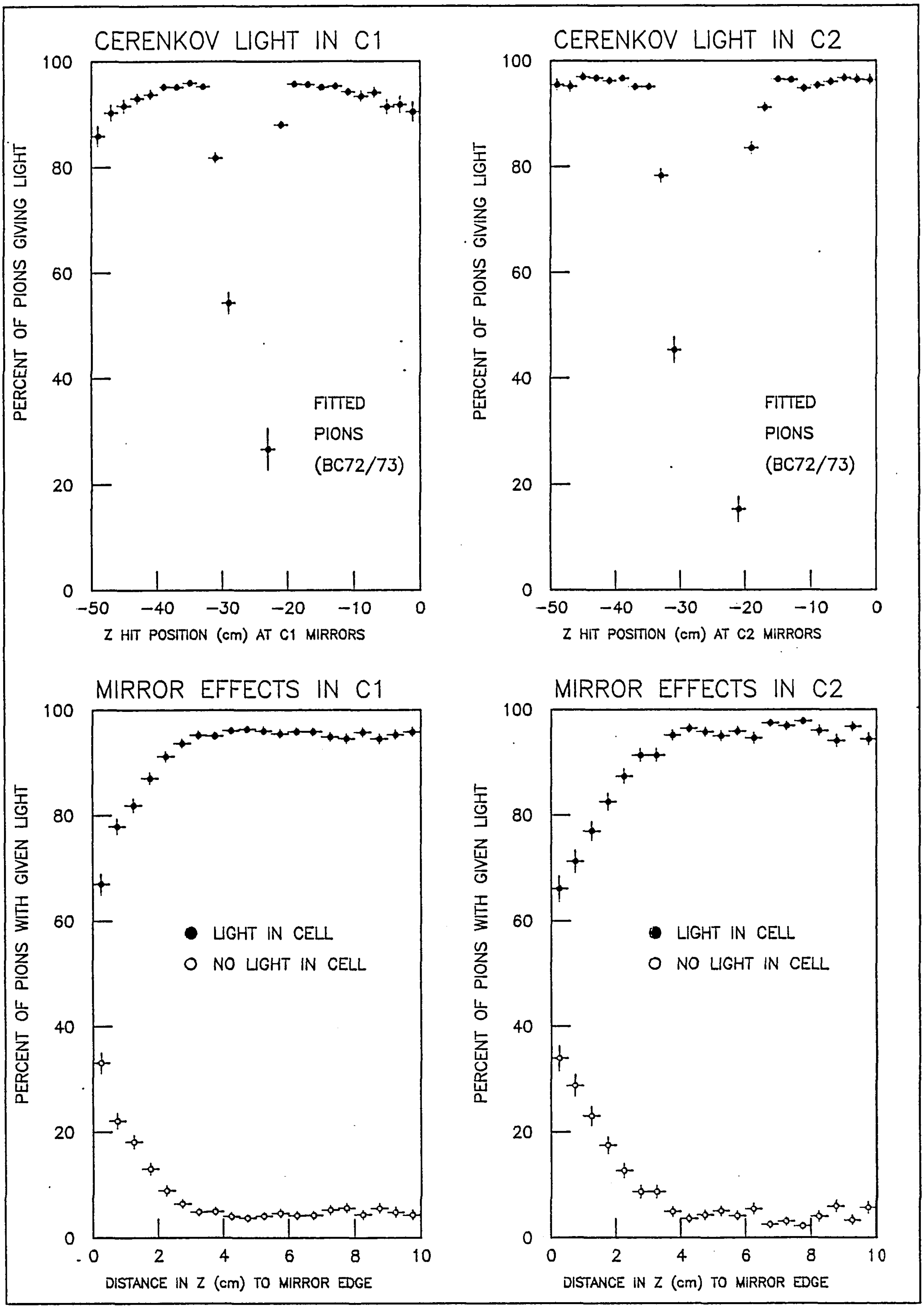

Figure 25: Light as a function of z Position

approach. For instance, figure 24 shows the distribution of projected vertical positions (y) at the mirror planes, and despite similarities with the z distributions the differences are such that no cell boundary should be ignored. A 'feel' for the frequency of light throughout the counters is hinted at by figure 26 which shows the relative multiplicity of cells with light.

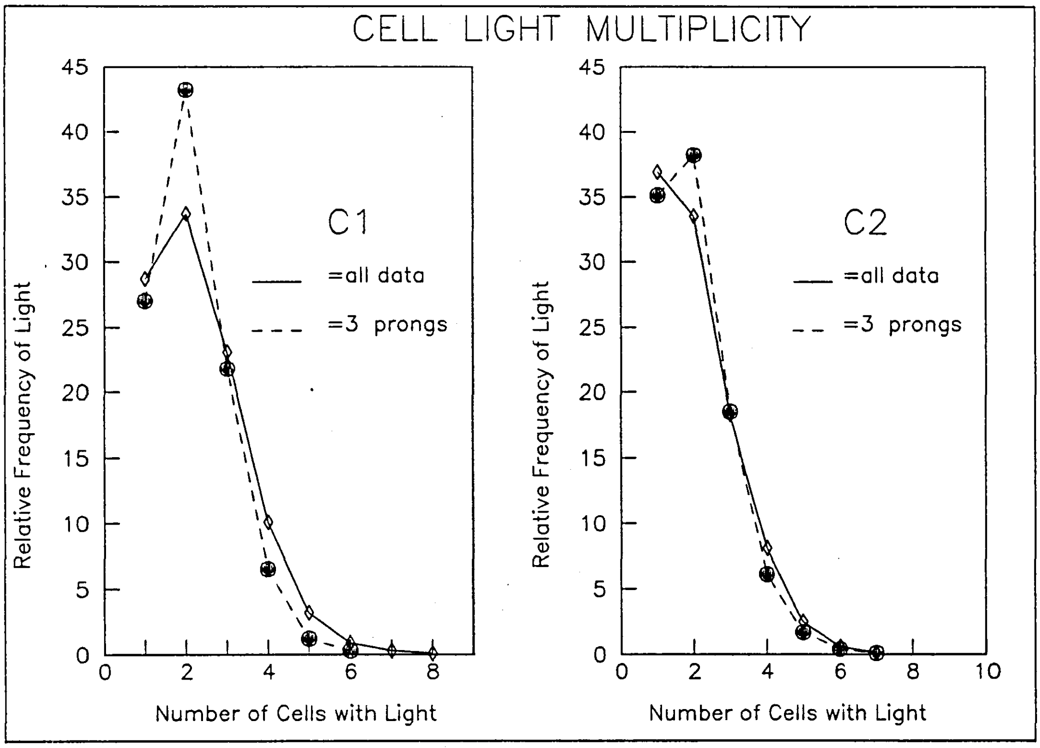

Figure 26: Multiplicity of cells with Light

This effect was studied by grouping all the cells together (as with the z plots) and looking at the four possible light/no light combinations in the predicted cell ($p=1$ or $\bar{0}$) and the nearest adjacent cell (n=1 or 0). Using fitted pions these combinations are plotted as a function of distance in y (dy) between the predicted hit position and the nearest cell boundary (figure 27). Both counters have similar characteristics:

a) (p=1,n=0) the probability of a track giving light in the predicted cell only is ~85% until within ~5cm of the boundary and falls to ~40% at the boundary. This is consistent with the light cone now overlapping two cells.

b) (p=1,n=1) the interpretation above is further supported by the behavior of the probability of light in both the predicted cell and the nearest adjacent cell. It remains ~7% until within ~5cm of the boundary where it rises to ~30%.

Neither (a) nor (b) lead to misidentification.

c) (p=0,n=1) the probability of finding no light in the predicted cell but light in the adjacent cell is however a source of misidentification. It is less than 1% throughout the cell, which can be accredited to accidental occurrences, but rises to ~25% near the cell boundary. This rise is understood as a consequence of an uncertainty in the predicted hit position at the mirror planes, for example, as a result of scattering leading to an incorrect prediction of the true hit cell.

d) (p=0,n=0) the probability of finding no light in either cell was approximately uniform at ~5% throughout the cells.

The plots suggest reasonable cuts of dy < 3.0cm in C1 and dy <3.5cm in C2 (which encompasses ~15% of the data) consistent with early results on a very small sample [36]. Ignoring tracks within the cuts meant that pions above threshold were ~97% efficient (after cuts) at producing light.

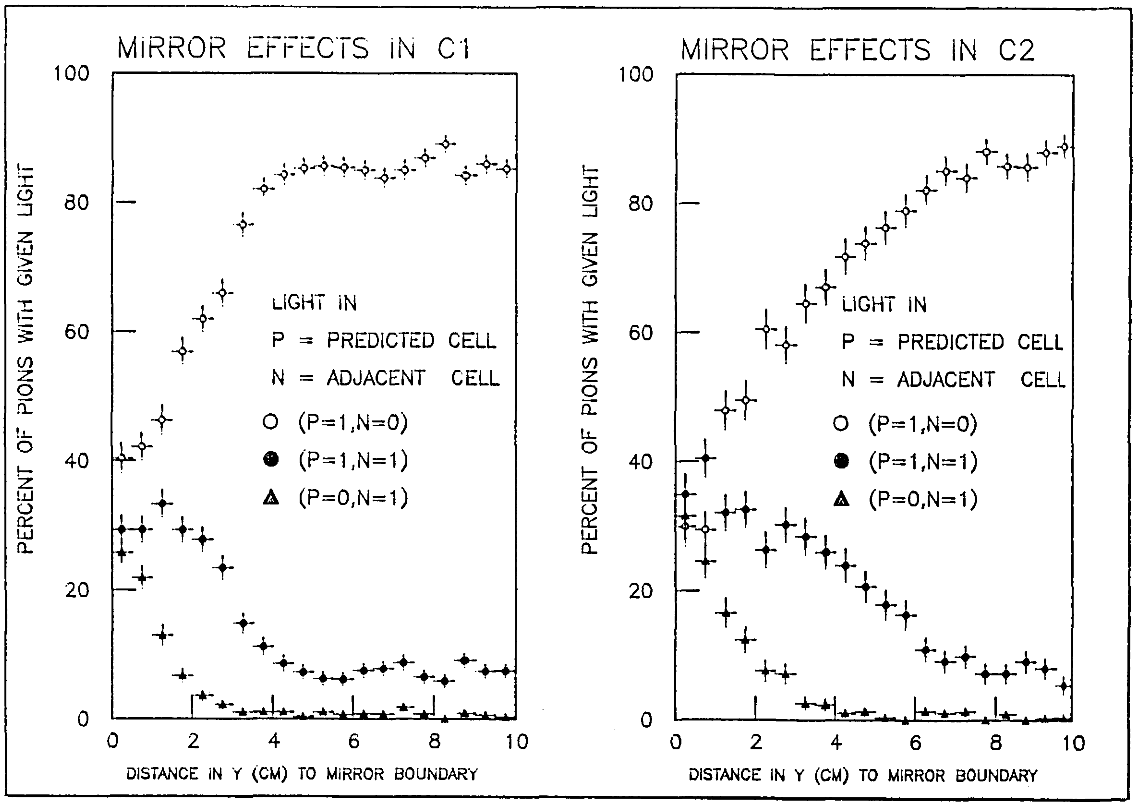

Figure 27: Light distributions in y near Mirror Boundaries

4.5.5 Kaon Efficiency

About 3100 events had 3C fits to $\gamma p \rightarrow pK^+K^-$ of which 859 were the best fit with χ^2 probability >2%. However, light in C1 suggested that some of these events were $\gamma p \rightarrow p\pi^+\pi^-$ where measurement errors had allowed the kaon fit. Therefore, to minimise pion contamination 'unique' fits were selected (those events with only one fit above the cut) giving 589 events and ~800 'identified' hybrid kaons. Using these fits the probability of detecting light from kaons, ie, the kaon efficiency for producing detectable light, is shown in figure 28 (for C1 only since kaons should never give light in C2). Despite this, background light occured in C2 at ~20%. Below threshold in C1 there was light at ~16% which rises to ~70% above kaon threshold. However, pion contamination is a problem. Combining the data from each counter (as with the pions) figure 29 shows that ~80% of kaons should be correctly flagged by the Cerenkov counters.

A mirror boundary analysis for kaons would not be practical since statistics are limited and is probably unnecessary because there is no reason to expect the analysis of kaons and pions to be different. The following section discusses particle identification in general and the problems with backgrounds.

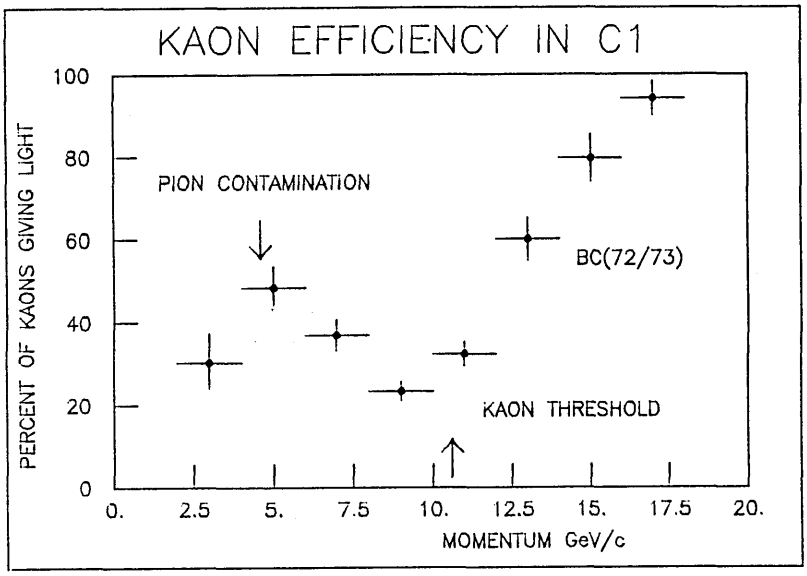

Figure 28: Kaons giving light in C1
Pion contamination degrades the accuracy of this efficiency, and kaons from ϕ decay are too thinly distributed to be useful.

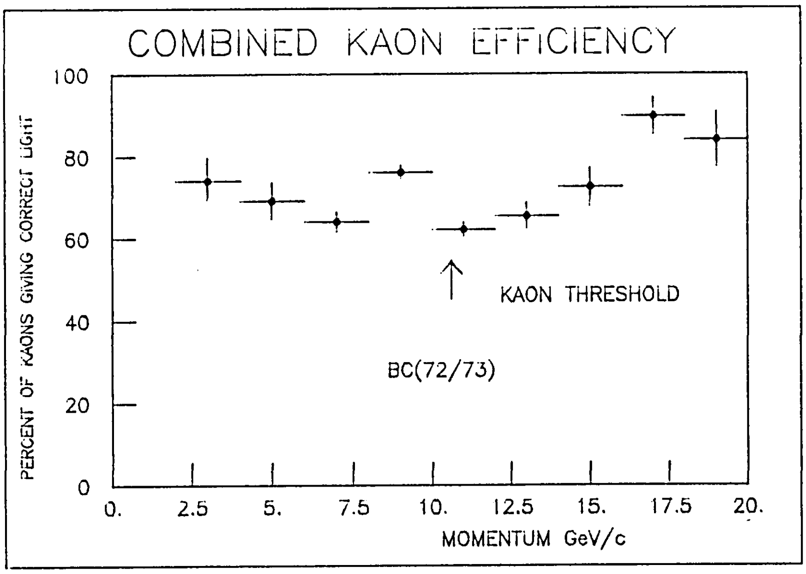

Figure 29: Combined kaon efficiency in Cerenkovs

4.5.6 Background and Particle Identification

The previous sections have shown how efficient pions and kaons were at producing correct light in the Cerenkovs. However, in those cases 'pure' samples of the respective particles were used, whereas in the general data particle identification/separation was required (especially for the charm candidate events), but due to background/inefficiency misidentification will occur.

The background can be examined by looking at the momentum interval 2.0-3.0 GeV/c where pions, kaons and protons are all below threshold. Only electrons are above threshold (the muon background is ignored as insignificant). Each counter has background light at ~12%. Of the tracks which hit both counters only ~80% correctly gave no light in both. This suggests a background problem for ~20% of tracks (~7% had light in C1 only, ~8% had light in C2 only and ~5% had light in both), but its effects are not as serious as first appears. Most pions are above threshold and produce light thus background light would tend to occur at the same time or counteract inefficiencies, especially near threshold. On the other hand, kaons should give no light and so background light will limit kaon identification to potentially ~80%. Background light from energetic knock-on electrons (ie, δ-rays) is estimated to be < 1%.

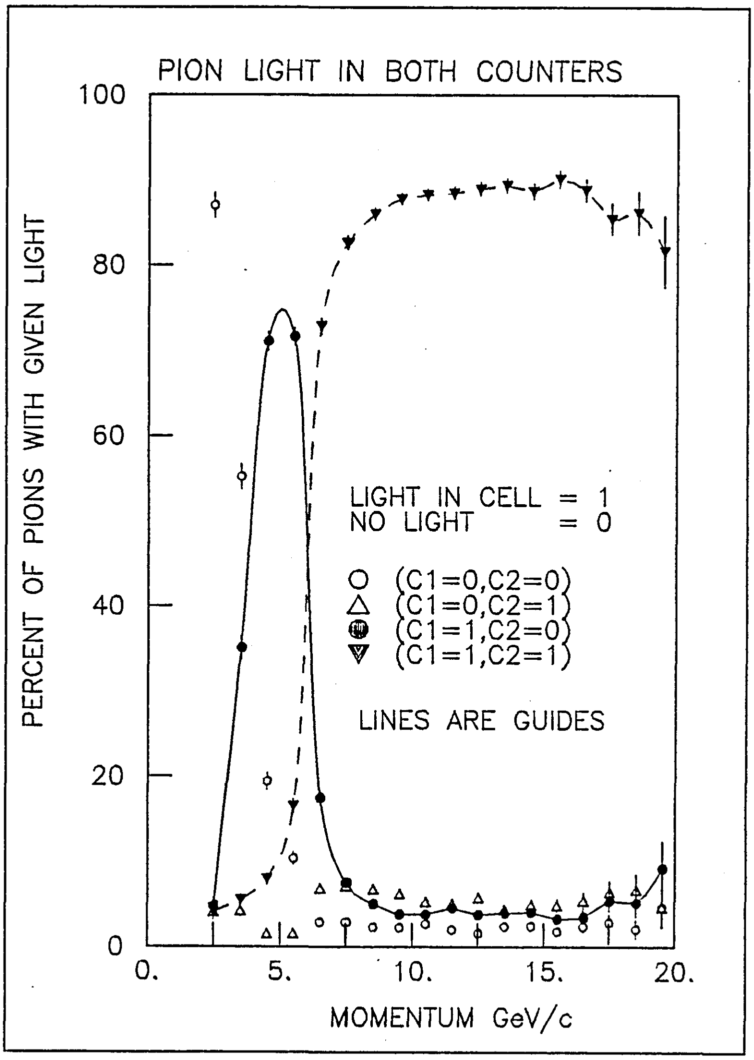

Figure 30: Light Logic for fitted pions

Initially we can make some estimates of misidentification by making the reasonable assumption that the π:K ratio of 8:1 is a good approximation over the entire range. Then, ignoring protons, we can write:

$$N(\pi) = \alpha(\pi)N(\text{true pions}) + \beta(K)N(\text{true kaons})$$

$$N(K) = \alpha(K)N(\text{true kaons}) + \beta(\pi)N(\text{true pions})$$

where α and β are efficiencies and inefficiencies and $N(\pi)$,$N(K)$ the number flagged by the Cerenkovs. In the worst case, where every pion with incorrect light is flagged as a kaon and vice-versa, this suggests only a ~3% kaon contamination of the pion sample, but ~50% pion contamination of the kaon sample! However, examination of the 'light logic' for pions over the entire momentum range (see figure 30) shows that following strict light requirements the above estimates are far too pessimistic. Averaging over the entire range pion inefficiencies lead to an estimate of the contamination of the kaon sample of ~15% without cuts and ~7% with cuts. Similar plots for kaons are consistent with background rates and even without cuts suggests only ~1% kaon contamination of the pion sample, with the main problems arising predictably near thresholds. However, while improving efficiency the mirror boundary cuts drastically lower acceptance.

With these considerations there are two possible strategies for attacking particle identification:

Method CKID [37] considers only sensible light combinations and flags ~85% of tracks as consistent/not consistent with π/K/p above 3.5 GeV/c. There is an unsatisfactory loss of pions flagged/identified in this manner around the pion threshold in C2. However, this can be filled by ignoring the information in C2 over the hole (5.7-8.0 GeV/c) and consequently reducing the number of tracks left 'inconsistent' to ~8%. A similar tolerance in C1 (10.6-15.0 GeV/c) is given to the kaon threshold.

Method CKIDWB [38] attempts further to flag inconsistent tracks. Consider that a 10 GeV/c kaon should give no light in either counter whereas a pion should in both. However a 10 GeV/c track may give no light in C1, but light in C2 and so not fit any hypothesis. Nevertheless, the likelihood that the track is a kaon with background is similar to that of a pion inefficient in C1. By such considerations a track may receive an "identified" flag or "consistent with background/inefficiency" flags, and consequently flag all tracks which hit the counters.

Both methods approach one another and are similarly successful except that the latter tends to flag more tracks as "kaon consistent". Though the contamination of the pion sample is small the contamination of the kaon sample is not. This thesis is concerned with <u>kaons</u> and so, coupled with the two-tier identification of the latter which is therefore difficult to implement, chooses the first method for kaon identification (which rejects inconsistent tracks).

Based upon the fitted events, the results of this algorithm are shown in figure 31 This shows the fraction of charged pions correctly identified and those misidentified as kaons, and also those correctly identified kaons.

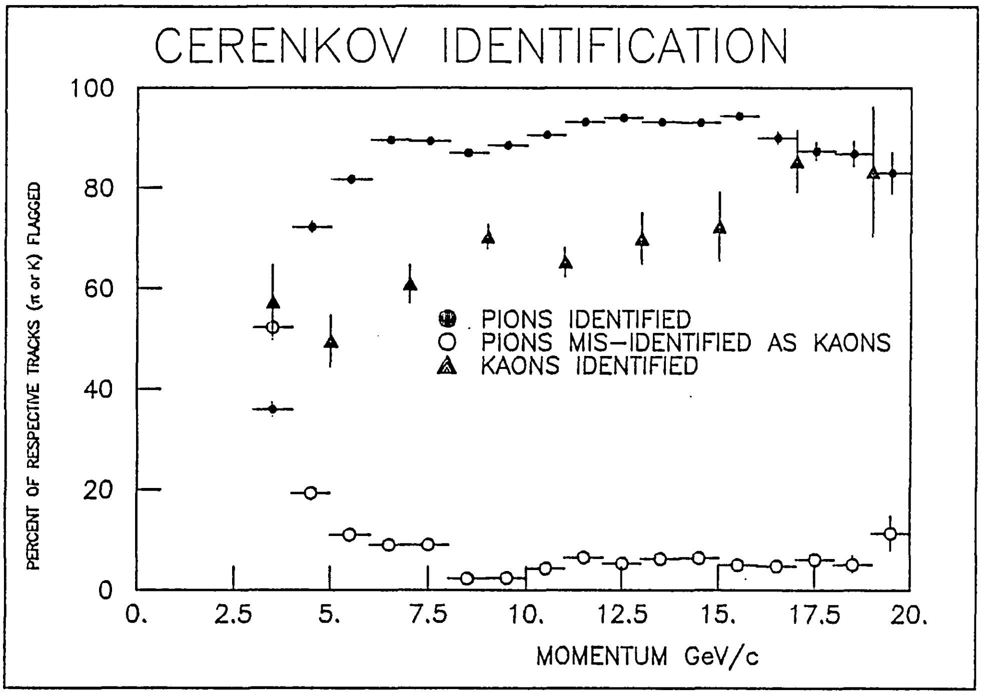

Figure 31: Identification (BC72/73)

4.6 CERENKOV PERFORMANCE (BC75)

In order to lower the momentum threshold of secondary particle identification during BC75 Freon-114 gas was chosen to fill both Cerenkov counters. This was successful for the larger vessel C2 lowering the pion threshold from ~3.0 GeV/c during BC72/73 to ~2.6 GeV/c for BC75, but the behaviour of the smaller vessel C1 was inconsistent with the new gas [39].

The detection efficiency of C2 is shown in figure 32. As before this is the fraction of hybrid tracks recording a hit in the PWC γ station which gave light in the predicted cell. The threshold behaviour of C2 is entirely as expected, ie, an initial rise between 2.0 - 3.0 GeV/c to ~80% (the pion threshold) with a further rise between 9.0 - 10.0 GeV/c to ~95% indicating the kaon threshold. In total ~6600 hybrid (candidate) events were available for BC75 analysis passing vertex cuts.

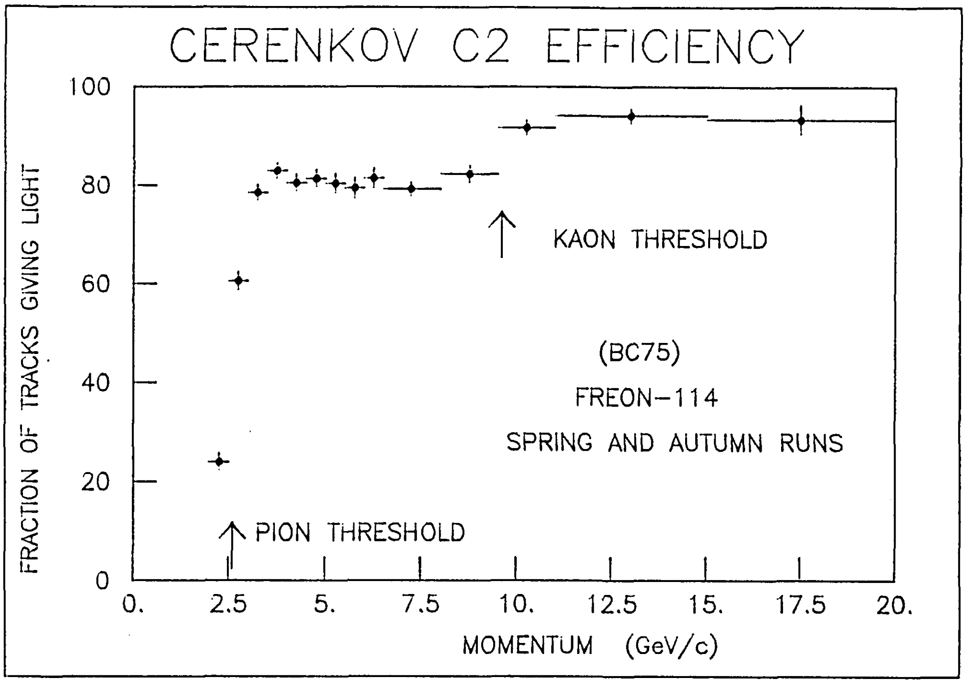

Figure 32: Cerenkov Light C2 (BC75)

4.6.1 The C1 Gas Puzzle

The problem of the threshold behaviour of C1 has been investigated but no satisfactory explanation with hard evidence has been found. It should be noted that the unavoidable delay between data-taking and the measuring of sufficient events had meant that we were unaware of the problem until after the spring 1983 run.

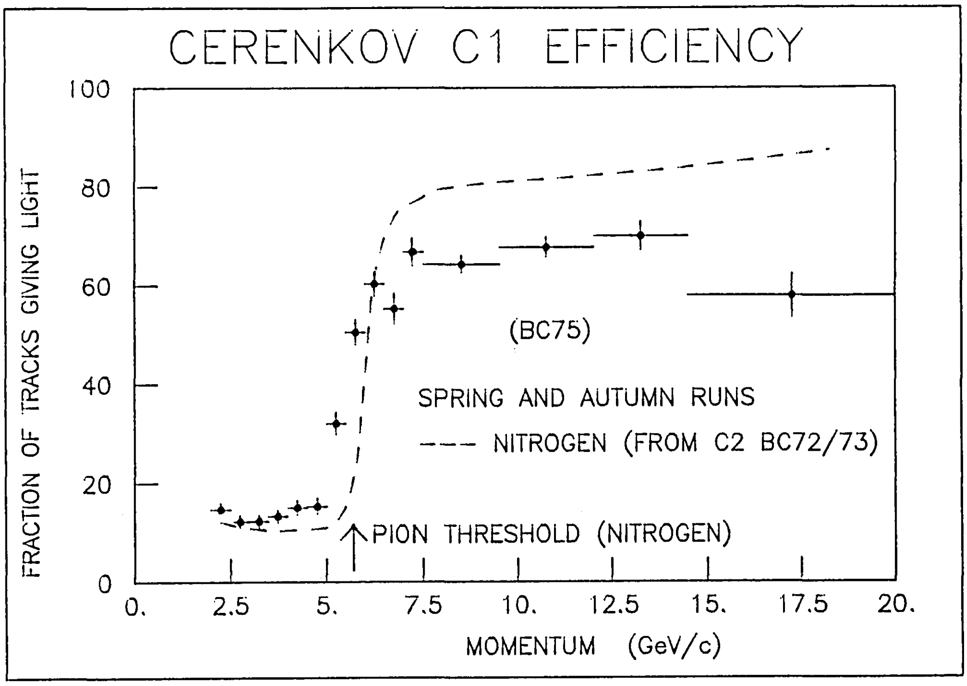

Figure 33: Cerenkov Light C1 (BC75)

In C1 the threshold rise occurs in the range 5.5 - 6.5 GeV/c, well above the pion threshold in Freon-114 (coincidentally the pion threshold in air(nitrogen) is 5.7 GeV/c). This suggests that C1 contained a freon/air mixture and indeed the behaviour for nitrogen (superimposed) has reasonable agreement. Furthermore, figure 34 shows the distribution of cells with light for hadronic events in the fiducial volume. The lower probability of light per cell per event in C1 was believed to be a result of the shorter radiator length of C1 in comparison to C2 and the overlap into several cells of the light cone in C2. However, with the odd C1 light curve this cannot account for the anomalous threshold behaviour.

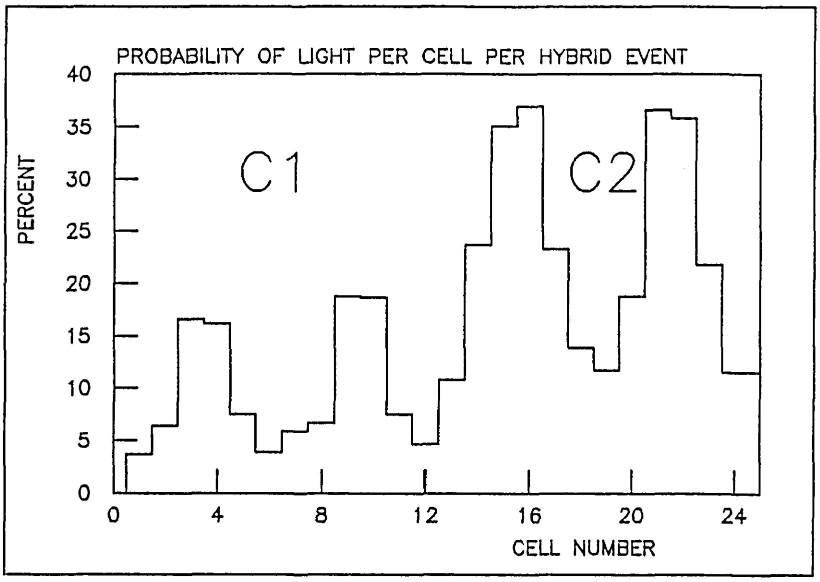

Figure 34: Probability light per cell (BC75)

Various routine checks were made on the data after processing (on-line monitoring had given no hints of a problem). Although cell prediction differences of ~2% were found this was too small to account for C1, even though C1 was naturally more sensitive to incorrect cell prediction than C2. The pulse height cuts in the DST program for flagging whether a cell contained light were checked and discounted. Too high a cut coupled with the low pulse heights could have artificially raised the apparent threshold. Actually the cuts need not be so precise and a cut at ADC channel 30 was adequate for all cells. Software problems were thus ruled out.

After the last run of BC72/73 and before the first run of BC75 the Cerenkov system was physically removed by crane. It has therefore, been suggested that a severe jolt or strain during this (although none were observed) may have shifted the mirrors of C1 out of alignment. Each set of mirrors was securely locked in position to the frame by two ball joints which otherwise would have allowed the mirrors to rotate horizontally or vertically. Again C1 would have been much more sensitive to this than C2. Also, the gas may have liquidised at night (normal boiling point ~4°C). However, there was no left/right or up/down asymmetry in the behaviour of C1, or indeed in C2. Furthermore, when the counters were eventually dismantled no apparent problems were evident. Examination of fitted events to $\gamma p \rightarrow p\pi\pi$ (including events from BC76) further confirmed the behaviour of C1.

Figure 35 shows differences between the counters in their pressure behavior during the spring run, but since the counters were not a closed system interpretation of the pressure limits are difficult. Prior to the start of the autumn run the gas vent pipes, previously connected, were separated and their heights checked. Both counters were 'flushed' thoroughly (3 times) to ensure that the air was purged out, and at intervals during the autumn run C1 was further flushed. Freon-114 has a distinctive odour and was clearly bubbling into and venting from the outlet pipes, and not leaking into the experiment building. A search for leaks proved fruitless but despite the precautions the behaviour of C1 remained unchanged.

As a result only C2 was used for particle identification purposes for the charm candidates and on an individual basis (a program was written which recalculated most DST quantities). In conclusion, evidence favours air entering C1 and creating a freon/air mixture, though not necessarily through some unlocated leak (for example, the expansion of C2 forcing gas out of C1?). It must be emphasized that the C1 problem should not overshadow the success of the main counter C2 which performed entirely as required.

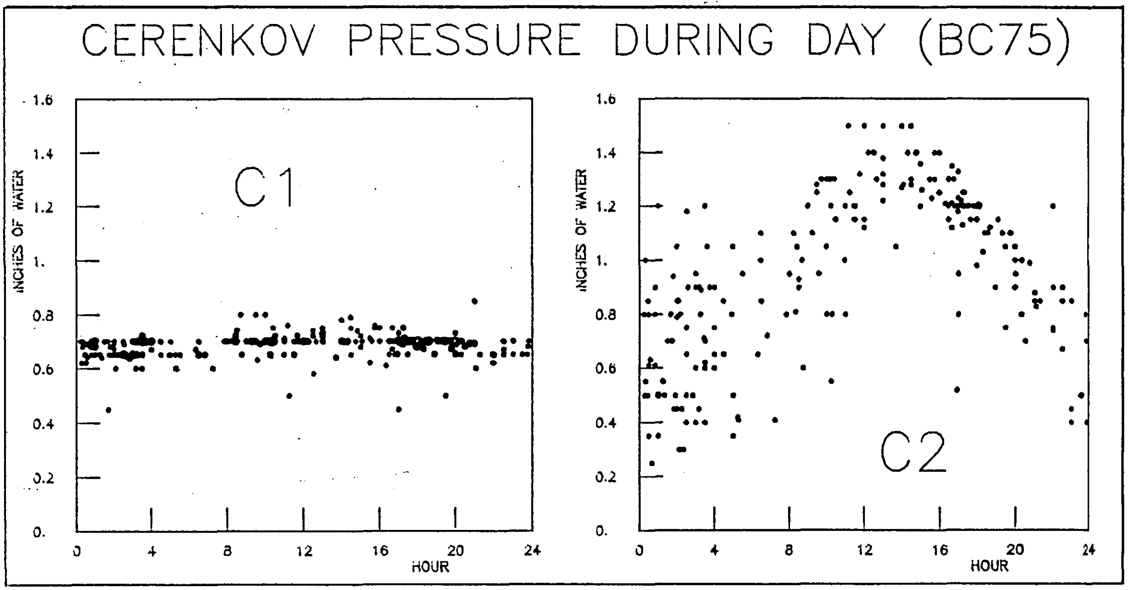

Figure 35: Gas Pressure Behaviour

Chapter V

PHOTOPRODUCTION CONCEPTS AND INCLUSIVE MODELS

This chapter presents phenomenological aspects of photoproduction theory, from an experimentalist viewpoint, relevant to the results reported in the following chapters on ϕ production and inclusive studies. ϕ photoproduction is discussed within the Vector Meson Dominance model together with the mechanism of helicity conservation. The quark-parton model of Recombination which describes hadronization in soft processes (low momentum transfer) is discussed in comparison to Fragmentation. Initially however, it is interesting to comment on the uniqueness of the photon. It can exhibit a two component structure whereby it can interact directly through a pointlike coupling or indirectly through its hadronic component which dominates in real photoproduction ($Q^2=0$).

5.1 DUAL NATURE OF THE PHOTON - POINTLIKE AND HADRONIC

Pointlike interactions are considered 'hard scattering' recognised by high Pt products. Figure 36 shows the lowest order diagrams for the basic processes. The first process, 'QED Compton', is the deep inelastic Compton scattering of the incident photon resulting in a direct (prompt) photon in the final state. The second, 'QCD Compton', is similar except that

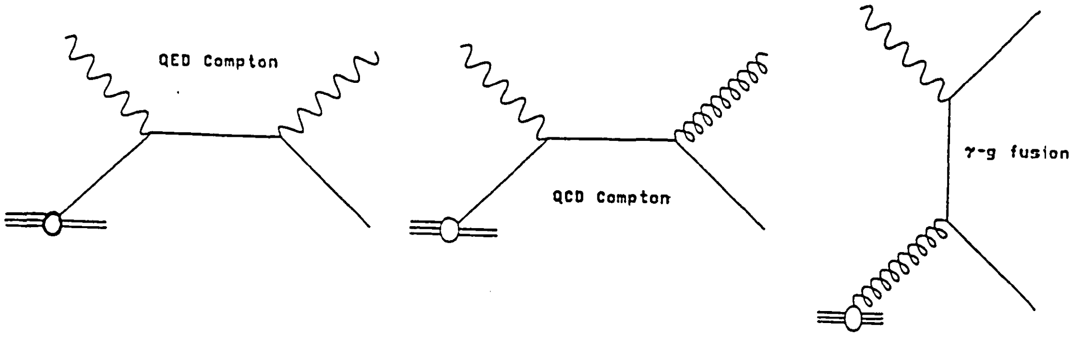

Figure 36: Pointlike interactions of the Photon

the final state photon is replaced by a gluon. The third process, photon-gluon fusion, is the QCD equivalent of the familiar Bethe-Heitler pair production process.

The hadronic nature of the photon can itself be further divided into two components (see figure 37).

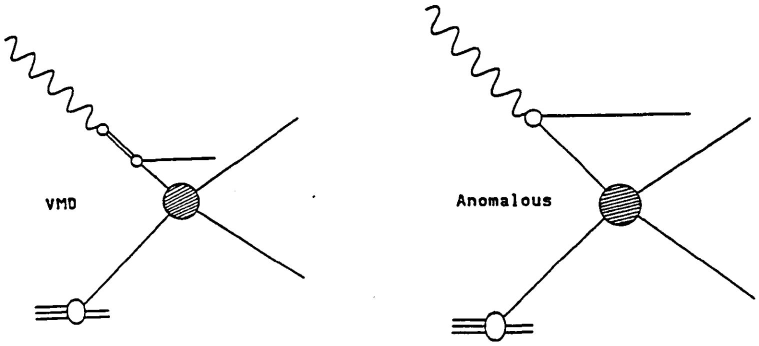

Figure 37: Hadronic interactions of the Photon

In the first process the photon manifests itself as a quark-antiquark pair, which through soft gluon exchanges build up a form factor, becoming in effect a vector meson. Consequently, the photon interacts here as a vector meson and accounts for the dominant mechanism for photon induced reactions at low Pt, and anticipates the discussion on VMD later. In the second process, the quark-antiquark pair interacts with the target before soft gluon exchange has built a form factor. Here the photon has an "anomalous" structure function which grows as $\ln(Q^2)$ in contrast to the VMD structure function which behaves as $1/\ln(Q^2)$ [40].

5.2 THEORETICAL INTEREST IN ϕ PHOTOPRODUCTION

Interest in vector meson photoproduction is connected with fundamental theoretical problems such as photon-hadron coupling and the diffractive scattering of hadrons (see [41]). It is well established that elastic photoproduction conserves helicity in the s-channel (SCHC) as observed in the diffractive process $\gamma p \rightarrow \rho^0 p$ [42]. Indeed this may even be an essential feature of diffractive processes [43]. Our experiment has a polarized beam which consequently permits a test of SCHC, eg, using the ϕ. Also of interest are higher mass resonances such as ϕ', predicted by both Regge Theory and as radial excitations in the Quark Model. Of more recent interest is the observation that $F \rightarrow \phi\pi$(1970).

5.2.1 Vector Meson Dominance

The vector meson dominance model describes an equivalence between the amplitude of the photon induced reaction $\gamma N \rightarrow VN$, and that caused by a transversely polarized vector meson $V_t N \rightarrow VN$ ie:

$$A(\ \gamma N \rightarrow VN\ ) = \sum_{V} \sqrt{(\ \alpha\pi\gamma_V^{-2})}.A(\ V_t N \rightarrow VN\ )$$

where a is the fine-structure constant, $\gamma_V^2/4\pi$ is the γ-V coupling constant, and V_t represents the transversely polarized vector meson ρ, ω, ϕ† (contributions from the J/Ψ family, etc, can be neglected at our energy). Similarly, the corresponding differential cross-section is given by:

$$\frac{d\sigma(\ \gamma N \rightarrow VN\ )}{dt} = a\pi\gamma_V^{-2} \cdot \frac{d\sigma(\ V_t N \rightarrow VN\ )}{dt}$$

Elastic photoproduction of vector mesons, such as the ϕ from protons can then be regarded as the virtual vector meson scattering off the proton to become a real vector meson observable through its decay products (see figure 37,38).

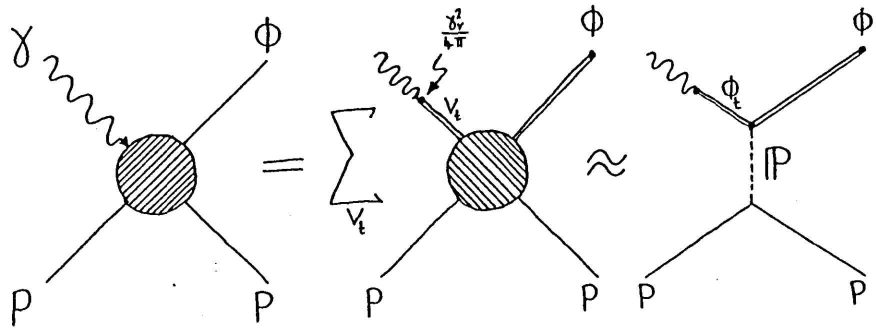

Figure 38: Elastic ϕ Photoproduction (VMD)

The Quark-Parton model and SU(3) assignment of the ϕ is as a pure $s\bar{s}$ pair (though this cannot be completely true since $\phi(1020) \rightarrow \pi^+\pi^-\pi^0$ with BR 16%) and (so) the OZI rule predicts that direct interactions of the ϕ with particles built only from non-strange valence quarks are strongly inhibited [44].

---

† The idea that processes such as $\rho\rightarrow\phi$ are considered negligible represents the idea of 'Diagonal VMD'.

Consequently, since there are no strange s- and u- channel resonances which could couple to the ϕ, only the t-channel exchanges with CP=++ and I=0 (as required by charge conjugation invariance) can contribute, ie, only the pomeron $\mathbb{P}$, f(1270) and f'(1514). In fact the latter are suppressed [45] so that elastic ϕp scattering is considered to be dominated by pomeron exchange.

The Optical theorem further allows VMD to relate the differential cross-section for vector meson photoproduction to the total meson production cross-section (see [46]) and also $\sigma(\gamma p)$(total) to $\Sigma\sigma(Vp)$. However, summation over the lightest neutral vector mesons accounts for only 80-90% of the observed cross-section and so implies that the original assumptions of VMD were too restrictive (and has led to extended VMD models known as Generalised VMD [4]).

The discrepancy between the total cross-section and VMD could allow for the existence of further vector mesons not included in the summation (for instance the $\rho'(1600)$ is well established and has been reported by our collaboration [47]). However, this does not preclude alternatives such as the photon coupling either to a continuum of non-resonant states, or directly to a quark-antiquark pair which then 'dress' to give the observed final states. Indeed, distinguishing between these may not even be possible.

As well as VMD the parton model is quite successful in relating elastic cross-sections, in particular the Additive Quark model [48] predicts for the ϕ:

$$\sigma(\phi p) = (\alpha\gamma_V^2/4\pi)(\ \sigma(K^+p) + \sigma(K^-p) - \sigma(\pi^-p)\ )$$

Assumptions within the AQM are used later to model an observed charge assymetry in chapter 7.

5.2.2 Helicity Conservation

Photons carry spin 1 (helicity ±1 for real photons) which must be conserved in interactions. To determine how the spin properties of the photon are conserved in elastic vector meson photoproduction three frames of reference are normally considered: the Helicity frame (s-channel), the Gottfried-Jackson frame (t-channel), and the Adair frame (γp cms). These are defined in detail in Appendix B.

The decay angular distributions $W(\cos\theta,\phi,\Phi)$ of the ϕ meson (or any vector meson) produced from polarized photons can be described by nine independent spin-density matrix elements ρ_{ij} as detailed in Appendix B. Further it can be shown that for linearly polarized photons if the ϕ carries the same helicity and polarization as the incident photon (ie, conserved in the s-channel: SCHC) then in the Helicity frame (see figure 39) W reduces to:

$$W(\cos\theta,\psi) \propto \sin^2\theta(\ 1 + P(\gamma)\cos(2\psi)\ )$$

where θ,ϕ = polar,azimuthal angle of K^+ in the ϕ rest frame
Φ = azimuthal angle of the photon electric field vector projected onto the Helicty x-y plane,
$\psi = \phi - \Phi$ (see figure 39)
$P(\gamma)$ = linear polarization of the photon ($0 \leq P(\gamma) \leq 1$)

However, as outlined in Appendix B conclusive proof of SCHC requires a calculation of all the ρ_{ij} using each of the three frames (which differ only in the choice of the quantisation axis z), but was prevented in our case due to limited statistics.

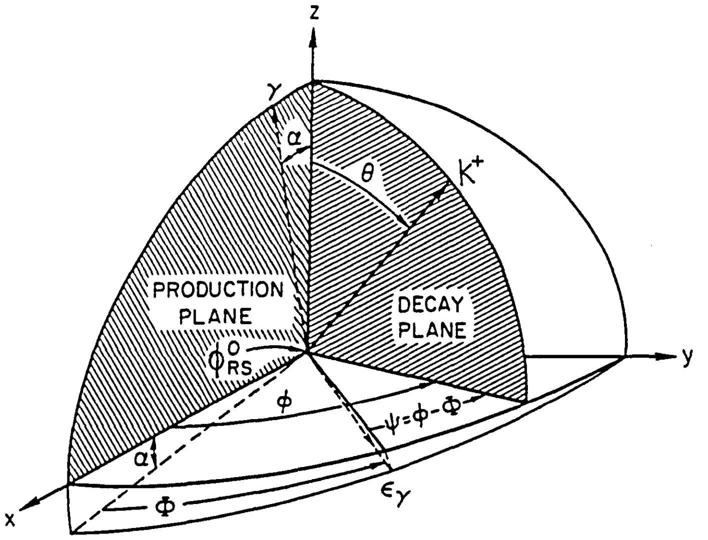

Figure 39: Helicity frame for the study of φ Decay

The nature of the t-channel exchanges may be observed by calculating the 'Parity Asymmetry' parameter P(σ) defined as:

$$P(\sigma) = \frac{\sigma(n) - \sigma(u)}{\sigma(n) + \sigma(u)} = 2\rho_{1-1} - \rho_{00}$$

where σ(n), σ(u) are the cross-sections for the exchange of natural (ie $P=+(-1)^J$) and unnatural (ie $P=-(-1)^J$) parity in the t-channel. Clearly SCHC, understood as predominantly pomeron exchange (JPC=0++), requires natural parity exchange in the t-channel ie, $P(\sigma)\to+1$. The spin density matrix elements may be calculated from the angular distributions, for instance using the Method of Moments [49]. For a JP=1- decay:

$$\rho_{00} = (5\overline{\cos^2\theta} - 1)/2$$

$$\rho_{1-1} = -\tfrac{5}{4}\,(\overline{\sin^2\theta\cos2\phi})$$

5.3 MODELS FOR INCLUSIVE SOFT PARTICLE PRODUCTION

In order to place within some context the results reported in chapter 7, the general background surrounding the competing ideas of Recombination and Fragmentation will be discussed from an experimental rather than theoretical viewpoint, (not least to keep the discussion short). For a comprehensive survey of all current quark-parton models for particle production with low momentum transfer see references [52].

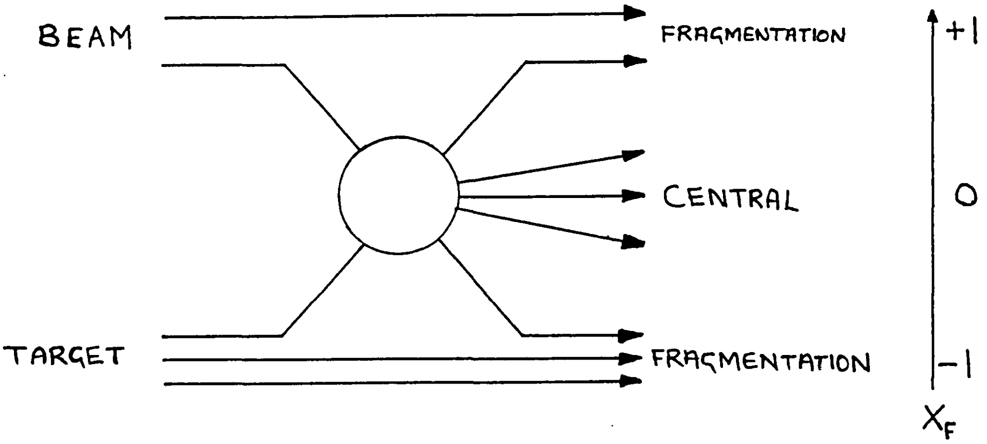

Figure 40: Representation of Feynman-x Regions

It is essential to introduce the dimensionless variable Feynman-x (Xf or just x): $x = P_l/P$ $(-1 < x < +1)$, which measures, in the centre of mass, the fraction of the beam momentum (P) which is carried as the longitudinal component (P_l) of the detected particle (see figure 40). A typical cross-section plotted as a function of x shows a large number of particles produced about x = 0 (slow moving) which decreases to zero, like $(1 - x)^n$, as $x \to 1$. The shape of the x distribution has been observed to be essentially independent of energy - an effect generally known as 'Feynman Scaling'. The value of the exponent n is an important test of the various models.

It is also convenient to introduce the 'rapidity' variable, where rapidity = 0.5 log($(E+P_l)/(E-P_l)$), which clearly depends on the frame of reference but has the advantage of being additive under a Lorentz boost.

The theoretical interpretation of low Pt fragmentation is open to debate and attracts much controversy. Broadly speaking, the existing models can be described as either using the 'quark fragmentation' approach or the 'quark recombination' approach, which have very different dynamical viewpoints. In fragmentation models a valence quark from the beam is assumed 'held back' and the inclusive distribution described by a set of 'fragmentation functions', $D_q^h(x)$, of the remaining fast forward quark (or diquark). The inclusive distribution in the recombination approach is described by the 'structure function', $f_H^q(x)$ of a fast forward valence quark which recombines with a slow sea quark to form the final state particle. Despite obvious differences there is reason to consider these models equivalent interpretations, but at best they may be only approximations to the underlying QCD mechanisms (assuming QCD is correct and also calculable).

In hadron-hadron scattering the central region is heavily populated by slow moving particles from which it is reasonable to assume that these particles are relatively independent of the beam and quark quantum numbers, (and has lead to quark combination models predicting particle yields [53]). As x→±1 (beam and target fragmentation regions), the produced particle carries a large fraction of the incident longitudinal momentum of the incident hadron, and therefore, the observed spectrum should reflect the quantum numbers of the fragmenting particle. In our experiment, the average charge in the beam fragmentation region (x→+1) is then expected to be zero, in conflict with the results reported in chapter 7.

5.3.1 Fragmentation Ideas and Counting Rules

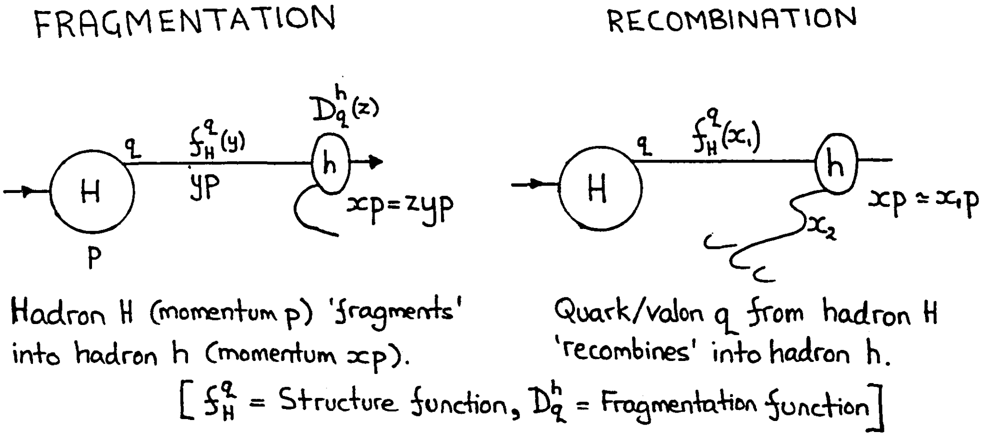

Figure 41: Fragmentation versus Recombination

Discussion of problems associated with naive fragmentation assists the popularity of the recombination approach which may be argued to have a more natural appeal to quark subprocesses. Both views are represented pictorially in figure 41. Fragmentation supposes a quark to 'fragment' in such a way as to lose momentum in two stages, which can be best illustrated by example. For instance, the fragmentation mechanism would write the inclusive cross-section for $pp\rightarrow\pi^+X$ as:

$$\sigma^{-1}\, d\sigma/dx(p\rightarrow\pi^+) = \int_x^1 f_p^u(y) D_u^{\pi^+}(z)\, dy$$

where $f_H^q(y)$ = Structure function. Valence quark carries momentum fraction y of the proton, and
$D_q^h(z)$ = Fragmentation function. Quark fragments to hadron carrying fraction x=zy.

However, Das and Hwa [6.2] have shown that this yields predictions more than an order of magnitude below the data whereas Recombination predictions agree quite well as shown in figure 43.

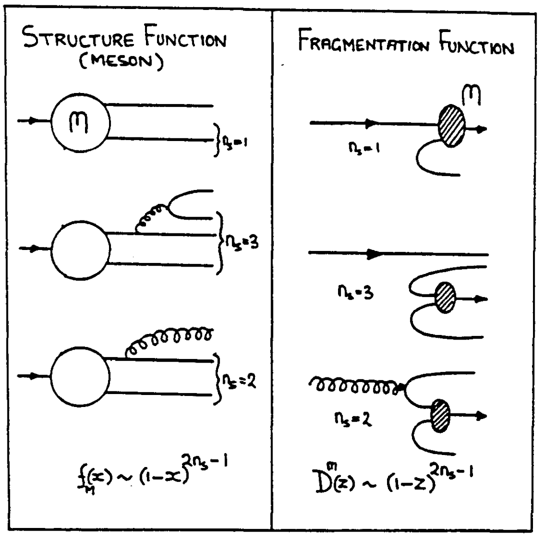

Figure 42: Dimensional Counting Rules

The form of the structure and fragmentation functions may be estimated by introducing Dimensional Counting Rules which count spectator quarks. In the limit $x\rightarrow1$ it would appear that a single parton would have to carry all the momentum of a hadron, but since this is impossible the structure function $f_H^q(x)$ must vanish. However, as $x\rightarrow1$ all other quarks (ie, spectator) must have vanishing momentum requiring hard gluon exchange to transfer their momenta to the fast valence quark (allowing some QCD calculations). Thus, Brodsky et al [54] have shown that this allowed them to develop a 'dimensional counting rule':

$$\text{limit } x\rightarrow1 \quad f_H^q(x) \simeq (1-x)^{2n_s-1}$$

where n_s is the minimum number of other partons whose momentum must vanish as $x\rightarrow1$. Referring to figure 42, a valence quark in a meson, for instance, is accompanied naively by one antiquark, and so $n_s= 1$ with $f_M^V(x)\simeq(1-x)^1$, for a sea quark $n_s= 3$ with $f_M^S(x)\simeq(1-x)^5$, and for a gluon $n_s= 2$ with $f_M^g(x)\simeq(1-x)^3$. Thus in the example $pp\rightarrow\pi^+X$ these rules predict $f_p^v(y)\sim(1-y)^3$ and $D_u^{\pi^+}(z)\sim(1-z)^1$ giving: $d\sigma/dx(p\rightarrow\pi^+) \sim (1-x)^5$, where experimental results indicate a behaviour closer to $(1-x)^3$. Indeed it was this observation by Ochs [55] that has motivated the present Recombination ideas.

The problem with fragmentation is that momentum is lost in two stages ($x=yz$): first (to continue our example), a quark (or antiquark) carries fraction y of the incident proton momentum, which then 'fragments' into a π^+ together with other particles, and therefore, must compete for a share z of the momentum. The various models of fragmentation overcome this difficulty by introducing a mechanism known as the 'quark held back' effect. This assumes a valence quark is held back in the central region ($x\simeq0$) allowing the other quark to fragment as if it carried all

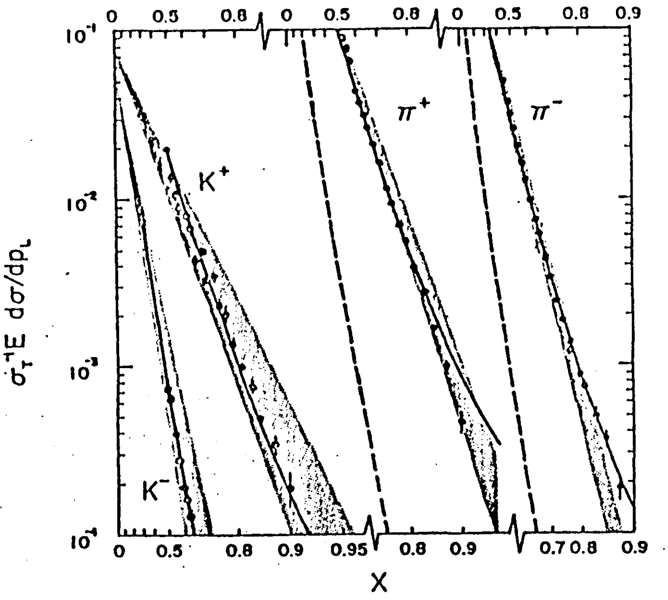

Longitudinal momentum distributions for charged mesons. Shaded regions represent extrapolation from data. Data points are for a p_T of 0.6 GeV/c with normalisation to fit within the shaded regions. Dashed lines are π^+ and π^- production due to quark fragmentation and solid lines correspond to the recombination process.

Figure 43: Comparison of Fragmentation & Recombination with Data
The figure is taken from reference [6.2]

the momentum with the result that the fragmentation models regain agreement with data.

Though fragmentation and recombination are different mechanisms this 'held back' effect brings them closer together. However, the naive version of the Recombination model cannot operate initially in e^+e^- annihilation since the produced quarks are 'bare', and it is not until these have 'dressed' themselves that the recombination mechanism may occur. In contrast this is where the Fragmentation model is most successful and where the fragmentation functions are measured (Anderson et al [6.1]). This should be taken as a reasonable hint to separate the processes of interaction and hadronization with the latter dependent upon the former.

5.3.2 The Recombination Approach

The original idea for the quark recombination model (QRM) was formulated by Goldberg (1972) and revived by Ochs (1977) [55]. The basic idea, as already stated, is that a fast valence quark ($x_1 \to \pm 1$) from the initial hadron 'recombines' with a slow antiquark ($x_2 \sim 0$) from the sea. Thus, the produced hadron has $x = x_1 + x_2 \simeq x_1$ and so, returning to the example $pp \to \pi^+ X$

$$d\sigma/dx(p \to \pi^+) \sim f_p^u(x) \sim (1-x)^3$$

in reasonable agreement with experiment (see figure 43) and in contrast to the original predictions of fragmentation. In fact the present impetus for the popularity of the recombination model comes from the observation by Ochs that the charged particle/antiparticle ratio agreed with the following:

$$\frac{d\sigma/dx(p \to \pi^+)}{d\sigma/dx(p \to \pi^-)} \sim \frac{f_p^u(x)}{f_p^d(x)}$$

The model has evolved in time but in its general form it can be expressed as:

$$\sigma^{-1}\, d\sigma/dx(H \to h) = \int^1 F(x_i) R(x_i, x) \delta(\Sigma x_i - x) \prod_i dx_i$$

where F describes the probability of finding appropriate quarks with x_1, x_2 if h is a meson, or x_1, x_2, x_3 a baryon,
R describes the probability that they recombine into hadron h,

The form of F and R are theoretically arbitrary, for instance in the standard approach of Das and Hwa F was chosen as:

$$F(x_1, x_2) = f^V(x_1) f^S(x_2) \rho(x_1, x_2)$$

where this is for fast meson production and $\rho(x_1, x_2)$ is a phase space factor. Even this is arbitrary and they chose (ad hoc) $\rho \simeq (1-x_1-x_2)$ as $x_1 + x_2 \to 1$. The arbitrariness has led to several choices by various authors, see for instance Takasugi et al [56]. The recombination function itself is apparently even more arbitrary. The standard choice is $R(x_1,x_2,x) = x_1x_2x^{-2}\beta$ where β is a constant (which may even be a function of x_1 and x_2!). Chang and Hwa [57] have made calculations supporting this choice using photoproduction.

The development of the recombination model has progressed along various lines (eg, [58]), but the most popular version (theoretically) is the 'Valon' model of Hwa [59]. In this model the hadrons are composed of 'valons', ie, constituent valence quarks accompanied by their virtual cloud of quarks and gluons. In soft hadronic collisions one of the valons in each hadron interacts and initiates the fragmentation of other valons into partons. These provide a source of antiquarks for the recombination process which then reforms valons into the forward hadrons. Obviously this model appears much more complicated and at present has not developed far enough for application to various processes.

Application of these ideas to photoproduction is not as easy as with meson beams, but assuming the photon to interact like a hadron then together with dimensional counting rules this allows a prediction for the inclusive x distribution:

$$d\sigma/dx(\gamma p \rightarrow hp) \propto (1-x)^1$$

which should apply to both <u>pions</u> and <u>kaons</u>. Indeed, earlier results using pions [18.2] were very encouraging.

5.3.3 Considerations for the Fragmentation Regions

It is interesting to note that some authors [60] have made calculations for a pointlike photon which would suggest that a pointlike photon would give a $(1-x)^0$ behaviour in the limit $x \to 1$, and so would be a source of high x quarks. However, resonance production complicates the distribution since it can produce fast decay products especially from diffractive events in photoproduction. Figure 44 shows the effect of resonances on the x distribution in our experiment?

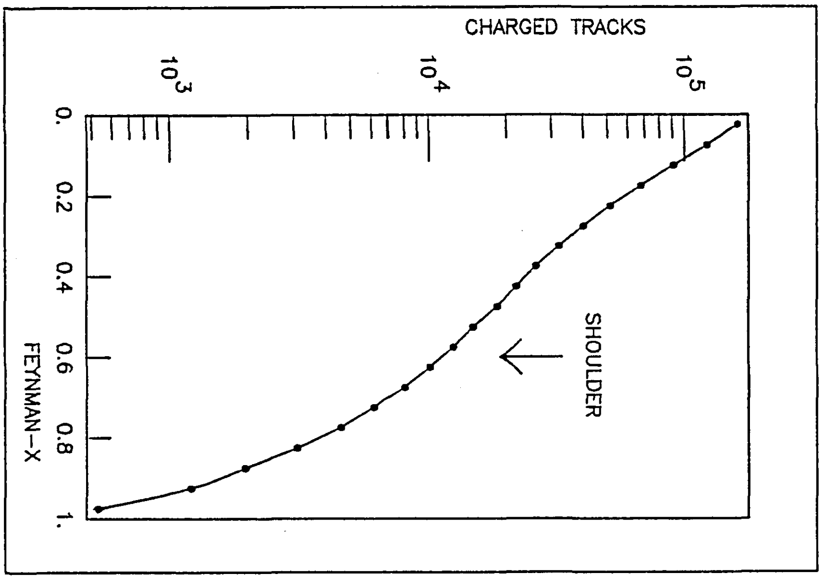

Figure 44: Resonance effects on x Distribution
The forward 'shoulder' is a result of resonance decay products.

It is of interest to end this discussion with the main idea behind the 'quark fusion' models, which considered within the recombination process are used in the interpretation of the results in chapter 7. These consider the probability of finding final state hadrons containing quarks from both colliding hadrons and have indicated that removing valence quarks by fusion or annihilation is an important process at low energies. Consequently, this must have some effect on inclusive distributions and even supply a mechanism for the recombination or fragmentation models. In this respect there is an important result observed by Buschbeck et al [61] that target fragmentation in hadron-proton collisions, and in particular the π^+/π^- ratio as a function of x, depends still on the beam hadron. Some of their results are shown as figure 45 and illustrate that their conclusions apply at reasonably high energies. Since the beam affects the target fragmentation region then, equivalently, the target must affect the beam fragmentation region, as will be shown to be the case in our experiment.

Naturally, at some high energy, the target fragmentation region should be independent of the beam and vice-versa just as the central region should be independent of both. However, the Buschbeck et al results suggest that 'fusion contamination' becomes negligible only at high energies ($\sqrt(s) \sim 20 - 30$ GeV). This should be seen as a caution in the use of models which assume the independence of beam and target fragmentation. Indeed, all the models of fragmentation and recombination have predicted distributions with this assumption. The results from our experiment, reported in this thesis for photon-proton collisions with $\sqrt{s} \sim 6$ GeV, further support this warning as will be demonstrated.

Inclusive π^+/π^- Ratio v. Feynman-x
(Buschbeck et al)

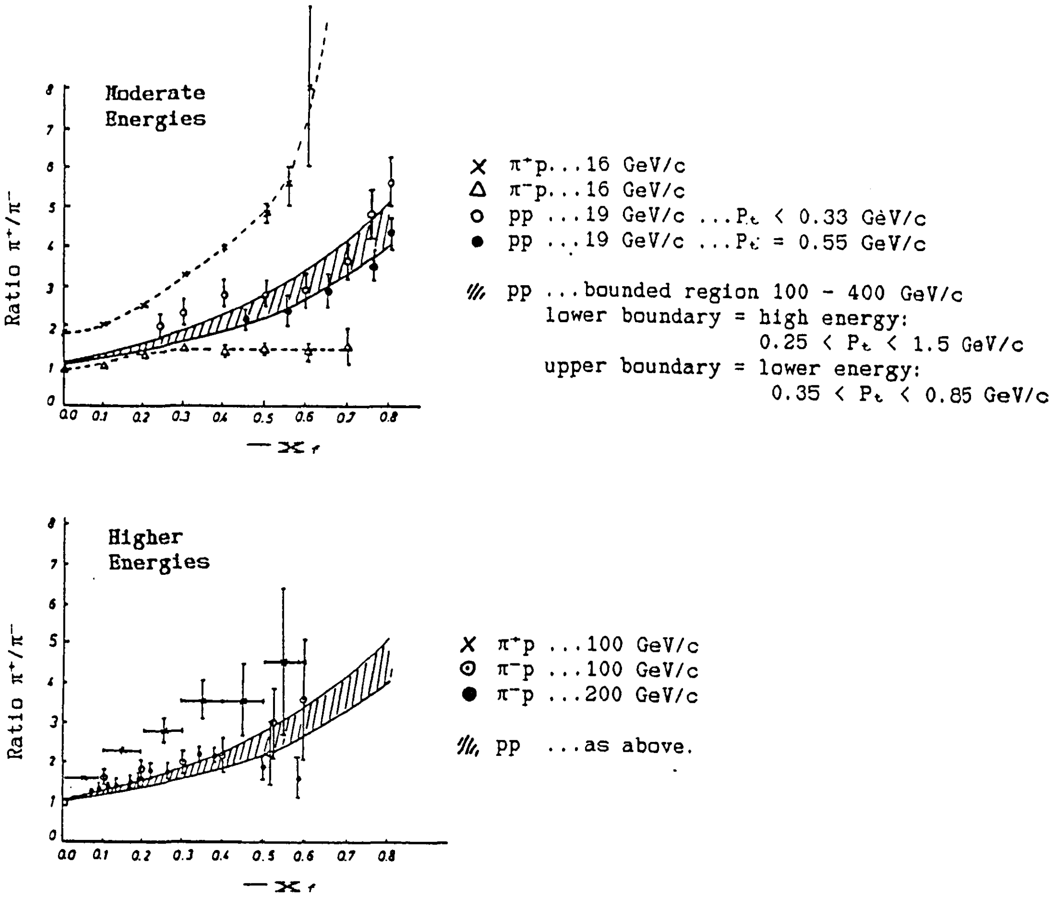

Figure 45: Beam effects on Target Fragmentation Region
These results are quoted from reference [61].
Bushbeck et al compared the inclusive π^+/π^- ratio in πp and Kp reactions at different energies to that of pp reactions. They reported a significant dependence on the beam quantum numbers for this ratio in the target (proton) fragmentation region. Since the naive recombination model cannot account for this effect they suggested that valence quark annihilation with subsequent recombination as an additional mechanism.

Chapter VI

ELASTIC AND INELASTIC ϕ PHOTOPRODUCTION

The photoproduction of ϕ mesons has been studied over a wide range of photon energies (up to ~180 GeV)[62]. The results reported in this chapter are based on the analysis of K^+K^- pairs at 20 GeV with an invariant mass in the $\phi(1020)$ mass region, and was concerned with the following two reactions:

$$\gamma p \rightarrow \phi p \rightarrow K^+K^-p$$

which will be referred to as 'elastic ϕ photoproduction' (in the VMD picture), and:

$$\gamma p \rightarrow \phi X \rightarrow K^+K^-X \text{ where } X \neq p$$

which will be referred to as 'inelastic ϕ photoproduction'.

6.1 ELASTIC ϕ PHOTOPRODUCTION

The total 3 prong sample consisted of ~118000 events before cuts. All 3 prongs were run through the kinematic fitting program as described in section 3.2.1 and so presented a natural way to select the $\gamma p \rightarrow pK^+K^-$ events using the 3C fits. However, the above reaction is kinematically similar to $\gamma p \rightarrow p\pi^+\pi^-$ so measurement errors may allow an event to have multiple successful fit(s) to different reactions. Therefore, a second method was also used, much simpler than the first, being a set of simple kinematic cuts, which would minimise any biases introduced. A major difference between the two approaches is that fit selection would also select the non-resonant pK^+K^- events whereas the alternative method will select only the ϕ events.

6.1.1 Acceptance

The estimation of the acceptance of the selection procedure/detector is a vital step in the calculation of any cross-section and is performed using the Monte-Carlo technique, which necessarily involves assumptions about the process under study. In this case ($\gamma p \rightarrow \phi p$) elastic ϕs were generated randomly from an exponential momentum transfer (t) distribution with a slope of 5.0 (as suggested by other experiments [62]), and uniformly around the beam. The ϕ was then allowed to decay to K^+K^- isotropically, but with the angular distributions weighted according to SCHC with an average beam polarization of 50%. The event was then tested for a trigger by 'swimming' the tracks through the SHF and testing against random numbers. Events which 'triggered' were further weighted by the mean scanning and measuring efficiencies for 3 prongs. The results are shown in figure 46 with the acceptance to exist on the DST estimated as $(66\pm4)\%$, remaining constant over the ϕ mass region.

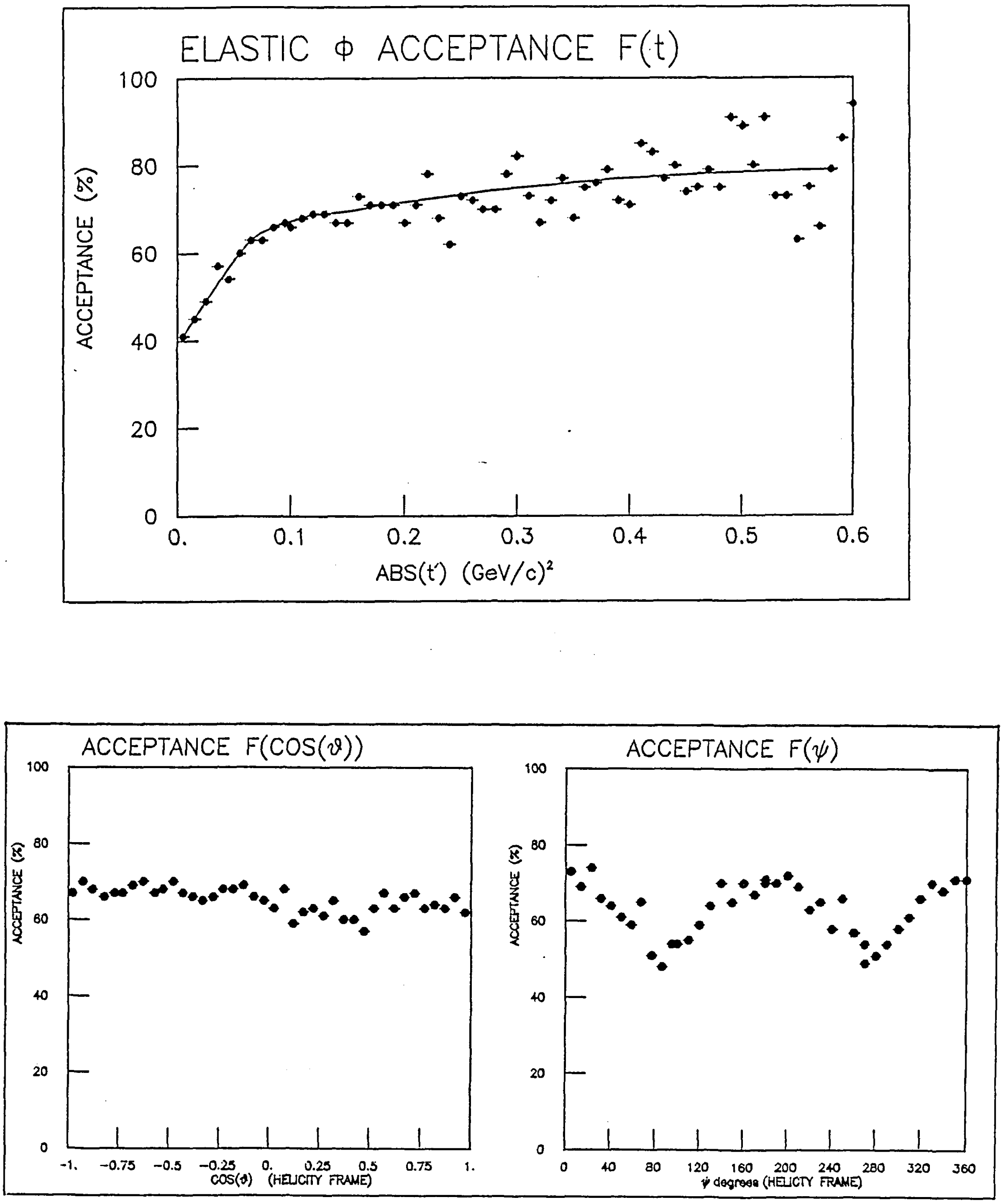

Figure 46: Acceptance of Elastic ϕ events

6.1.2 Cross-Section Calculation (by kinematic cuts)

The major advantage of selecting $\gamma p \rightarrow \phi p$ events through the decay channel $\phi \rightarrow K^+K^-$ is that there are no neutrals to miss and all the charged tracks should be seen on the bubble chamber photographs. However, though proton recoils should be visible at ~75MeV/c (even less on the HRO), a short proton track (range < 1mm) may be missed, and therefore the 2 prong sample was examined.

The 2150 2 prong events were shown to be mostly beam conversions by examining the e^+e^- mass plot, which shows a spike at $m(e^+e^-) \sim 30$ MeV/c, and the total transverse momentum plot which shows a spike along the beam axis. Eliminating these with a cut at $m(e^+e^-) < 100$ MeV/c^2 leaves 471 events which potentially could contain a ϕ. The $m(K^+K^-)$ plot shows 21 events in the ϕ region allowing an upper estimate of < 4 events in this sample.

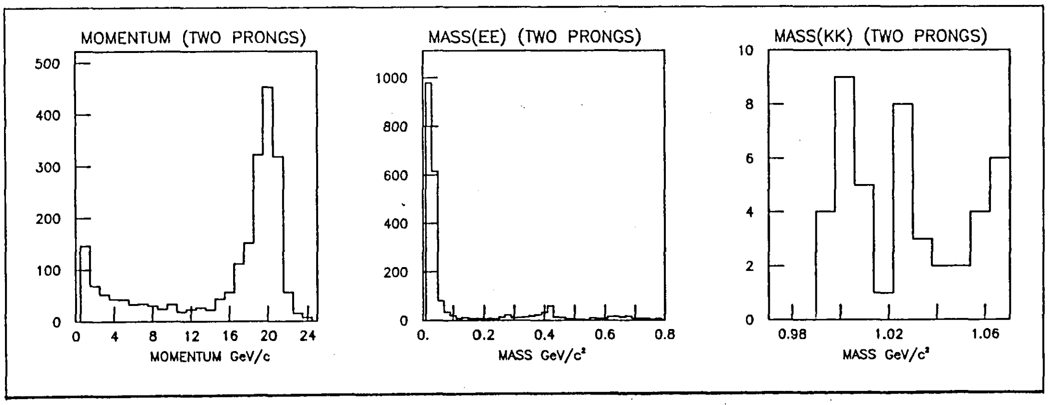

Figure 47: Possible losses via slow proton

The main data sample consists of ~114255 3 prong events in the roll range 300-2531 passing vertex cuts, of which 14792 were flagged as containing a V°. In this sample 5160 events were rejected which contained at least one track with 1/p = 0.0 (ie flagged as unmeasured, of which 25% were kink tracks). This gave a loss of (4.5±0.1)% consistent with that expected from secondary interactions. In the remaining sample 708 events which had one track with an unassigned charge (for instance, due to the straightness of the track), were easily resolved, but 193 events remained ambiguous (0.20±0.01)%, and were removed. Finally the remaining events were subject to the main kinematic cuts:

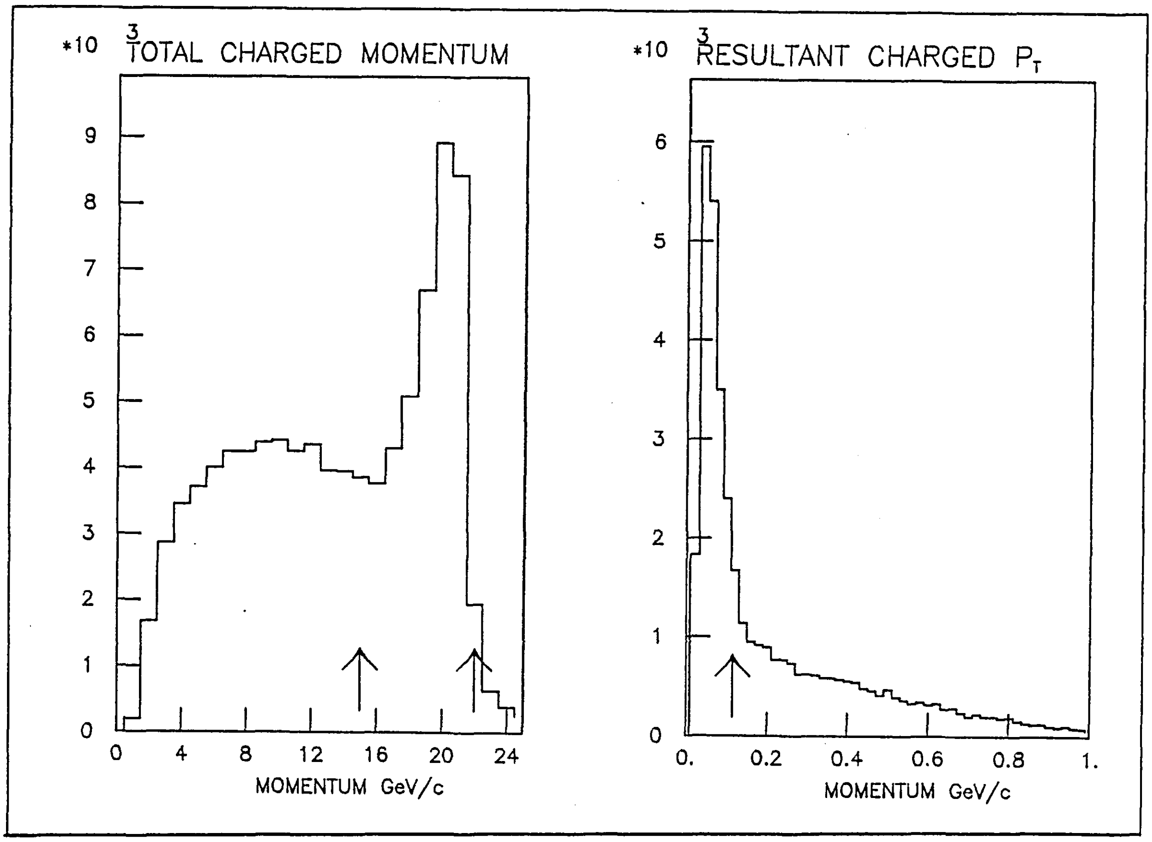

Figure 48: Momentum cuts on 3 prong sample

a) The total charged momentum was required to be in the range 15.0 - 22.0 GeV/c to remove events with neutrals. However, since the photon energy is not known this would not remove all such events and left a sample of 41662 events, of which 2516 were flagged with a V^0. These V^0 events were removed and plotted separately to check for losses due to unassociated V^0s or γs, indicating a loss of (6.0±0.1)%.

b) The photon beam lies along the x-axis and therefore if there are no missing neutrals then the resultant charged Pt should be about zero. Allowing for measurement errors a cut at 115 MeV/c (supported by the 3C fitted events) was used leaving a sample of 20397 events. Running the program on the 3C fitted $\gamma p \rightarrow \phi p$ events suggests this cut introduces a loss of (3.9±1.3)%. The overall identification efficiency is, therefore, calculated to be (56.8±3.5)%.

Using the two forward tracks (+-) the $\pi\pi$ and KK mass combinations were plotted (figure 49). It is interesting to note that a plot of $m(p\pi^+)$ (not shown) indicated a $\Delta^{++}(1232)$ peak on a large background which failed the Pt cut. The $m(\pi^+\pi^-)$ plot shows a dominant $\rho(770)$ peak with a ϕ reflection sitting at ~360 MeV/c^2. The $m(K^+K^-)$ plot shows the $\phi(1020)$ clearly on a rising background which peaks at ~1210 MeV/c^2 corresponding to the ρ reflection.

The events in the ϕ region where the acceptance is constant were fitted to a gaussian and a three parameter polynomial

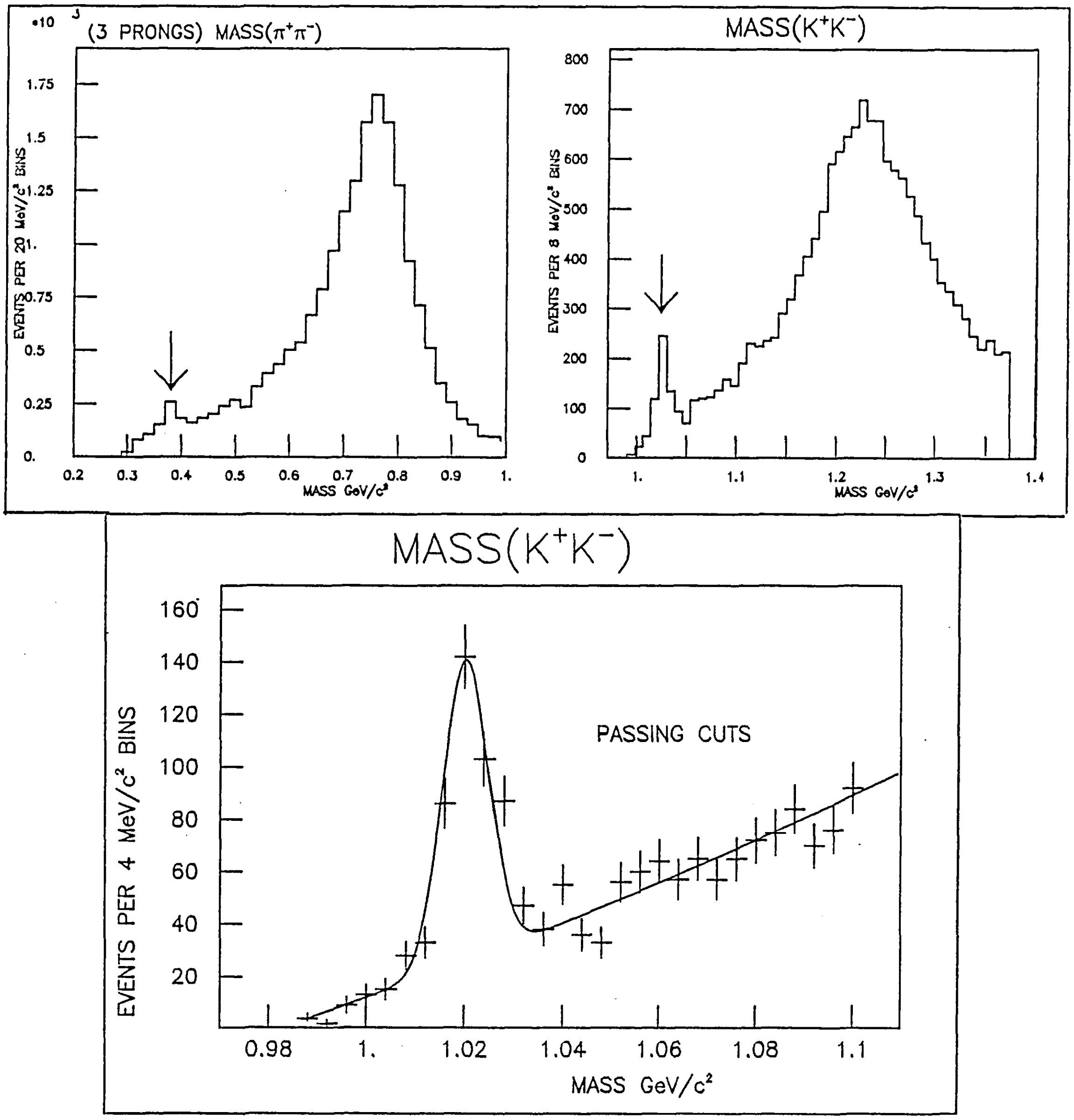

Figure 49: m(K^+K^-) from kinematic cut method

background. After subtracting background, the peak is estimated to contain 350.0 ± 18.7 events. Correcting for losses gives 616.2 ± 50.3 events which using the experimental sensitivity quoted in chapter 3 corresponds to elastic cross-sections of:

$$\sigma(\ \gamma p \rightarrow \phi p\ ).\mathrm{BR}(\ \phi \rightarrow K^+K^-\ ) = 228 \pm 15 \pm 24 \text{ nb}$$

According to [1] BR($\phi \rightarrow K^+K^-$) = (49.3 ± 1.0)%:

$$\Rightarrow \quad \sigma(\ \gamma p \rightarrow \phi p\ ) = 463 \pm 31 \pm 49 \text{ nb}$$

Since the background was so small and well parameterised the Cerenkov counters (which would introduce misidentification and acceptance complications) were not used, so that the above results are calculated with the minimum of bias. However, if the Cerenkovs are used as a consistency check to reject events, then the reduction in background from $p\pi^+\pi^-$ events (ppp is negligible) indicates the number of ϕ events to be consistent with the above.

As an alternative, the cross-section could have been calculated by comparing the number of events to that of a dominant reaction with a known cross-section, for example the reaction $\gamma p \rightarrow \rho p$ with 11.1 ub. However, the $\rho(770)$ peak is wide and skewed (as described by a Drell 'interference' background in the Söding Model [75.3]) which makes the estimation of the number of ρ events non-trivial.

6.1.3 Cross-Section Calculation (by 3C fit selection)

It is reasonable to expect all well-measured genuine pK^+K^- events to succeed in fitting pK^+K^- with some sort of background from other channels. In the roll range 300-2531 there were 3100 3C fits to $\gamma p \rightarrow pK^+K^-$ and 19959 to $\gamma p \rightarrow p\pi^+\pi^-$. Those events with fits to pK^+K^-, but fewer than 3 constraints, therefore represent a loss of (9.0±0.5)%. As already stated a 3C fit has associated with it a χ^2 probability effectively describing the probability that a better fit could be obtained. Figure 50 shows the distribution for 3C fits to $\gamma \rightarrow pK^+K^-$ and is typical.

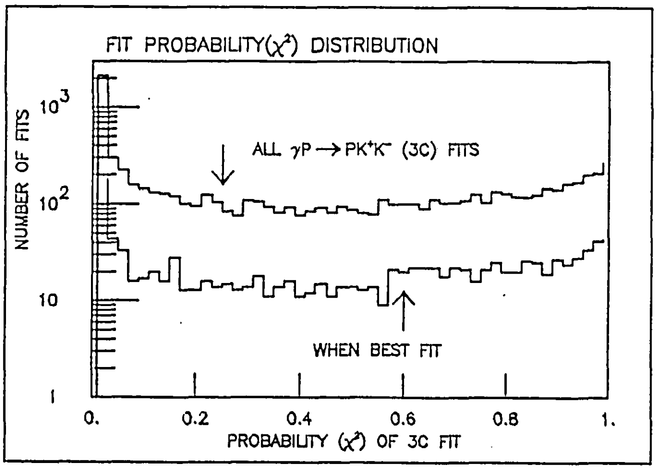

Figure 50: Typical Probablity χ^2 Distribution for 3C fit

The large spike near zero essentially represents incorrect fits which were removed by a cut at $P(\chi^2) = 2\%$. This represented a loss of $(1.9 \pm 0.2)\%$ estimated from the pK^+K^- fits in the range $0.02 < P(\chi^2) < 0.22$.

The remaining 2822 events contained 75% with one pK^+K^- fit (572 were unique fits) and 25% with both permutations (ie '++-' = 'pKK' and 'KpK'). However, 1840 of these events fitted another channel 'best' (ie had the highest $P(\chi^2)$), of which 98.2% were $p\pi^+\pi^-$, and 1.8% $p\bar{p}p$. Using the Cerenkov counters a lengthy investigation of potential differences between the first and second best fits in quantities such as the $P(\chi^2)$s and stretch (pull) distributions found no quantity with which generally to distinguish fits. Of course, the fits with at least one hybrid track could potentially be distinguished by using the Cerenkov counters. However, inefficient pions near threshold and background light for kaons complicate acceptance through misidentification, whereas using <u>all</u> the pK^+K^- fits should lose no ϕ signal, and only increase a background. It was decided to select the best fit, thereby avoiding a series of 'tangled' cuts, giving a total of 982 events which was reduced to 863 after a cut on the fitted beam energy of (15.0 - 22.0), and a very clean ϕ signal (see figure 51).

Examination of the pK^+K^- fits which were not the best fit showed a good ϕ signal in those which were above the $P(\chi^2)$ cut, but no signal above background in those below. The rejected 'good' pK^+K^- fits represented a loss of $(29.5 \pm 3.1)\%$ Furthermore, though 98% of these rejected events fitted $p\pi^+\pi^-$ 'best', only a weak $\rho(770)$ peak was evident. It is of interest to note that 3 prong events with 3C fits to $\gamma p \rightarrow p\pi^+\pi^-$ were used to check the beam spectrum during BC76.

The calculated errors on the mass combinations averaged 3 MeV which is of the order of the ϕ width. Therefore, the m(KK) peak was fitted with a gaussian, since measurement errors were expected to smear the narrow peak. The fit resulted in: $m(\phi) = 1020.5 \pm 0.2$ MeV/c² with $\Gamma(\phi) = 12.5 \pm 2.6$ MeV/c². A Breit-Wigner [63] fit also resulted in: $m(\phi) = 1020.3 \pm 2.2$ MeV/c², $\Gamma(\phi) = 8.3 \pm 2.9$ MeV/c² compared to the Particle Data Book [1] value of $m(\phi) = 1019.5 \pm 0.1$ MeV/c² and $\Gamma(\phi) = 4.22 \pm 0.13$ MeV/c². Subtracting the small background estimated 279.0 ± 16.7 events in the ϕ peak, which when corrected for losses represented a signal of 672.3 ± 64.4 events. Using the sensitivity this corresponds to an elastic cross-section of:

$$\sigma(\ \gamma p \rightarrow \phi p\ ).BR(\ \phi \rightarrow K^+K^-\ ) = 249 \pm 19 \pm 27 \text{ nb}$$

which with BR($\phi \rightarrow K^+K^-$) = (49.3 ± 1.0)% gives a total elastic cross-section of:

$$\Rightarrow \quad \sigma(\ \gamma p \rightarrow \phi p\ ) = 505 \pm 38 \pm 56 \text{ nb}$$

This result is in reasonable agreement with other results as shown in figure 52.

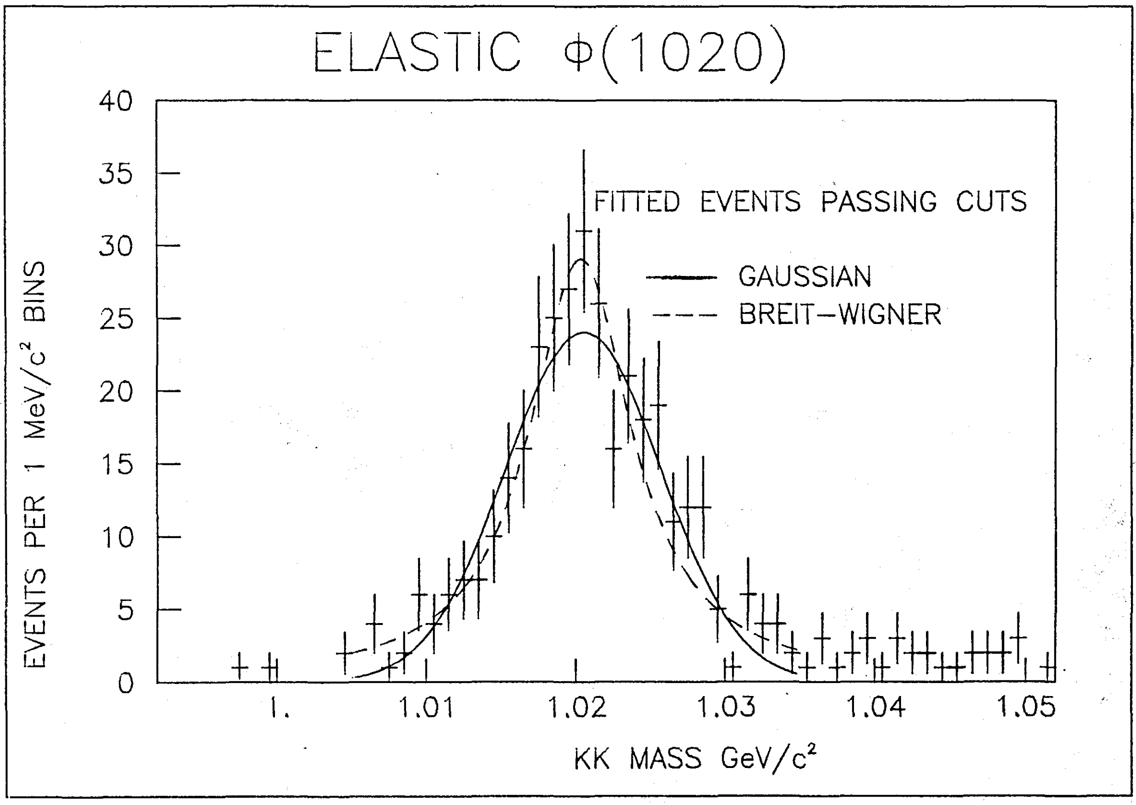

Figure 51: Fitted K^+K^- mass distributions

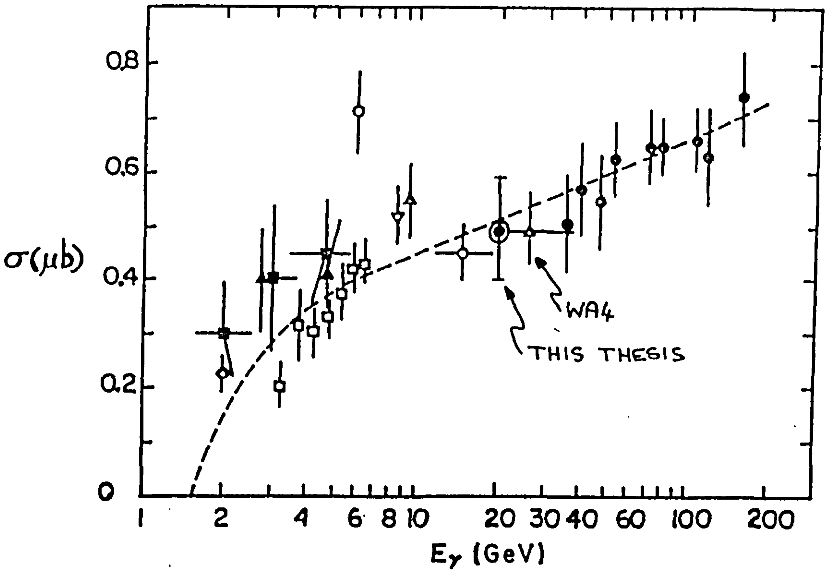

Figure 52: Comparison of ϕ cross-sections
Data and Calculation taken from Egloff et al [62.1]. The dashed curve represents a parameterization of the ϕp photoproduction cross-section based on VMD-Quark model assumptions.

6.1.4 ϕ Production and Decay Properties

Using the fitted ϕ events the t distribution was plotted as t' where t' = t − t(min). Corrected for acceptance a fit of the form $d\sigma/dt' = A \exp(-B|t'|)$ yielded a value of $B = 5.3 \pm 0.2$ (figure 53), characteristic of a diffractive mechanism, and is compared with other results on the right.

Using the fitted events the angular distributions $\cos\theta$ and ψ in the Helicity frame were calculated and plotted in figure 54, corrected for acceptance. The general agreement is good and the fit to the ψ distribution gives an average linear polarization of (45 ± 4)% (compared to the expected value 52% [64]), implying that the production mechanism is at least consistent with SCHC expectations. However, the mean values of the $\cos^2\theta$ and $\sin\theta\cos 2\phi$ distributions (averaged over $|t'| < 0.6$) imply values

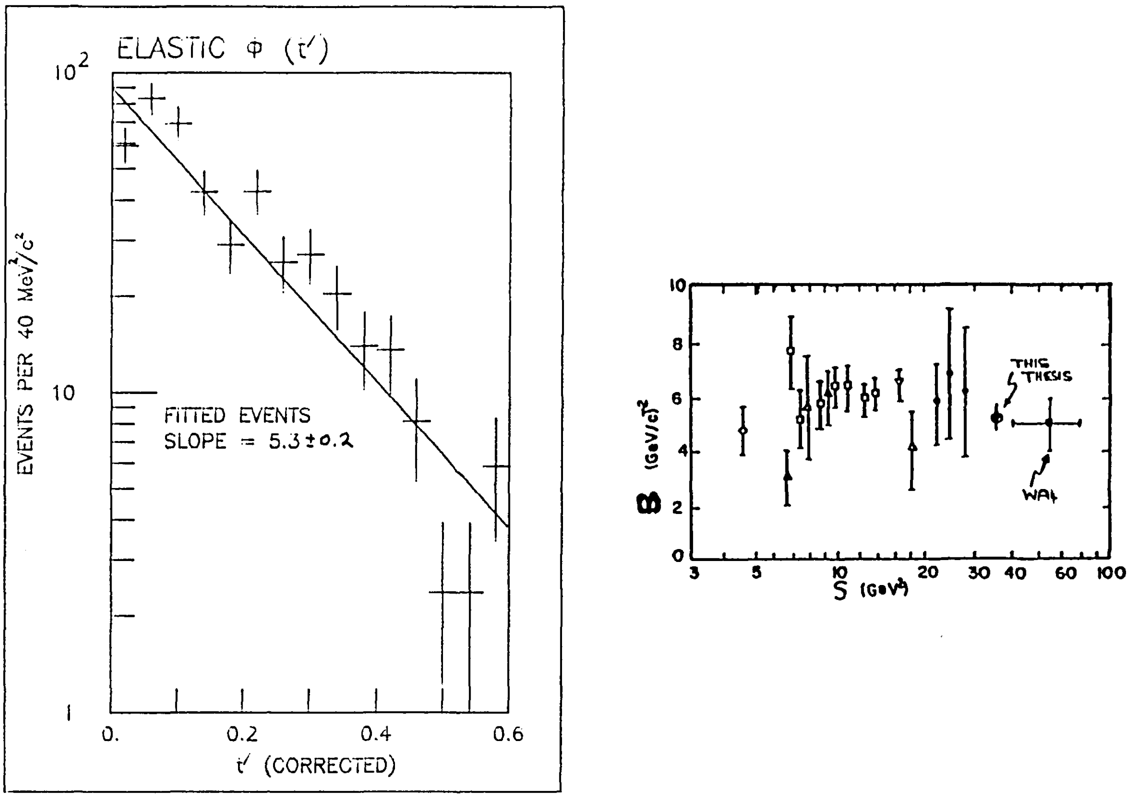

Figure 53: t distribution and slope parameter B. Slope data taken from Aston et al [62.8].

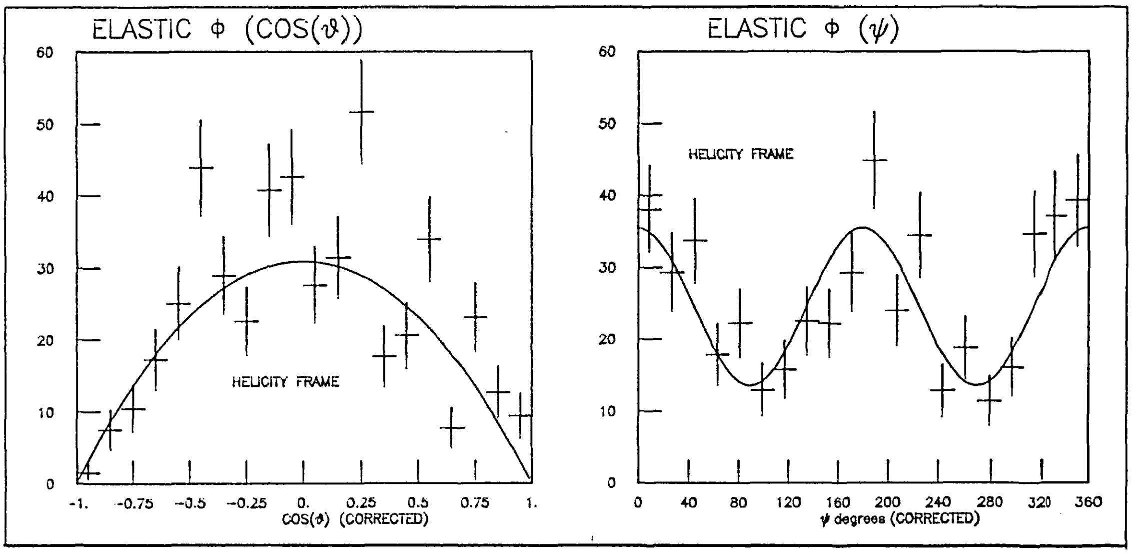

Figure 54: Angular Distributions in ϕ Helicity Frame

of $\rho_{00} = 0.003 \pm 0.031$, and $\rho_{1-1} = -0.069 \pm 0.034$ to the spin density matrix elements, indicating a value for the parity asymmetry parameter $P(\sigma)$ of only 0.17 ± 0.05. This is consistent with predominantly natural parity exchange in the t-channel and supports (though not conclusively) an SCHC production process. However, $\rho_{00} \simeq 0$ is in very good agreement with SCHC expectations.

In preparation for the study of inclusive ϕ photoproduction, figure 55 shows the Feynman-x distribution for the elastic ϕ events using the fitted beam energy, and clearly shows $x > 0.9$ with $0.9 < x < 0.95$. However, in the inclusive analysis the true beam energy is unknown and so the peak energy of 19.6 GeV is used. Therefore, figure 55 also shows the smearing effect on these events when Feynman-x is recalculated using the unfitted quantities and nominal beam energy, and indicates that elastic ϕs have a smeared $x > 0.7$.

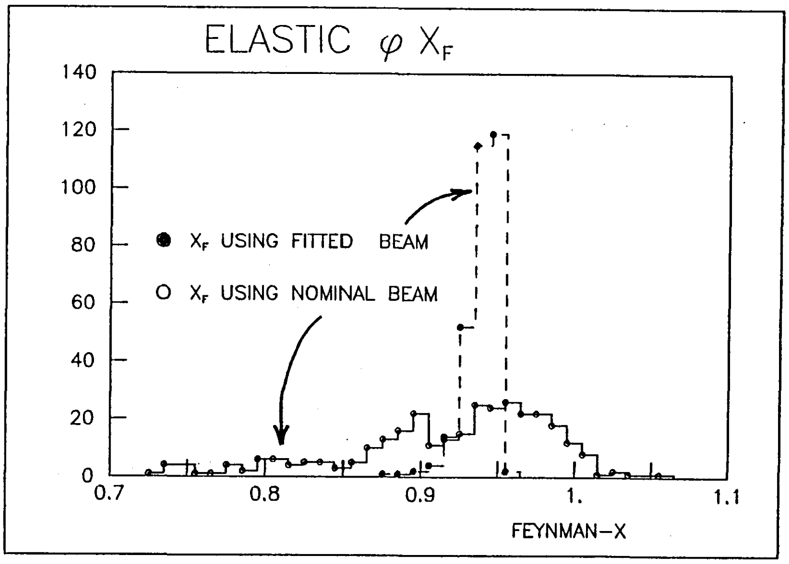

Figure 55: Smearing effect on fitted ϕ x distribution

6.2 INELASTIC ϕ PHOTOPRODUCTION

The inelastic ϕ signal was filtered using the Cerenkov counters by selecting events which contained one or more kaons. The kinematics of the events suggest the existence of 'central' production as well as 'peripheral' production.

6.2.1 Acceptance

An estimation of the acceptance for an inelastic ϕ signal presented a difficult problem, not least through the possibilities of various production mechanisms with, say, a topology dependence, but also the existence of neutrals. Therefore, it was decided to approximate any inelastic signal by choosing a peripheral phase space Monte Carlo method and generating $\gamma p \rightarrow p\phi\pi^+\pi^-\pi^0$ events according to n-particle phase space (using the CERN package FOWL [65]). The ϕ itself was generated from a gaussian distribution to simulate a distribution smeared by measurement errors†, and then allowed to decay to K^+K^- isotropically. This is reasonable since the elastic signal has already been shown to fit a gaussian, and also we may expect a 5 prong to dominate any inclusive signal. However, phase space is generally very far from describing real events, and therefore, events were generated as $\gamma p \rightarrow pX$ where $X \rightarrow \phi\pi^+\pi^-\pi^0$ and weighted as will be described. If events had been generated according to 5 particle phase space then the Monte Carlo would have been generating kinematically rare events, but though most of these

---

† This is possible since the ϕ is so narrow. The ideal method would have been to decay a ϕ (generated from a Breit-Wigner [63]), and then introduce track errors.

would have received a small weight a great deal of computer time would have been wasted.

The method used began by generating a value of t from a distribution of the form $\exp(-B|t'|)$ with B varied < 7.0. This value then defined a minimum and maximum value for the recoil mass m(X) as described by the Chew-Low Plot [66] which plots t versus $m^2(X)$. However, the "D-shaped" area defined by the boundary curve in the Chew-Low plot is not equally populated, and therefore, coupled with the other assumptions already used it was considered reasonable to generate $m^2(X)$ from a suitable ad hoc distribution bounded by the maximum and minimum values of $m^2(X)$: a) uniformly, b) from various gaussians and c) from a triangular distribution. Comparing the results indicated the Monte Carlo to be reasonably insensitive to the choice of function used.

It is worth noting that once t is generated in the lab this defines only the kinetic energy of the proton; and it is not until m(X) is generated that the cms scattering angle is known (the angle about the beam being completely free).

The recoil system X then decayed according to 4-particle phase space: $X \rightarrow \phi\pi^+\pi^-\pi^0$ and subsequently $\phi \rightarrow K^+K^-$ isotropically. Finally the whole event was assigned the 4 body phase space weight. Tracks were then swum through the SHF system in turn to test for event triggering. If an event 'triggered' then the kaons were tested for reaching the Cerenkov counters. Furthermore, background light and kaon identification efficiency were taken into account so that the calculated acceptance would include the probability of identification.

The final (averaged) results were constant over the ϕ mass range with: (20±3)% for detecting only one kaon, and (11±1)% both kaons.

6.2.2 Cross-Section calculation

The data sample was reduced by selecting all hybrid events passing vertex cuts with 3 or more charged tracks in the roll range 300-2531, and then applying (for convenience) the most loose kaon requirement. An event was selected if at least one hybrid track above 3.0 GeV/c gave no light in the Cerenkov counters or light in C1 above 10.6 GeV/c. This gave a data sample of 51176 events mainly through the second requirement.

These events were then analysed in groups depending on the number of kaons flagged per event. This was essential since the backgrounds in each sample would be different such that combining the samples may conspire to produce false peaks [67]. In the 3 prong sample 5357 events with 3C fits with $P(\chi^2) > 1\%$ were rejected to remove the elastic ϕ signal and at the same time remove $\gamma p \rightarrow \rho p$ events which could potentially introduce misidentified pions. Losses due to unmeasured tracks, which would affect the one-kaon sample only, were estimated to be (4.3±0.1)%. This gave a final sample of 29654 events with 1 kaon flagged, 3122 events with 2 kaons flagged, only 107 with 3 kaons and, only 1 event with 4 flagged†.

---

† These statistics illustrate effectively the impracticability of any search for glueballs here (currently very topical) despite the inherent difficulty of such a task, and also the strong theoretical arguments for/against any success [68].

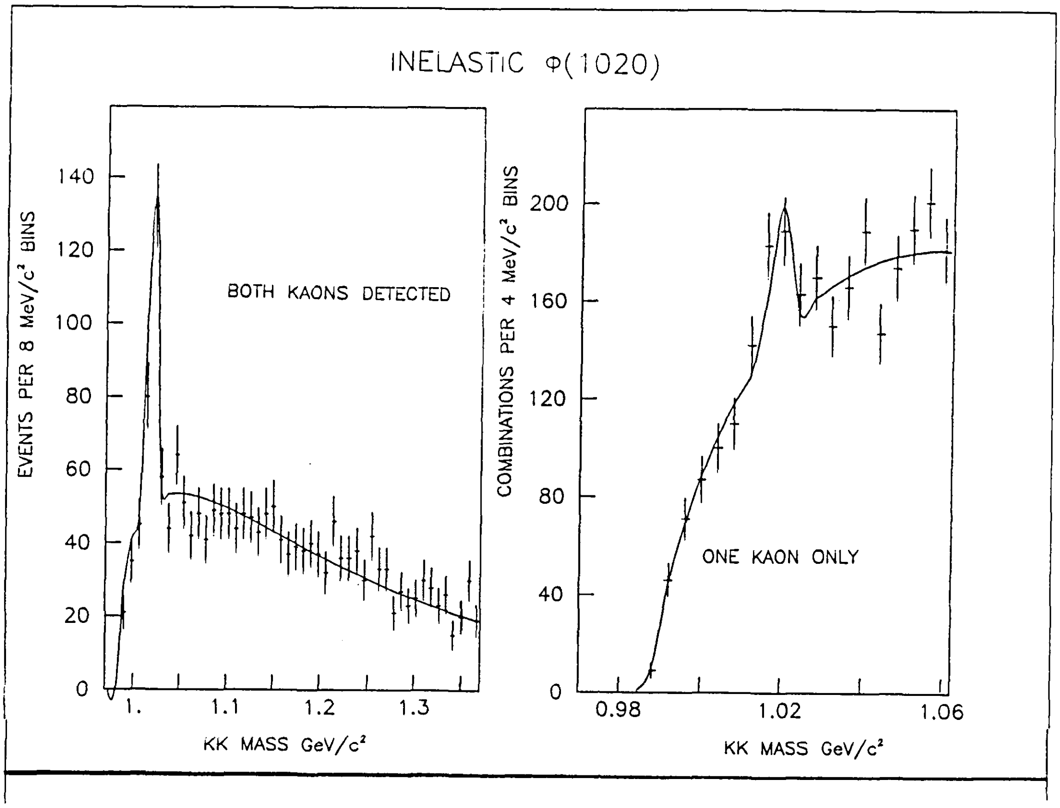

Figure 56: Inelastic ϕ mass plots

Figure 56 shows the m(K^+K^-) mass combination when two kaons were flagged and shows a clear signal. When only one kaon was identified it was combined with every other oppositely charged track. This is also shown in figure 56 and despite the large combinatorial background there is clear evidence of a ϕ peak. The signal to background can be improved upon as will be shown, but the effects of the cuts used on the acceptance are difficult to estimate, and therefore, it was decided to parameterise the background in the ϕ region before cuts to avoid this complication [69]. Subtracting the background gave estimates of the number of events: 117.0 ± 10.8 from 2 kaon events, 135.0 ± 11.6 from 1 kaon events, and a negligible number (<2) in the remaining small sample.

However, in this sample we can expect up to about a 10% elastic contamination in the 3 prong sample from pK^+K^- fitted events with fewer than 3 constraints. Pursuing this for events in the ϕ region the total momentum of the primary vertex charged tracks was plotted (one- and two-kaon samples separately). These showed a wide spread but with a peak (19÷20) GeV/c. Further, the $m(K^+K^-)$ plot indicated the ϕ peak to be predominantly from the total momentum range (15-22) GeV/c. Consequently, the planarity of these events was examined (elastic ϕs should have coplanar γ,ϕ,p), and indicated 8 and 10 elastic events to be leaking through into the one- and two-kaon inelastic samples respectively. Removing these and then correcting for losses gives totals of 1355.8 ± 146.7, 1973.1 ± 274.9 and 1568.4 ± 121.0 for the one-, two-kaon and combined samples respectively. Using the experimental sensitivity this corresponds to an inelastic cross-section of:

$$\sigma(\ \gamma p \rightarrow \phi X\ ) .BR(\ \phi \rightarrow K^+K^-\ ) = 360 \pm 52 \pm 61 \text{ nb} \quad \text{where } X \neq p$$

for the more reliable two kaon-sample and consequently:

$$\sigma(\ \gamma p \rightarrow \phi X\ ) = 731 \pm 105 \pm 130 \text{ nb where } X \neq p$$

Note that the cross-section calculated from the one-kaon sample yielded 502±57±160nb, with 581±50±110 nb from the combined sample. Other photoproduction measurements with which to compare are rare. The most recent Omega (WA57) reports cross-sections of: 1499±74±150 nb and also 907±37±90 nb [62.9], whereas the previous Omega (WA4) found 621±33±190 nb. This is compared to the results of Behrend et al [62.6], who measured the inelastic to elastic cross-section ratio using $d\sigma/dt$ at t(min) as a function of photon energy and obtained $\sim$ 0.38±0.15 for $4.6 < E(\gamma) < 6.6$ GeV.

6.2.3 Inelastic ϕ Production Characteristics

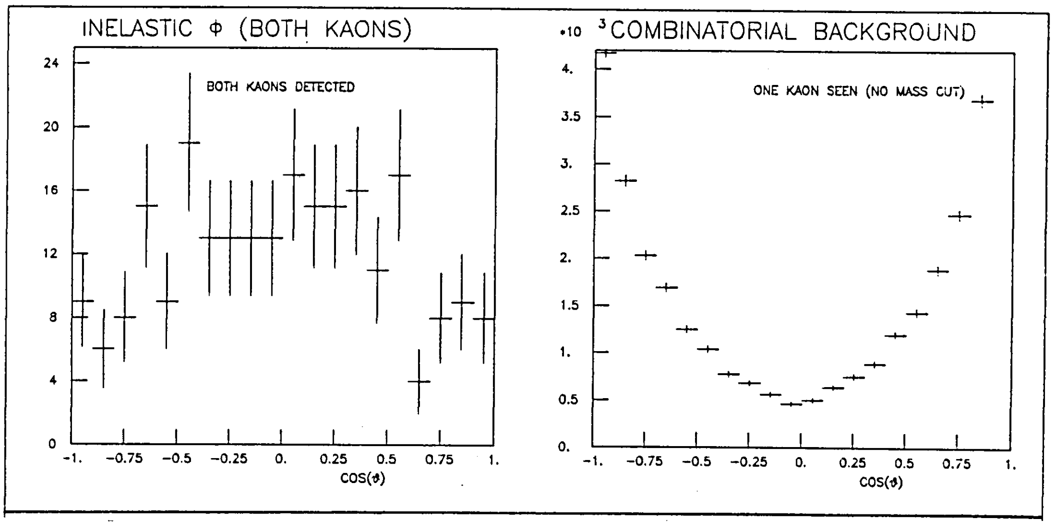

Figure 57: Decay angle in one- and two-kaon samples

The background in the one-kaon sample was first reduced by combining the kaon with all tracks except those flagged as pions, which had a negligible effect on the signal. Secondly a cut was made on the cosine of the decay angle, plotted in figure 57 for the combinations with one- and two-kaon tracks per event. The two-kaon plot, shown for events in the ϕ region, is consistent with a $\sin^2\theta$ dependence. On the other hand the one-kaon plot shows large 'wings' which most likely are from background combinations, and therefore, a cut was made to remove these wings at $\cos\theta = \pm 0.7$. Without any prior knowledge of the production distribution it could be a mixture of for instance, a $\sin^2\theta$, flat (isotropic), and $\cos^2\theta$ distributions, and therefore, the above cut would have very different effects on the acceptance.

The mass plots are shown in figure 58 as a function of topology and clearly there is evidence for an inelastic signal in all topologies despite the combinatorial background.

It is possible to conceive of three general production mechanisms for an inclusive ϕ shown pictorially in figure 59.

a) Diffractive with target break up. This would go via pomeron exchange resulting in target products and a reasonably energetic ϕ.

b) Quark Fusion. This can be subdivided according to quark mass: light quark fusion in which the ϕ 'carries' all the strangeness, and strange quark fusion, in which extra strange particles are produced.

c) Finally, γ-g, g-g fusion. These will be the rarest mechanisms if they exist at all. Gluon-gluon fusion can probably be ignored but photon-gluon fusion is a favoured mechanism for the understanding of charmed particle photoproduction in our experiment.

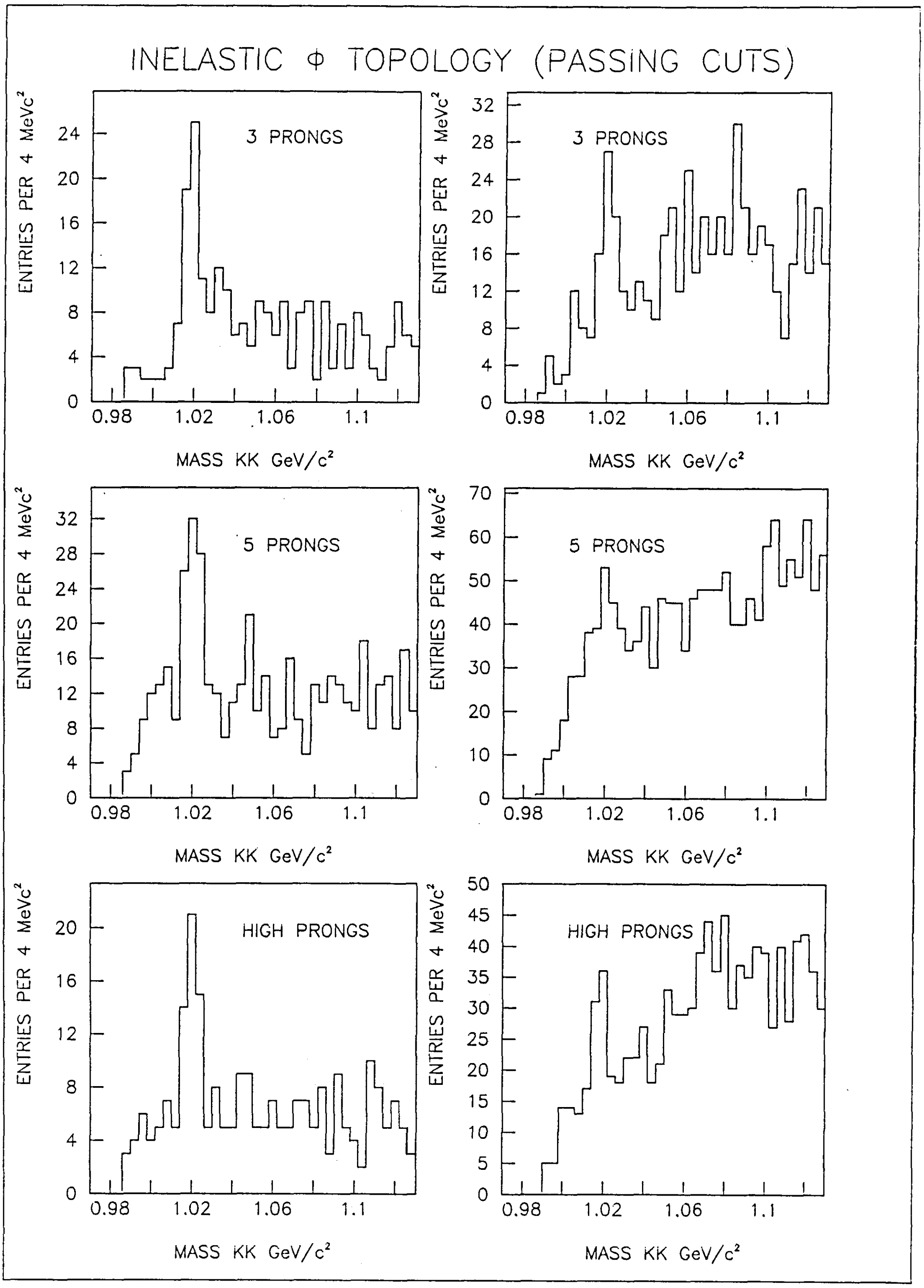

Figure 58: Topology of Inelastic ϕ events
Two-kaon sample (left), one-kaon sample (right).

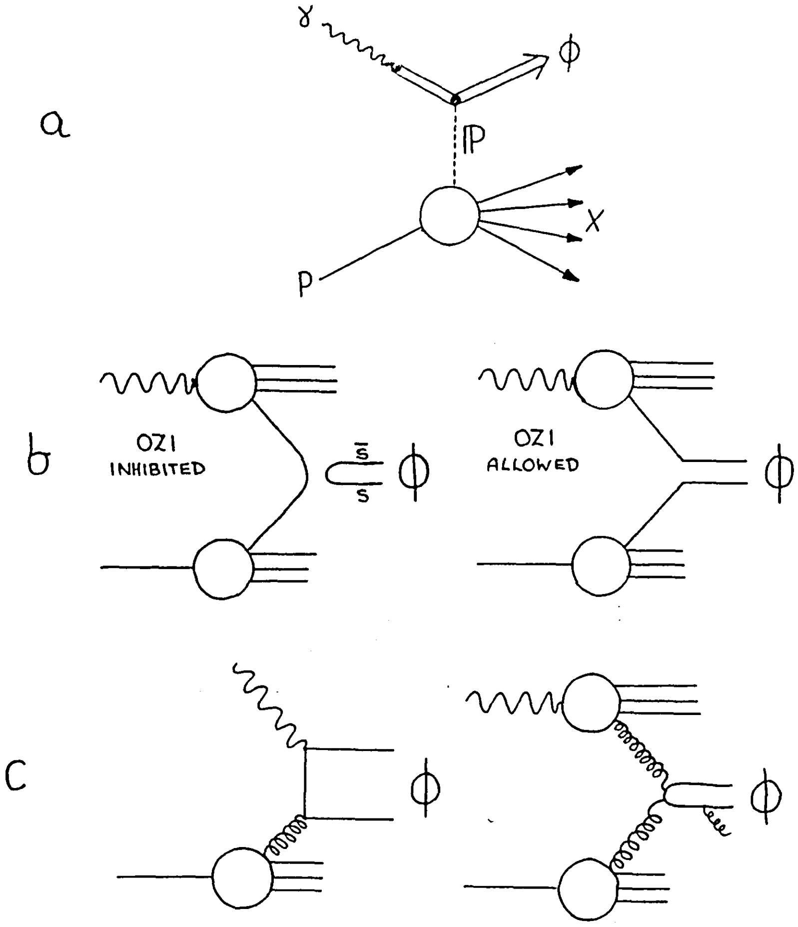

Figure 59: Possible Inelastic ϕ Production Mechanisms

Unless extra strangeness is observed it is difficult to distinguish between any of these production mechanisms. However, an intuitive approach can be employed by examining the Feynman-x distributions. Figure 60 shows the x distribution for all two-kaon combinations in the ϕ region and ranges $\sim 0.3 < x < 0.95$. Elastic ϕ events were shown to have $x > 0.7$ and therefore if the sample is split at $x = 0.7$ and replotted there is clearly still a signal with low x. Tentatively this can be associated with some form of central production with possibly the diffractive mechanism representing the higher x events. The same plots are calculated using the one-kaon events. The x distribution is surprisingly flat[†] in the range $0.5 < x < 1.0$ but then rises sharply as $x \to 0.25$. It is reasonable to assume that this peak represents the majority of the combinatorial background. Despite this, when replotting the mass plot divided at $x = 0.7$, there is still a definite signal in the low x plot.

Furthermore, figure 61 shows the m(KK) mass spectrum when all unassociated beam conversions have been removed and clearly there is some evidence for ϕ production with an associated strange V^0. The two-kaon events show an insignificant ϕ signal, but there is better evidence for a ϕ signal in the one-kaon sample all of which had a ϕ with $x < 0.7$. This is arguably evidence for central production proceeding via strange quark fusion. The main cuts used to remove beam conversions were on the V^0 Pt w.r.t beam direction (x-axis) and the $m(e^+e^-)$; the remaining V^0s were checked for K^0s and Λs.

Since SCHC has been demonstrated to be at least consistent with elastic ϕ photoproduction then it is a reasonable hypothesis for a diffractive inelastic process. Figure 62 shows the $\cos(\theta)$ distribution in the Helicity frame for different x regions. The distributions do not indicate any clear behaviour in the $x > 0.7$ sample (because of statistics), but the low x sample shows a $\sin^2\theta$ behaviour, (consistent with but not proof of a diffractive

---

[†] The Omega collaboration observe a distinct rise at $x > 0.8$ which they associate with a diffractive mechanism with target breakup [62.9].

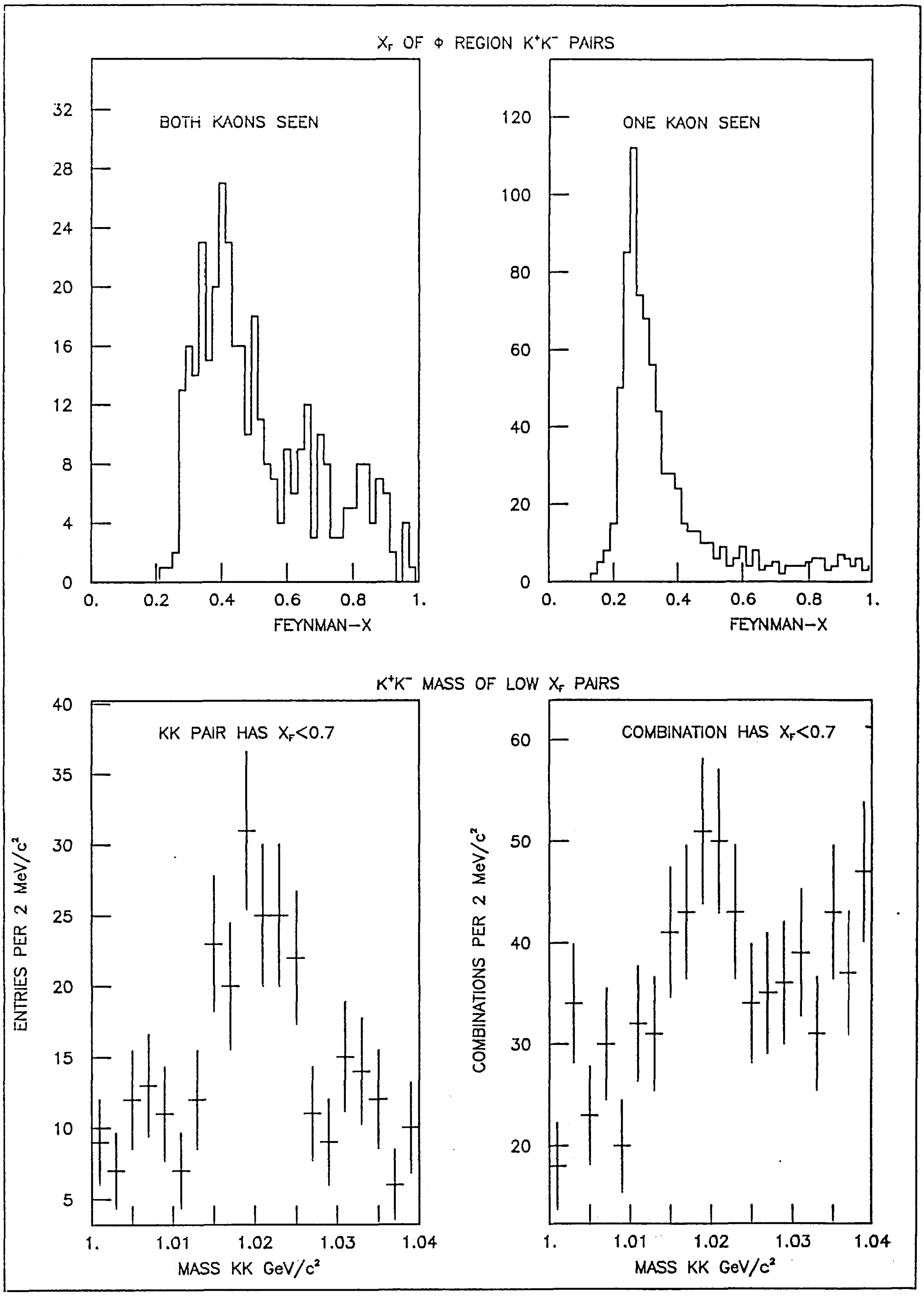

Figure 60: Inelastic signal in different x regions
The data has been divided into two subsets by splitting the mass combinations at x = 0.7.

mechanism). The plots from one-kaon events show the opposite to SCHC expectations resulting from the combinatorial background which makes their interpretational value limited. The general behaviour of these plots do not alter if the 3 prong sample is removed (not shown).

In conclusion, it has been difficult to isolate any particular production mechanism for the inelastic ϕ. However, assuming that the smeared x distribution for the (fitted) elastic ϕ signal is a good indicator of the effects of beam spread, then it has been demonstrated that there is evidence for central as well as peripheral inelastic ϕ production. It is extremely interesting to note that the OMEGA collaboration (a γp experiment with 25 GeV $<$ E(γ) $<$ 80 GeV, and high statistics) observed a definite change in their angular distributions (above and below $x = 0.7$), which has been interpreted as evidence for two production mechanisms. In particular they demonstrated that a quark fusion model could reproduce their results at low x. It seems likely that a similar mechanism ought to be invoked in our experiment since it is at a neighbouring energy.

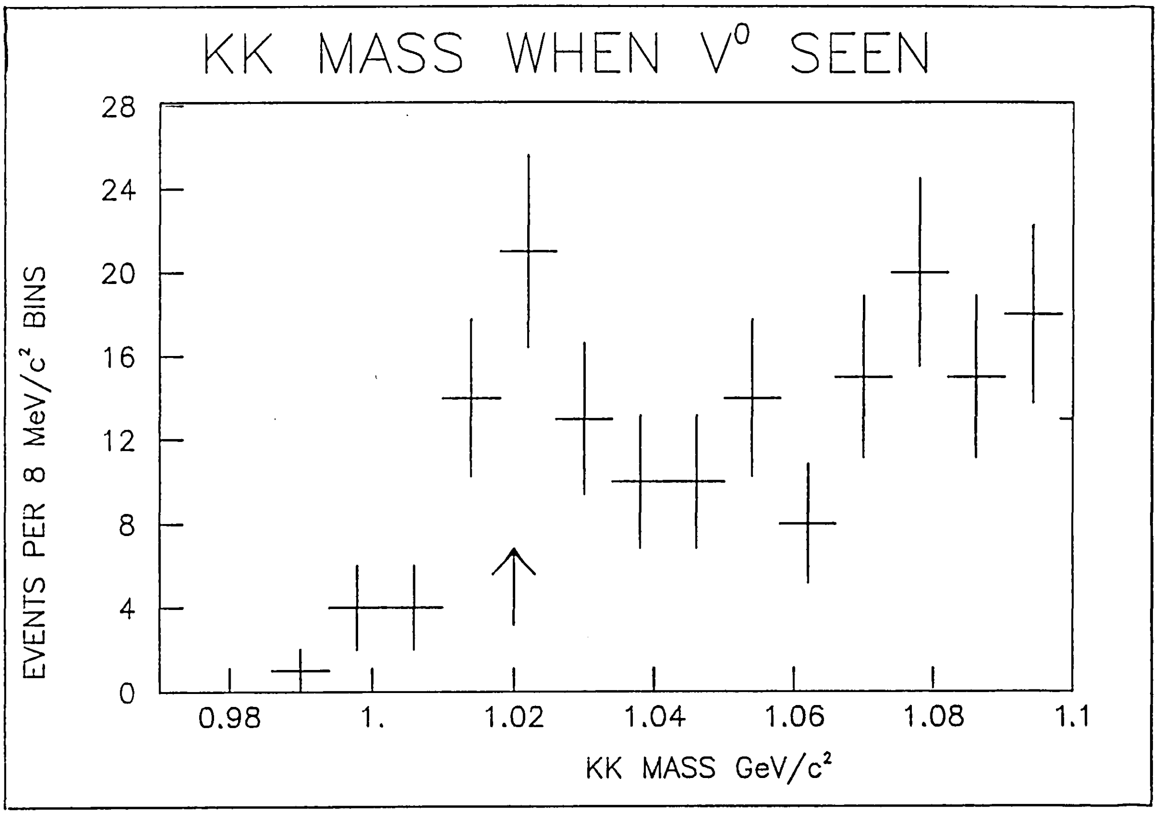

Figure 61: m(K^+K^-) when strange V^0 seen

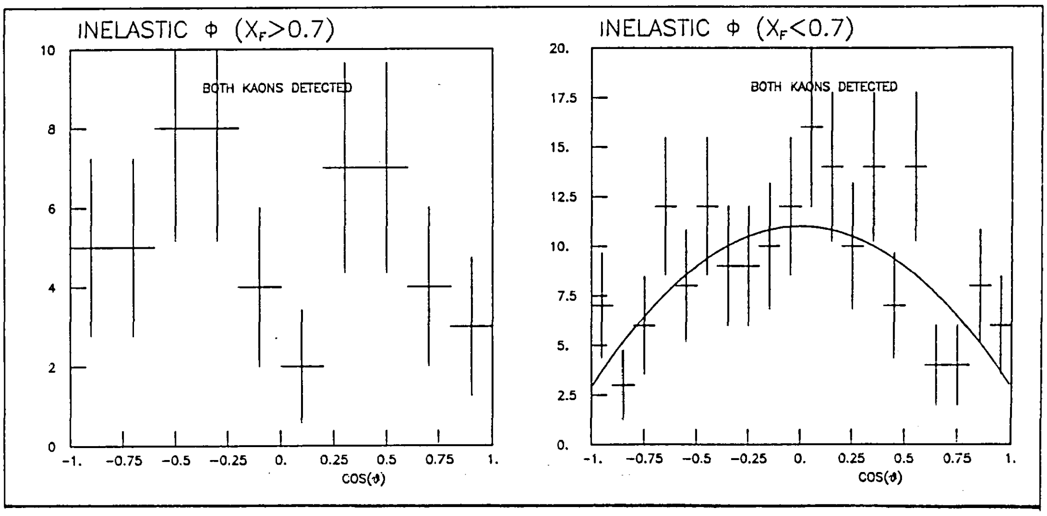

Figure 62: Angular Distributions in Helicity Frame (as f(x))

6.2.4 Any evidence for F Photoproduction?

Charmed F photoproduction has been reported by several experiments [70] with a reported mass of ~ 2020 MeV/c^2. Recently however, a result obtained by the CLEO group at Cornell (an e^+e^- experiment) of 1970 ± 5 MeV/c^2 has generated much interest. This signal was seen as an enhancement only in the channel $\phi\pi^+$, $\phi\pi^-$ and subsequently confirmed by the ARGUS and TASSO collaborations at DESY [71], whereas the ACCMOR collaboration claim a signal in $KK\pi$.

The results of our collaboration are quoted in figure 63, calculated using the charm candidate events and show no F signal. The current value of the lifetime is believed to be ~ 1.9×10^{-13}s [1], however all experiments have difficulties observing very short lifetimes, and therefore, it is possible that the lifetime may be shorter. With this consideration in mind the K^+K^- pairs from the inclusive sample with 5 or more charged primary tracks were combined with all other charged tracks, and plotted separately for $m(K^+K^-)$ in and outside the ϕ region. The distributions have a phase space shape peaking at ~ 1280 MeV/c^2 and falling off sharply, and show no evidence of an F signal; the same plots made using the $KK\pi$ combinations (ie, not ϕ) show a similar behaviour and no F signal (figure 64).

However, although not statistically significant it is nonetheless interesting to attempt an order of magnitude calculation on a cross-section limit. First, the mass plot was replotted with each entry weighted by the number of entries contributed by the event. Any genuine signal must be at least smaller than the fluctuation in the background. Then, assuming that the detection efficiency for D-decays to 3 charged tracks (~15±10)% [10.10], is a reasonable guide, together with detecting two kaons from inelastic ϕ (10±1%), would suggest an F acceptance of the order of 10%. Hence:

$$\sigma(\gamma p \rightarrow FX).BR(F \rightarrow K^+K^-\pi) < 19\text{nb (where } \pi \neq \pi^0)$$

This <u>crude</u> calculation is compared to an Omega result at 60 GeV [71.5] which assumes F^+F^- pair production giving $\sigma.B(F \rightarrow \phi\pi) < 4$ nb.

As a final comment on the enhancement reported in $\phi\pi$(1970), it is interesting to note that Close and Lipkin (by consideration of the OZI rule) postulated that a $\phi\pi$ signal would be a possible signature for exotic states of a four quark nature [72].

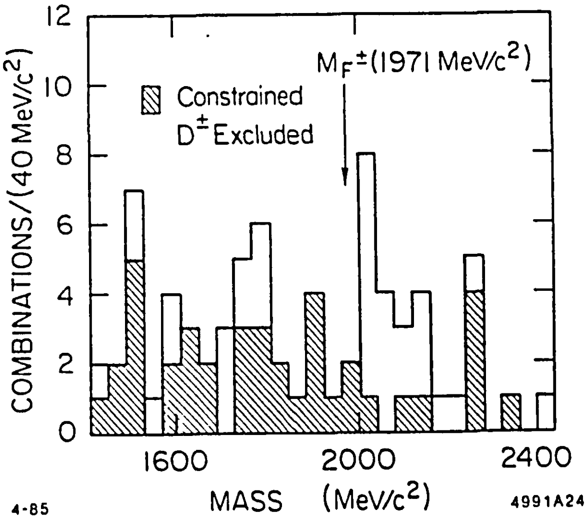

Figure 63: BC73/75 collaboration F Search
This plot is quoted from our collaboration results [10.11], and shows charged decays pointing back to the primary vertex (interpreted as an F). The apparent enhancement at 2040 MeV/c² is a reflection of D-decays when a pion is given a kaon mass.

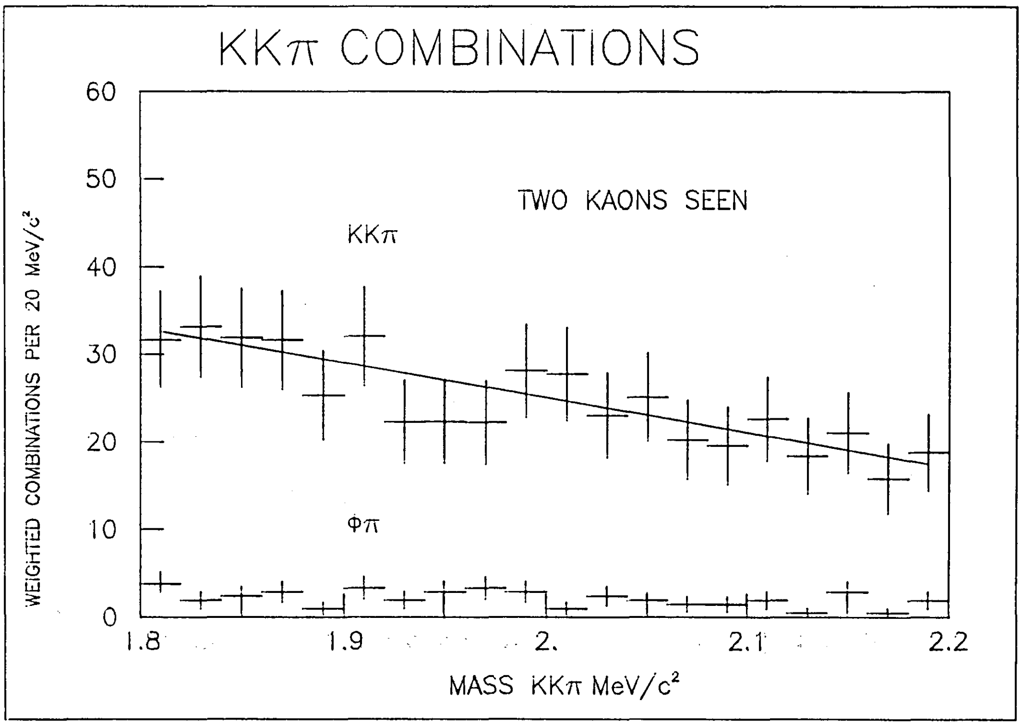

Figure 64: Combinatorial KKπ mass in F mass region
No evidence of an F signal.

Chapter VII

SINGLE PARTICLE INCLUSIVE DISTRIBUTIONS

This chapter reports on charged pion and kaon inclusive distributions in the forward region. A charge asymmetry has been observed for which we have constructed a simple model. Also charged particle ratios are reported. Finally, the forward region is examined for any evidence of a "jetlike" appearance as seen by the comparable γp experiment OMEGA(WA57).

7.1 EFFECTS OF BEAM SPREAD/MISIDENTIFICATION

Inclusive distributions are frequently presented using Feynman-x (and sometimes cms rapidity). This requires a knowledge of the cms energy, but in our experiment the interacting photon four-momentum is unknown. However, the beam direction and energy spectrum are well known, with the latter showing a narrow peak so that it is not unreasonable to use a nominal beam energy of 19.6 GeV. However, this has the effect of shifting a true x value to some apparent value and hence introduce bias into the x distribution. These 'beam spread effects' have already been investigated for pions [18.2] with the results shown in figure 65. The effects for kaons has also now been calculated from the 3C fits and is also shown on the figure.

A second source of bias arises through track misidentification. However, as figure 66 shows, the shift in x due to π/K/p misidentification in the beam fragmentation region is negligible (the x was calculated for each mass (π/K/p). At 4 GeV/c the π/K x difference is only 0.03 falling to less than 0.01 above 8 GeV/c.

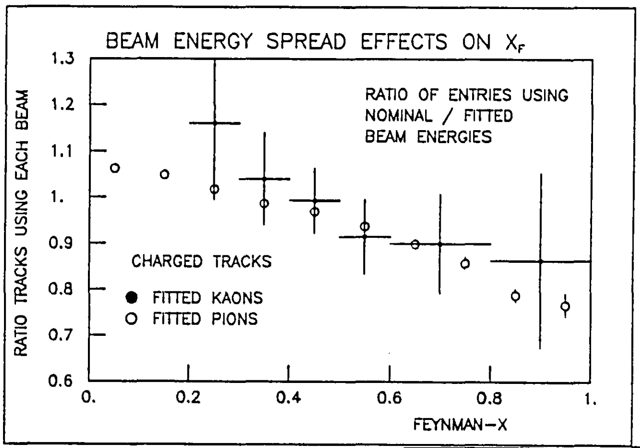

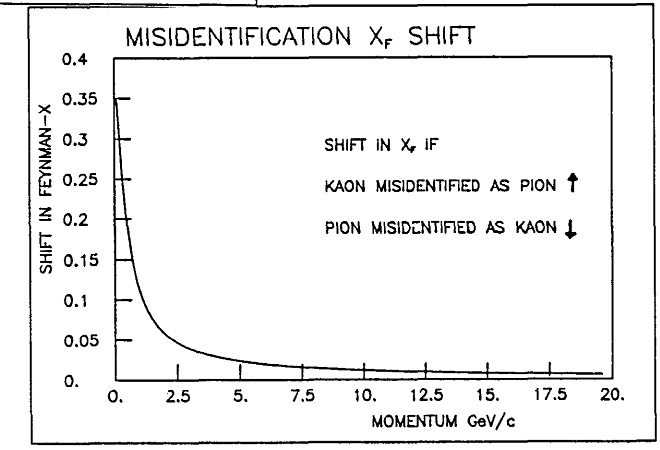

Figure 65: Beam Spread Effects for Pions and Kaons
Correction factors to be applied to pion and kaon x distributions to counter beam spread effects.

Figure 66: Misidentification Effect on Feynman-x

7.2 INCLUSIVE CHARGED (PION) DISTRIBUTIONS

A subgroup within our collaboration has studied the forward going charge in our beam fragmentation region. A net positive excess has been observed which increases with Feynman-x and transverse momentum. We believe this behaviour suggests that target fragments going forward are not responsible. A simple model had been developed which uses recombination ideas (discussed in chapter 5), but extended to include the interaction process, which qualitatively explains our results†.

7.2.1 Observation of a Forward Charge Asymmetry

The positive charge asymmetry was observed by studying the average charge $\langle Q\rangle$ defined as: $\langle Q\rangle = (N^+ - N^-) / (N^+ + N^-)$ where N^+,N^- are the number of positive and negative tracks in any given kinematic interval. This is plotted in figure 67 as a function of laboratory momentum which is <u>independent</u> of particle identification. The strongly positive target region (ie, proton) is obvious and decreases rapidly at low momenta to a plateau of $\langle Q\rangle \sim +0.1$, which remains uniform and extends to the limit of the range.

Assuming the nominal beam energy, figure 68 shows the average charge as a function of x (where all particles have been assumed pions). Although, in the forward region this includes ~8% of tracks which are kaons (with a negligible proton contamination), the π/K mass difference has a negligible effect on the x

---

† A publication is currently in preparation [10.13]; also presented at the April 1985 Washington APS meeting [73].

distribution for x > 0.1. Clearly there is a distinct change in the average charge with increasing x and transverse momentum. At low Pt the average charge is consistent with zero, whereas as Pt increases the average charge becomes increasingly positive, being most strongly associated with high x and high transverse momentum. Figure 68 also shows the ratio N^+/N^- which although demonstrates the asymmetry more strongly, is less straightforward to interpret.

These results are in direct conflict with a basic assumption of the models of low momentum transfer which would require the forward going charge (x>0.4) to average zero for a photon beam.

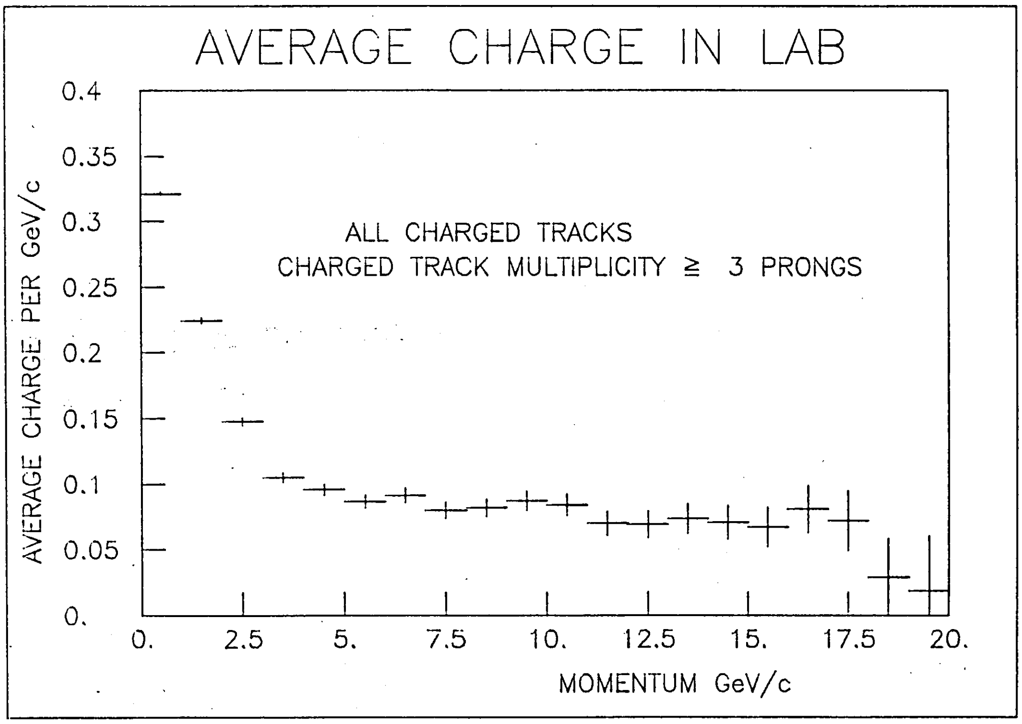

Figure 67: Average charge as a function of lab momentum

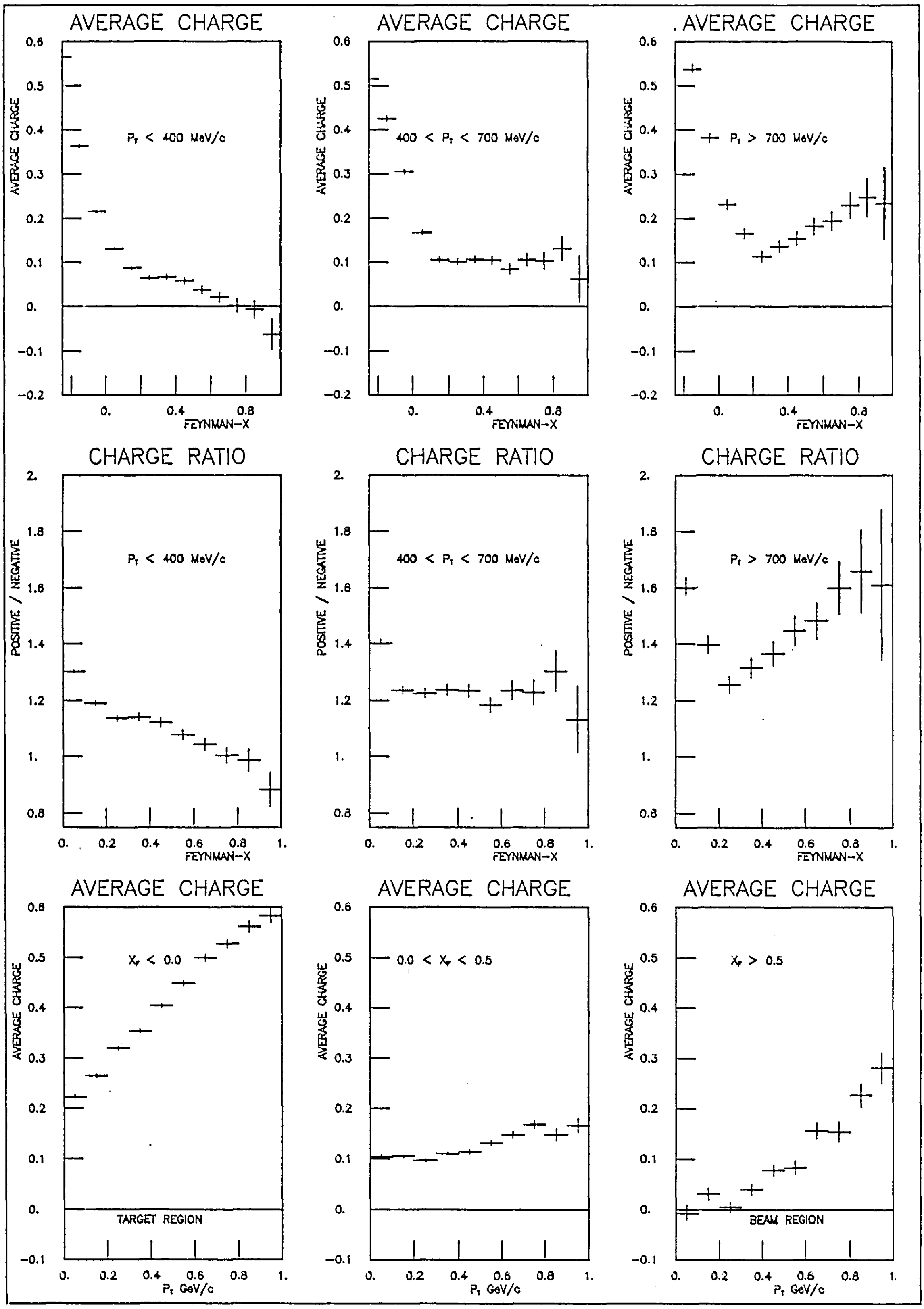

Figure 68: Forward Charge Asymmetry
The net positive charge increases with Feynman-x and transverse momentum, whereas naively, a zero forward average charge would be expected for (x>0.4).

7.2.2 Search for Experimental Bias

A check has been made for possible biases towards positive tracks in our trigger, scanning, measuring or reconstruction procedures sufficient to account both for our observed charge imbalance and its behaviour. Also independent sets of programs were written as an internal consistency check on the analysis within our group.

Trigger Bias?

Recall that our experiment has two independent triggers OR-ed together. Therefore, the average charge was replotted selecting those events with a PWC trigger (73% of the data) irrespective of a Pb-glass trigger (figure 69), and also vice-versa (84% of the data). About 58% of events were triggered by both triggers. No difference is seen in these two subsets. Furthermore, similar results hold when selecting on a single trigger (15% PWC only, 27% Pb-glass only). The conclusion is that there is no evidence for any trigger bias.

Measuring/Hybridisation?

This is difficult to investigate since at the DST stage we can only confirm that tracks are internally consistent. If in any given kinematic interval the number of positive tracks is different to the number of negative tracks, then since the probability that any particular track will hybridise is independent of charge (+-), they should hybridise in the same proportions. Therefore, to first order, the fraction of positives hybridising should be the same as negatives. This is plotted in figure 70 and is clearly consistent with unity everywhere except at low momenta. This fall is interpreted as a loss of short tracks such as stopping protons.

Therefore, it is concluded that there is no evidence of any experimental bias which could result in our observed charge asymmetry.

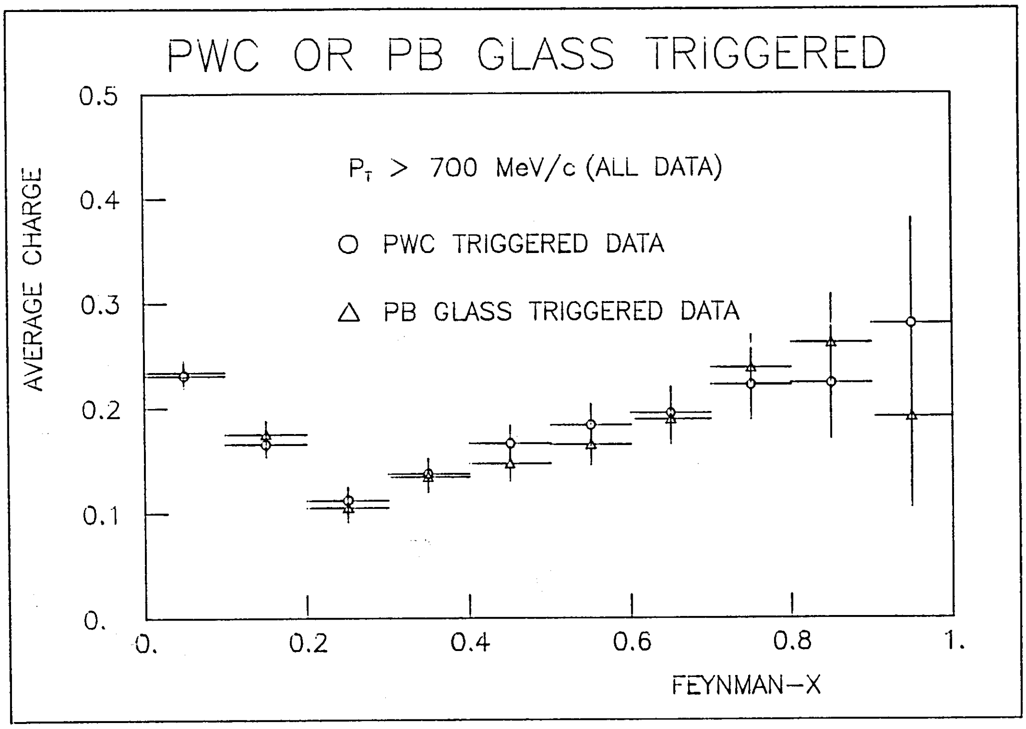

Figure 69: Average Charge using Each Trigger

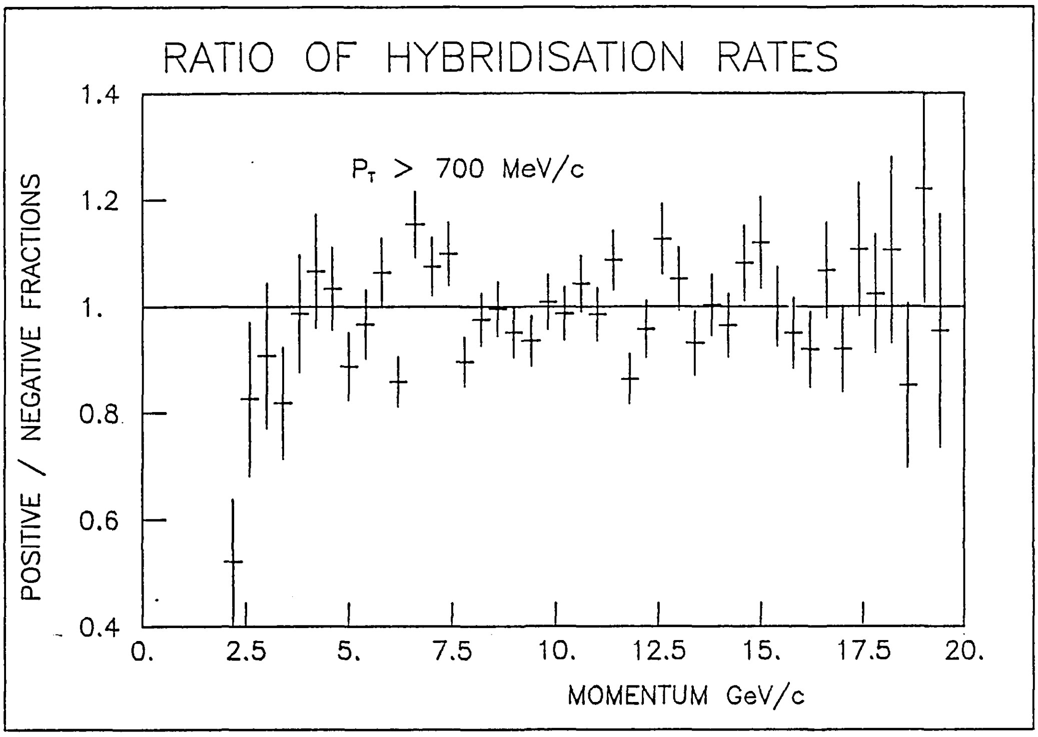

Figure 70: Positive/Negative Hybridisation Ratio

7.2.3 Resonance or Strangeness effects?

Without any experimental bias present it is still possible that some common physical process causes the charge asymmetry [74].

Diffractive Interference?

The quasi-elastic process $\gamma p \rightarrow \pi^+\pi^-p$ involving $\rho^0(770)$ production is well understood in terms of the Söding Model [75]. This model includes the effects of (Drell) 'direct pions' which may be considered as a potential source of our asymmetry.

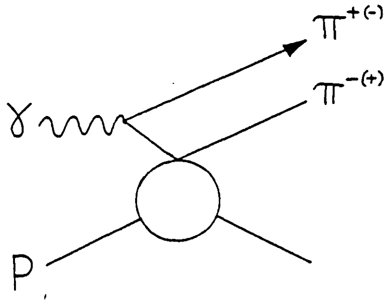

A Monte Carlo calculation based on this model (written and performed by SLAC [75]) predicted that diffractive ρs would decay symmetrically with an average charge of zero over the entire range. Using the 3C fits to $\gamma p \rightarrow \pi^+\pi^- p$ the $\rho^0(770)$ was selected by mass ($690 < m(\rho) < 850$ GeV) and plotted in figure 71. Clearly the data are consistent with zero.

Asymmetry due to Strangeness?

Since we expect ~8% of charge tracks in the forward region to be kaons, then there is a serious possibility that processes involving strange particles could be responsible. In particular, there is within the kaon sample a natural K^+/K^- asymmetry due to the associated production of K^+ (eg: $K^+\Lambda$) being enhanced by a factor of ~30 relative to K^- production. The fraction of events containing a Λ has already been measured in this experiment to be ~5% [76]. If this were the explanation, then what role would the hyperon play? To examine this, figure 72 shows the average charge for all those events with a visible sign that strangeness could be present (ie, kink/V^0), where V^0 events were first checked to remove beam conversions. These events contain, in theory, an enriched sample of kaons and hyperons (Λ,Σ) but the charge asymmetry is not significantly increased. The size of the increase is insufficient to account for the effect in the full sample and removing these events does not appreciably change the asymmetry, and therefore, it is concluded that a further mechanism must exist.

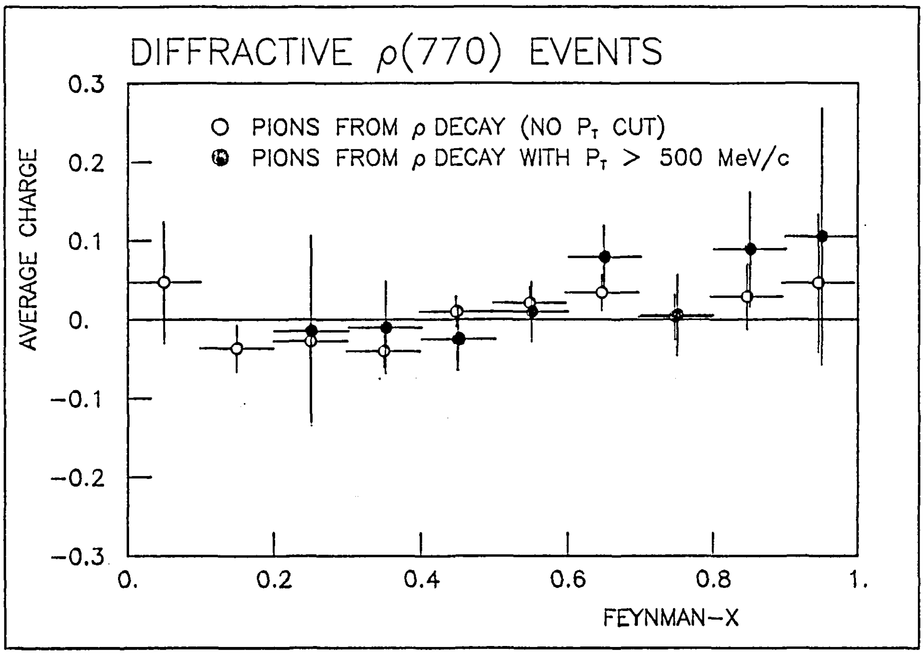

Figure 71: Symmetric Average Charge from Diffractive Processes

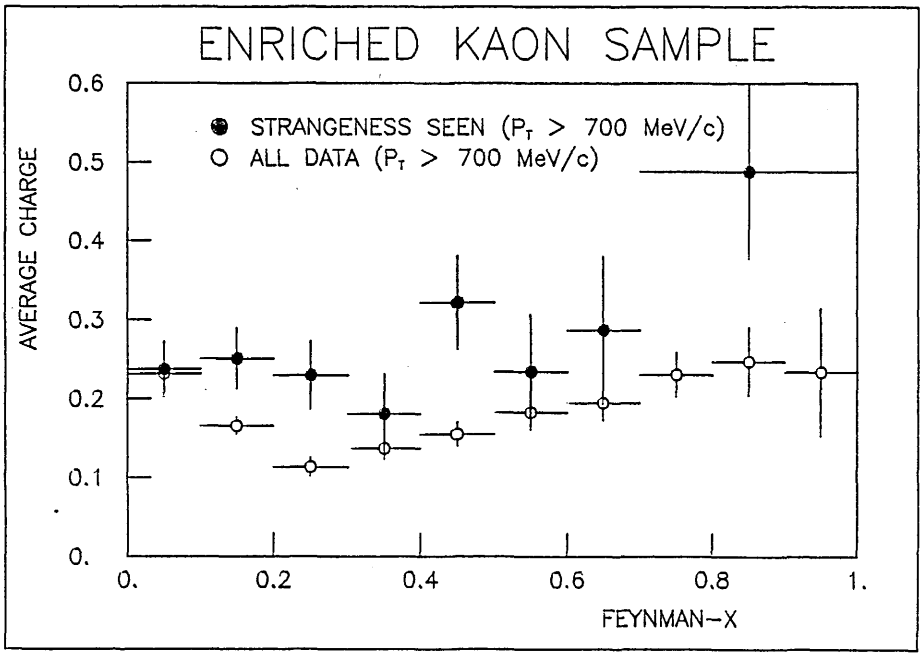

Figure 72: Forward Average Charge with Enriched Kaon Content

7.2.4 Interpretation and Proposed Mechanism

The understanding of our forward charge asymmetry is based upon an extension of recombination concepts by including the effects of the interaction process. This approach was also used by Buschbeck et al, whose results have already been discussed in chapter 5 [61]. They had considerable success in explaining the behaviour of their target fragmentation from an enhancement of like-flavoured quark-antiquark annihilation. In particular, the scattering of all quarks could occur through the t-channel exchange of a gluon, but like-flavoured quark antiquark scattering could have the additional option of the annihilation channel:

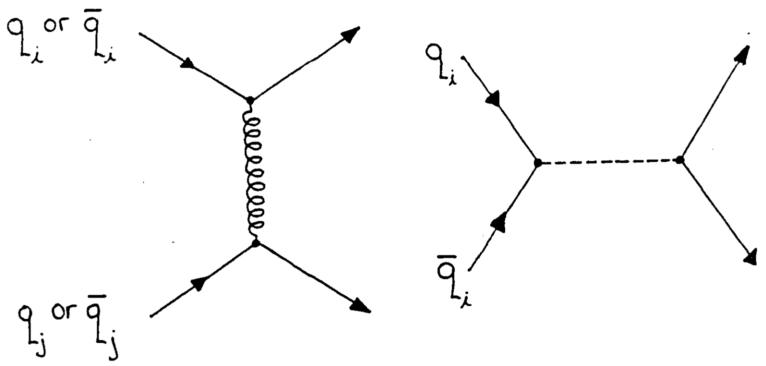

We believe that this annihilation mechanism is sufficient to account for our observed charge imbalance. To support this, consider that this annihilation mechanism can, to first order, be called upon to explain qualitatively the fact that the $\sigma(p\bar{p})$ cross-section exceeds that of $\sigma(pp)$ up to $\sqrt{s} \sim 100$ GeV. This upper limit corresponds to quark-quark or quark-antiquark cms energies of $\sqrt{s} \sim 3$ GeV, and therefore, since in our experiment our total cms energy is only $\sim$ 6.2 GeV the cms energy of any of our interacting partons would be within the region of the annihilation enhancement. We consider this then as the major component in the asymmetric forward charge mechanism.

The basis of our model is that after the photon has dissociated into a 'quasi-free' quark-antiquark pair, the antiquark will tend to scatter more frequently than the quark because of the annihilation channel open to it, and so leave the (spectator) quark to continue forwards to hadronize into the observed hadrons. The hadronized spectator system will on average be positive. This is because the probability that the spectator is a u-quark is larger than for a d-quark for the following reasons:

a) the photon coupling to $u\bar{u}$ is enhanced by a factor of four in intensity relative to the $d\bar{d}$ coupling, and

b) the coupling is further increased by a factor of two from the two u valence quarks in the proton (uud), either of which can annihilate.

Any interactions with the sea can only contribute a charge symmetric background, and therefore, it follows quite naturally that we should expect to observe (on average) more positive charge going forward than negative. In principal, target u quark interactions with the photon sea could also add to the asymmetry. Any charged resonance production (eg, ρ^+,ρ^-), should reflect a similar asymmetry, and so only contribute to a smearing on the resultant x distribution. Our model is illustrated in figure 73.

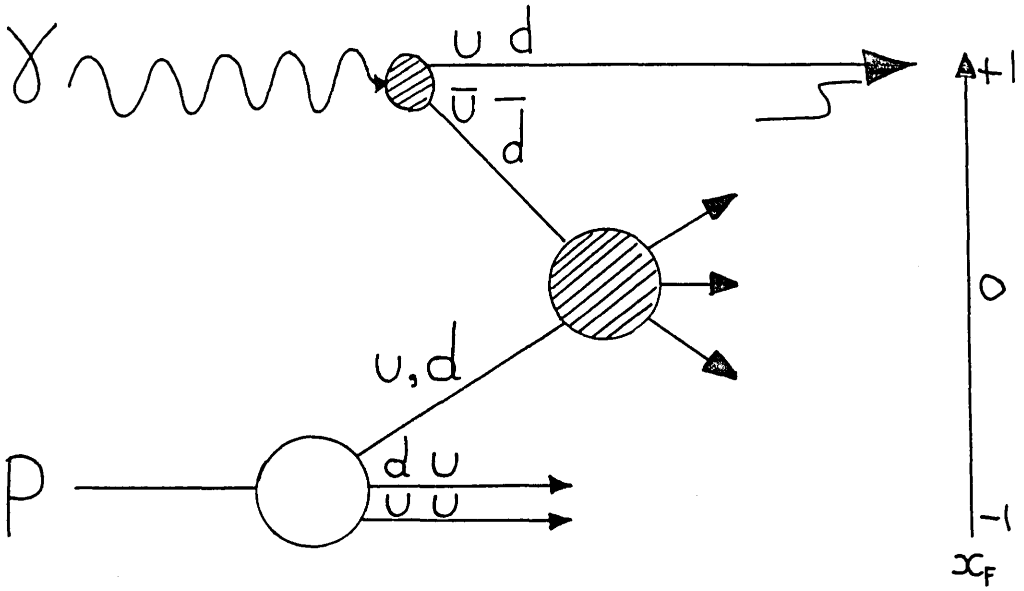

Figure 73: Proposed Charge Asymmetry Interaction Process

Various experiments have also observed similar charge asymmetric effects, with the EMC collaboration a good example (a muon-proton experiment at 280 GeV/c [77]). They report net charge as a function of cms rapidity and observe a clean separation between current and target fragmentation by a 'dip' around zero rapidity, with a rise on either side to net positive charge. Their results are consistent with a pointlike photon interacting directly with proton constituents, with a probability proportional to the charge squared of the struck quark. These authors interpret their net forward charge as due to the approximate preservation of the charge of the struck quark impelled forward. Using the ideas so far presented the development of our model will now be discussed.

7.2.5 Development of an Extended Recombination Model

Our Monte Carlo was constructed from a series of assumptions as a feasibility check on the interpretation of our forward charge asymmetry [78]. Despite its naivity, its aim was to establish (at best) plausibility for our interpretation rather than reproduce the data, but considering its simplicity the results are surprisingly good. Referring to figure 74, our mechanism is briefly as follows: we consider the photon to dissociate into a quasi-free quark-antiquark pair, which through the interaction leaves a fast forward spectator quark. This is predominantly positive (due to the photon coupling and the proton uud quark content), and recombines at approximately the same x to form the observed hadrons.

We assume that the interacting parton from the beam is a quark or antiquark (only) with Feynman-x (x_1), which leaves the rest of the photon to continue forwards with x ($1-x_1$) and recombine into the observed hadron(s). The coupling of the photon to the quark-antiquark pair is proportional to the quark charge squared so that the relative strengths of the photon manifesting as a $u\bar{u}$: $d\bar{d}$ pair is in the proportion $P(u\bar{u}) : P(d\bar{d}) \equiv \frac{4}{9} : \frac{1}{9}$. We insist that the interacting parton will be predominantly the 'slower' parton (lowest x), leaving the faster parton to behave as the spectator, where the quark and antiquark have equal probabilities of being slower.

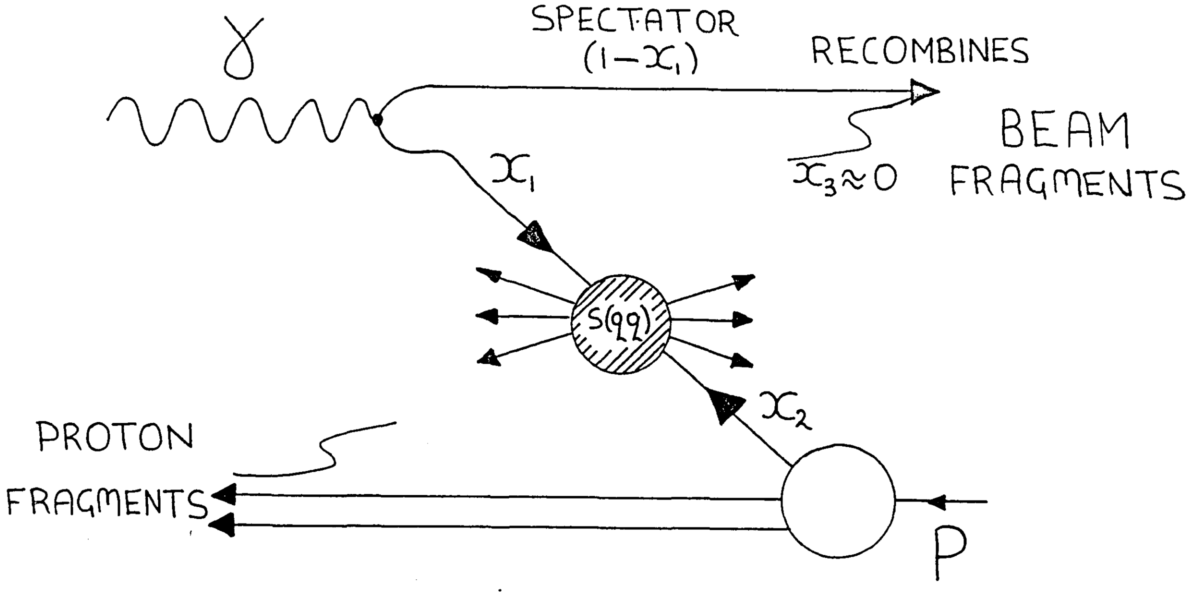

Figure 74: Charge Asymmetry Mechanism in our Model

Thus:

$$P(\text{slower } u \text{ or } \bar{u}) = P(u\bar{u}) \times \tfrac{1}{2}$$

$$P(\text{slower } d \text{ or } \bar{d}) = P(d\bar{d}) \times \tfrac{1}{2}$$

Next we must consider the interaction of the slower beam parton with the target proton (uud), where the 4:1 'u-quark dominance' is now further increased by a factor of 2 to 8:1 for u. We simply consider which interactions leave a positive, and which a negative, spectator at $(1-x_1)$. Then, based on similar ideas found in the Additive Quark Model [48], we sum the individual cross-sections for scattering subprocesses for <u>LIKE</u> and <u>UNLIKE</u> quarks. Therefore, ignoring sea and gluon effects:

a) <u>Positive spectator at (1-x_1)</u>

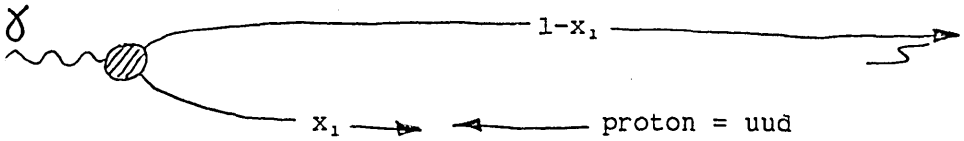

$$\begin{array}{rcl}
u \rightarrow \sigma(q\bar{q}) & \qquad & u \rightarrow \sigma(qq) \\
\bar{u} - u \rightarrow \sigma(q\bar{q}) & & d - u \rightarrow \sigma(qq) \\
d \rightarrow \sigma(qq) & & d \rightarrow \sigma(qq) \\
\hline
2\sigma(q\bar{q}) + \sigma(qq) & & 3\sigma(qq)
\end{array}$$

where $\sigma(q\bar{q})$,$\sigma(qq)$ are the total cross-sections for the scattering of LIKE and UNLIKE flavoured quarks. Similarly:

b) <u>Negative spectator at (1-x_1)</u>

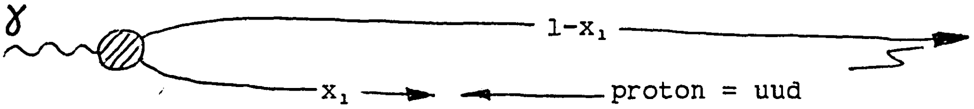

$$\begin{array}{rcl}
u \rightarrow \sigma(qq) & \qquad & u \rightarrow \sigma(qq) \\
u - u \rightarrow \sigma(qq) & & \bar{d} - u \rightarrow \sigma(qq) \\
d \rightarrow \sigma(qq) & & d \rightarrow \sigma(q\bar{q}) \\
\hline
3\sigma(qq) & & \sigma(q\bar{q}) + 2\sigma(qq)
\end{array}$$

Thus we have the cross-section for a spectator at (1-x_1) of a given charge as:

$$\sigma(+) = P(u\bar{u})P(\bar{u})\sigma(\bar{u}p) + P(d\bar{d})P(d)\sigma(dp)$$

$$\sigma(-) = P(u\bar{u})P(u)\sigma(up) + P(d\bar{d})P(\bar{d})\sigma(\bar{d}p)$$

However, when the spectator system recombines into the observed hadrons we must weight the cross-section formulae by the magnitude of the charge that the spectator system contributes at

$(1-x_1)$. If we write this as $w(q)$ (ie, the average charge of the specatator system from quark (q), then, <u>either</u> the quark dresses into hadrons with integral average charge (± 1), in which case $w(u)=w(d)=1$ <u>or</u>, as the EMC collaboration implies, the original charge of the quark should be preserved, in which case $w(u)=\frac{2}{3}$ and $w(d)=\frac{1}{3}$. Consequently, we rewrite our cross-sections:

$$\sigma(+) = P(u\bar{u})P(\bar{u})\sigma(\bar{u}p)w(u) + P(d\bar{d})P(d)\sigma(dp)w(\bar{d})$$

$$\sigma(-) = P(u\bar{u})P(u)\sigma(up)w(\bar{u}) + P(d\bar{d})P(\bar{d})\sigma(\bar{d}p)w(d)$$

A formula can now be constructed for the average charge produced at any given $x = 1-x_1$:

$$\langle Q(x)\rangle = \frac{\sigma(+) - \sigma(-)}{N(+) + N(-)}$$

where $N(+)$,$N(-)$ are nothing more than the number of respective charges (ie, $\sigma(q)$ calculated with $w(q)=1$). Thus, we obtain the formulae:

$$\langle Q(x)\rangle = \frac{7R - 7}{9R + 21} \qquad \langle Q(x)\rangle = \frac{15R - 15}{27R + 63}$$

Integral average charge(1) Quark charge preserved(2)

where $R(x_1,x_2,s(q_1q_2))$ is the ratio of the quark-(anti)quark cross-sections for the interacting partons (with x_1 and x_2), and remains a parameter to be determined: $R = \sigma(q\bar{q})/\sigma(qq)$. These are reasonably exciting results since they state that if the cross-sections are equal then our model would imply NO asymmetry. Furthermore, the annihilation channel ensures that $R > 1$ so that the result is a positive asymmetry. However, it still remains to generate x_1 and x_2 of the interacting quarks, and to determine R as a function of x_1,x_2 and $\sqrt{s}(qq)$.

The generation of x_1 and x_2 requires some knowledge of the Structure Functions for the photon and proton respectively. Unfortunately, the photon structure function is an extremely complicated subject [3] and therefore, for the purposes of this model, it was considered reasonable to approximate with a $(1-x)$ distribution to some power. It could be suggested that some remnant of the pointlike component (dominant at high Q^2) may be present in real photoproduction ($Q^2=0$), which could contribute high x quarks. However, a previous investigation has shown no evidence of a pointlike photon in our experiment [18.2]. VMD considerations suggest a $(1-x)^1$ distribution to be reasonable, but though in principle the photon sea can contribute to our charge asymmetry, a distribution peaked more towards low x is not unreasonable. Therefore, a range of values were used ($\frac{1}{2}$ - 10).

The proton structure function has been well measured ($10<Q^2<30$ GeV^2) to be $F_2 \propto x^{0.55}(1-x)^{3.2}$ (see S61 [1]), where the quark probability density $Q(x)$ is given by $F_2=xQ$. Thus the probability of finding a valence quark in the proton in the interval x to x+dx is $Q(x) \sim (1-x)^3/\sqrt{x}$. However, F_2 may be further split into the respective quark distributions for which experiment suggests: $u(x) \sim (1-x)^3/\sqrt{x}$ and $d(x) \sim (1-x)^4/\sqrt{x}$.

The values of the parameter $R(x_1,x_2,s(q_1q_2))$ for the quark subprocesses are based upon the differences between the total cross-sections for $\sigma(p\bar{p})$ and $\sigma(pp)$. This arises through the naive assumption that the $\sigma(p\bar{p})$ could be a source for estimating the annihilation channel $\sigma(q\bar{q})$ due to the quark content and $\sigma(pp)$

for estimating the scattering $\sigma(qq)$. Continuing this, an over-simplification is to regard the cross-section at any particular $s(p_1p_2)$ as largely the result of a beam and target quark interaction, thus in the cms:

$$s(p_1p_2) = 4(\ M^2 + P^2)$$

$$s(q_1q_2) = 2m^2 + 2E_1E_2 + 2x_1x_2P^2$$

where M = proton mass, m = quark 'mass',
P = cms momentum of proton, and,
$x_{1,2}$ = fraction of proton momentum carried by quarks q_1q_2

Substituting for P^2, we obtain:

$$s(q_1q_2) = 2m^2 + 2E_1E_2 + \tfrac{1}{2}x_1x_2s(p_1p_2) - 2x_1x_2M^2$$

Interestingly, assuming massless quarks and ignoring the last term, the expression reduces to $s(q_1q_2) \sim x_1x_2s(p_1p_2)$. Therefore on average, $s(q_1q_2) \sim s(p_1p_2)/36$, or if you consider q_1,q_2 to be valons $s(q_1q_2) \sim s(p_1p_2)/9$. The program varied the quark 'mass' assuming: 0,150,300 MeV/c^2. Having generated x_1 and x_2, the above expression is used by calculating the $s(q_1q_2)$ for the quark subprocess and then taking R as the value of the ratio $\sigma(p\bar{p})/\sigma(pp)$ at the corresponding energy $s(p_1p_2)$. Obviously these ideas are open to discussion and adjustment.

Consider, for instance, that applying the same procedure of counting like and unlike flavoured quark cross-sections to $\sigma(p\bar{p})$ and $\sigma(pp)$ would result in a modification to R:

$$R \sim \sigma(p\bar{p})/\sigma(pp) \quad \rightarrow \quad \tfrac{9}{5}(\ \sigma(p\bar{p})/\sigma(pp) \ - 1\ )$$

Also the threshold $\sqrt{s}$ for $p\bar{p}$ interactions is 1.8766 GeV and so any $\sqrt{s}$ below this is unphysical. Therefore, in the model, two assumptions were made about this region: a) extrapolating the cross-section ratio, and, b) assuming a finite value. The 'unphysical' region only affected the extreme upper limit of the x range leaving the majority of points unchanged.

The effects of beam spead were incorporated into the model by generating x_1 using the known beam energy spectrum, and then, assuming the spectator to be a pion at $(1-x_1)$, boosting the particle first back to the lab and then reboosting to the cms using the nominal energy.

The discussion so far has made it clear that there is some freedom for adjusting the parameters, and also the assumptions used, so that we can apparently 'tweak' the model almost as we please. Obviously, there are more processes occurring than our annihilation diagram, for instance since VMD accounts for upwards of 80% of the total cross-section it may be argued that there would be similar numbers of u and d beam quarks available to interact. Recalculating the average charge formulae for <u>equal</u> numbers of beam quark flavours yields:

$$\langle Q(x)\rangle = \frac{R-1}{3R+9} \qquad\qquad \langle Q(x)\rangle = \frac{3R-3}{3R+9}$$

Integral Average Charge(3) Quark Charge Preserved(4)

Since diffractive ρ production has been shown to give symmetric forward charge, which is a small fraction of the 80% VMD component, we believe the major part of the asymmetry to result from the remaining (non-diffractive?) VMD component. However, there could still be some contribution to the asymmetry from the non-VMD component, since in principle we do not know what processes this accounts for.

A somewhat qualitative argument may be presented suggesting we need not know the size of the photon component resulting in the asymmetry. Suppose we interpret $P(q\bar{q})$ as the probability that the beam photon manifests itself as a quark-antiquark pair which proceeds explicitly through our diagram to produce the charge asymmetry. Arguably, this may be written $P(u\bar{u}) = \frac{4}{9}c(u)$ and $P(d\bar{d}) = \frac{1}{9}c(d)$, where $c(q)$ is some sort of constant dependent on the quark mass. Then let $P(u\bar{u}) + P(d\bar{d}) = a$ where 'a' represents the fraction of beam manifestations which proceed through our asymmetry mechanism ($0<a<1$). Assuming a similar kinematic dependence for $c(u)$ and $c(d)$, and that the similarity in quark mass allows $c(u) \sim c(d)$, then the parameter 'a' cancels in the construction of the average charge formulae. The interaction rate is effectively contained in the parameter R.

The result of running the Monte Carlo and varying all the parameters, such as the different assumptions about the photon structure function, u and d quark availability, quark 'mass' and the average charge of the hadronised spectator system, produced a series of curves which have been displayed as the band superimposed on figure 75. In order to enhance the effect, the data include all events with 3 or more charged tracks but with the 3C fits to 3 prongs removed.

There is reasonable agreement between the model and the data, in particular the rising x dependence despite the model having no transverse momentum dependence incorporated. The Pt dependence may be associated with a more tightly bound u-quark in the proton

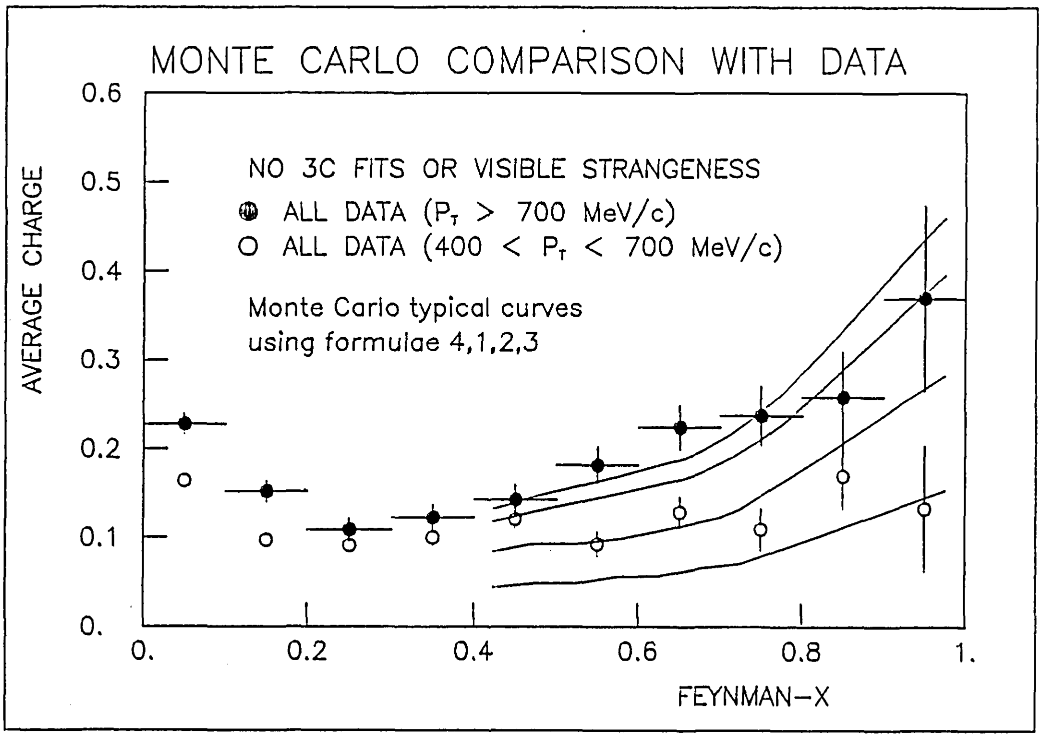

Figure 75: Comparison of Model with Data

than the d-quark, which would result in harder scattering. Also there is the possibility that charge symmetric processes (such as diffractive production) compete at low Pt by swamping any effect [78.2], or perhaps the effect does not manifest itself at low Pt. An important consequence of the model is that, assuming the rising x dependence is a genuine reflection of the increasing difference between the total cross-sections for $\sigma(p\bar{p})$ and $\sigma(pp)$ with decreasing cms energy, then a testable prediction of our model is that the asymmetry should decrease with increasing cms energy, since the low x region responsible for the asymmetry becomes progressively unable to contribute. Despite the simplicity of the model the plausibility for our interpretation to the asymmetry is established.

Finally however, it is worth mentioning the results of running a QCD Monte Carlo [79], which calculated the cross-section difference for $d\sigma(\pi^{+} - \pi^{-})/dP_{1}dPt$. This program, used by the NA14 experiment at CERN (a γp experiment with a bremsstrahlung beam of energy 50 -150 GeV), included diagrams such as 'QCD Compton', 'Photon-gluon Fusion', and many other 'leading log' contributions, but <u>not</u> our annihilation diagram. The applicability of this program to our lower energy range with correspondingly soft Pt products (Pt<1.5 GeV/c) is not clear, but nevertheless, after modifying the program for our experiment, the output suggested a small asymmetry but with the <u>wrong</u> x and transverse momentum dependence.

7.3 CHARGED KAON DISTRIBUTIONS

As discussed in chapter 5 (5.3) the x distribution is predicted to have a form $(1-x)^{n}$ with n → 1 in the beam fragmentation region (x>0.4) as x → 1, which should apply to both pions and kaons. Earlier results on the pion distributions were very encouraging with very good agreement in favour of recombination ($n \sim 1$) over fragmentation ($n \gg 1$) [18.2]. This section now reports on the charged kaon x distributions identified in the Cerenkov counters.

Figure 76 shows the geometrical acceptance of the Cerenkov counters as a function of x (integrated over Pt). This was calculated using actual data with 3 or more charged tracks and includes beam spread effects. As a consistency check a Monte

Carlo program was also written which used a 'rotation technique', wherein tracks were generated in given kinematic intervals ultimately to form a table of acceptance. Generated tracks were rotated about the beam direction and after each rotation were swum through the S.H.F and tested for reaching the Cerenkov counters (including the appropriate known PWC plane efficiencies for hybridisation). The results were then combined with the real data to obtain the expected Cerenkov sample.

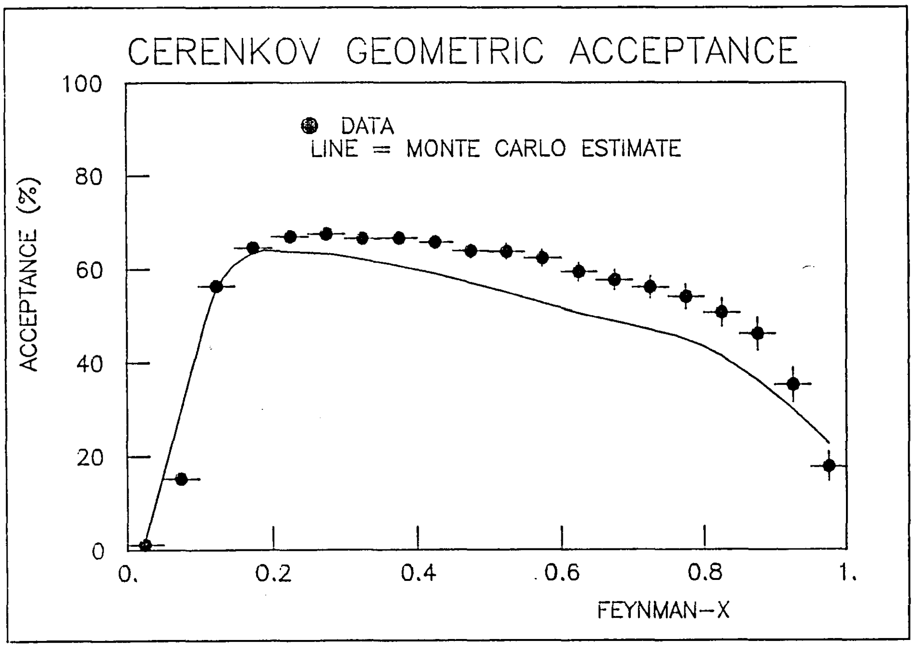

Figure 76: Cerenkov Acceptance as a function of x
This particular plot is integrated over Pt for the full data.

Corrected for acceptance, beam spread, and kaon identification efficiency (recalculated from the 3C fits) figure 77 shows the behaviour of dN(K)/dx as a function of x in the beam fragmentation region for: all kaons, those from 3 prongs, and those from high prongs (7 or more charged tracks). The results, tabulated below, are not conclusive as was the case with the earlier work on pions.

TABLE 6

Charged Kaon Power Law Behaviour

Data Sample		No Pt cut	400<Pt<700 (MeV/c)	700<Pt (MeV/c)
All data	K^+	1.46±0.03	1.44±0.01	0.98±0.04
	K^-	1.34±0.03	1.31±0.05	1.06±0.06
	K^++K^-	1.36±0.01	1.34±0.01	1.00±0.01
3 prong	K^+	0.95±0.03	0.85±0.04	0.51±0.04
	K^-	0.95±0.03	0.86±0.05	0.54±0.05
	K^++K^-	0.95±0.01	0.86±0.01	0.54±0.01
High prong	K^+	2.93±0.09	3.02±0.12	2.02±0.14
	K^-	3.76±0.18	4.02±0.29	2.84±0.34
	K^++K^-	2.75±0.01	2.79±0.02	2.13±0.02

Table quotes n from fits to:

$$dN/dx = A\,(1 - x)^n$$

with fits performed using HBOOK MINUIT [83]

The total sample indicates a power index reasonably close to, but not exactly consistent with one, however, at high Pt the agreement is excellent. It may be argued that higher Pt products in the beam fragmentation region are more likely to reflect an

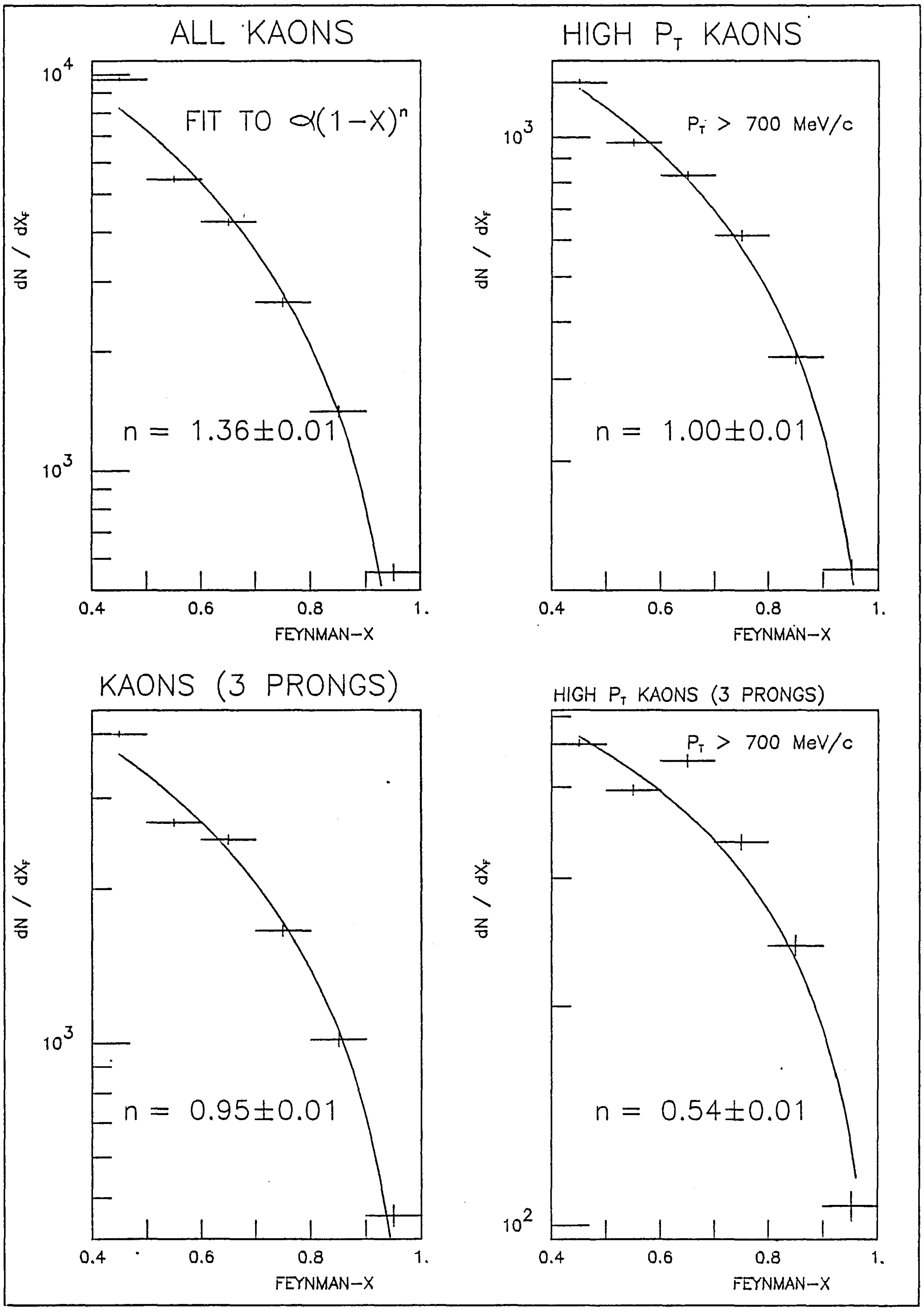

Figure 77: Forward Kaon Distributions

origin within the photon, and therefore reflect a structure function, than lower Pt products, which may be more centrally produced. To test whether this is true requires the data to be subdivided by topology, not least because the above results may be a consequence of different distributions averaging out, but also because the 3 prong sample may be expected to reflect a beam structure function more closely. Indeed, the index of the 3 prong sample is in good agreement with one, which possibly suggests another success for the recombination approach to soft processes. However, the high Pt 3 prong sample is much shallower, and furthermore, examination of the high prong sample, possibly less likely to reflect the beam structure, shows very steep distributions more in line with fragmentation ideas. Unfortunately, at the time of writing no theoretical predictions for a comparison with the behaviour of kaons were available.

The results here then are inconclusive, and although the 3 prong subsample and the total sample suggest some agreement with the recombination view, there is reason to consider this accidental. If the recombination and fragmentation models both describe QCD processes then it is reasonable to suggest both occur. It is further suggested that recombination ought to be favoured since, in a sense, it is 'quark/valon capture', a less dramatic process than fragmentation which is a catastrophic event.

7.3.1 K/K and K/π Particle Ratios

This subsection reports the K^+/K^- and K^-/π^- ratios observed in this experiment. There are several advantages in these ratios, for instance, the cancellation of the geometrical acceptance of the Cerenkov counters. Further, when plotted as a function of Pt wrt the beam direction, there are no beam spread effects.

Figure 78 shows the K^+/K^- ratio both as a function of Feynman-x and Pt, which have the added advantage that the kaon identification efficiency is the same for K^+ and K^-, and so cancels. The ratio as a function of x is everywhere greater than one, averaging ~1.6, but is increasing in the Pt distribution. This is understood as arising from associated production. A similar Pt distribution has been observed in the NA14 experiment [80]. Both results are consistent with each other, and also with the same ratio measured by Frisch et al, a 200/300 GeV/c π^-p experiment with much higher Pt ($1<Pt<6$ GeV/c)[80.2].

The K^-/π^- ratios are reported in figure 79, where the Pt plot has been cut at 300 MeV/c to minimise the effects of the Cerenkov dead region and mirror edges. Plotted as a function of x the distribution is reasonably flat at $\sim \frac{1}{8}$, and since this is the beam fragmentation region it may be argued that this suggests that the s-quark distribution within the photon is similar to the d-quark except in magnitude[38]. The Pt distribution is interesting in that it rises with increasing Pt, a trend possibly continued in the Frisch et al results, but is in conflict with the NA14 results which are approximately flat.

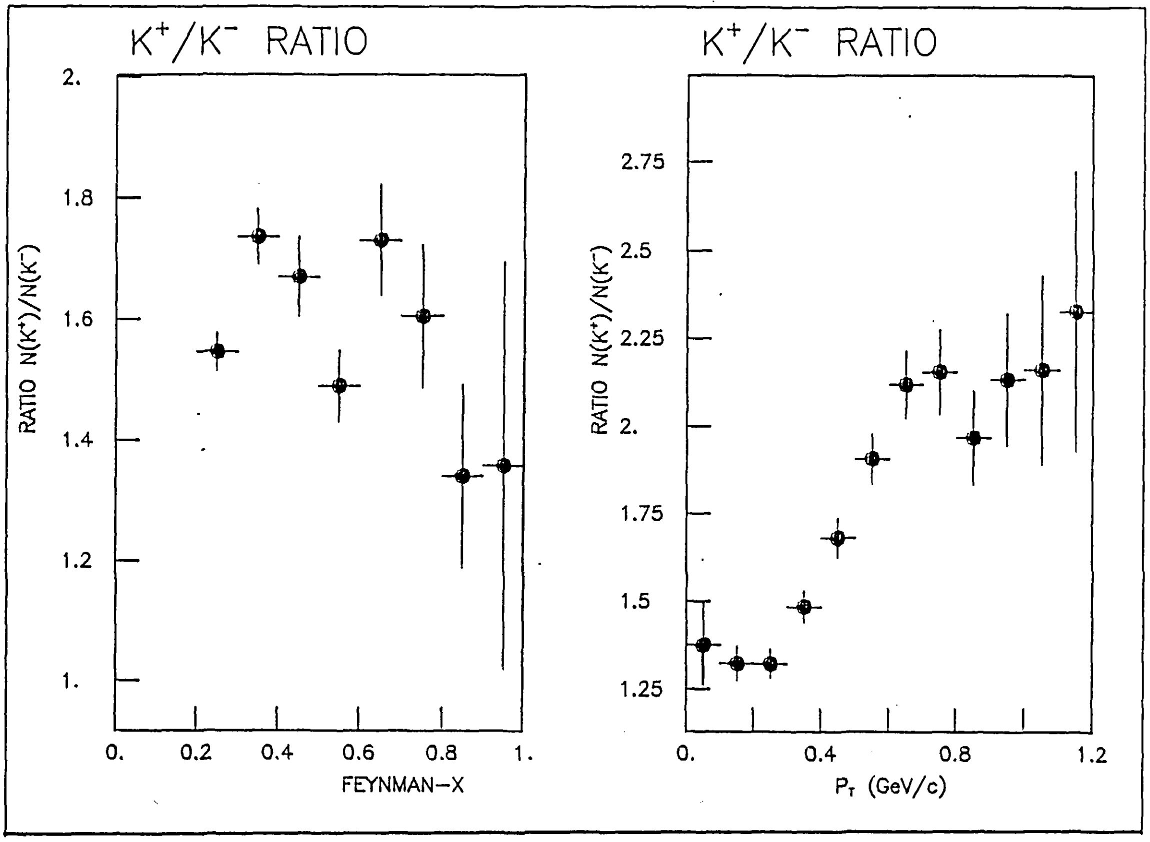

Figure 78: K^+/K^- ratios versus Feynman-x and Pt

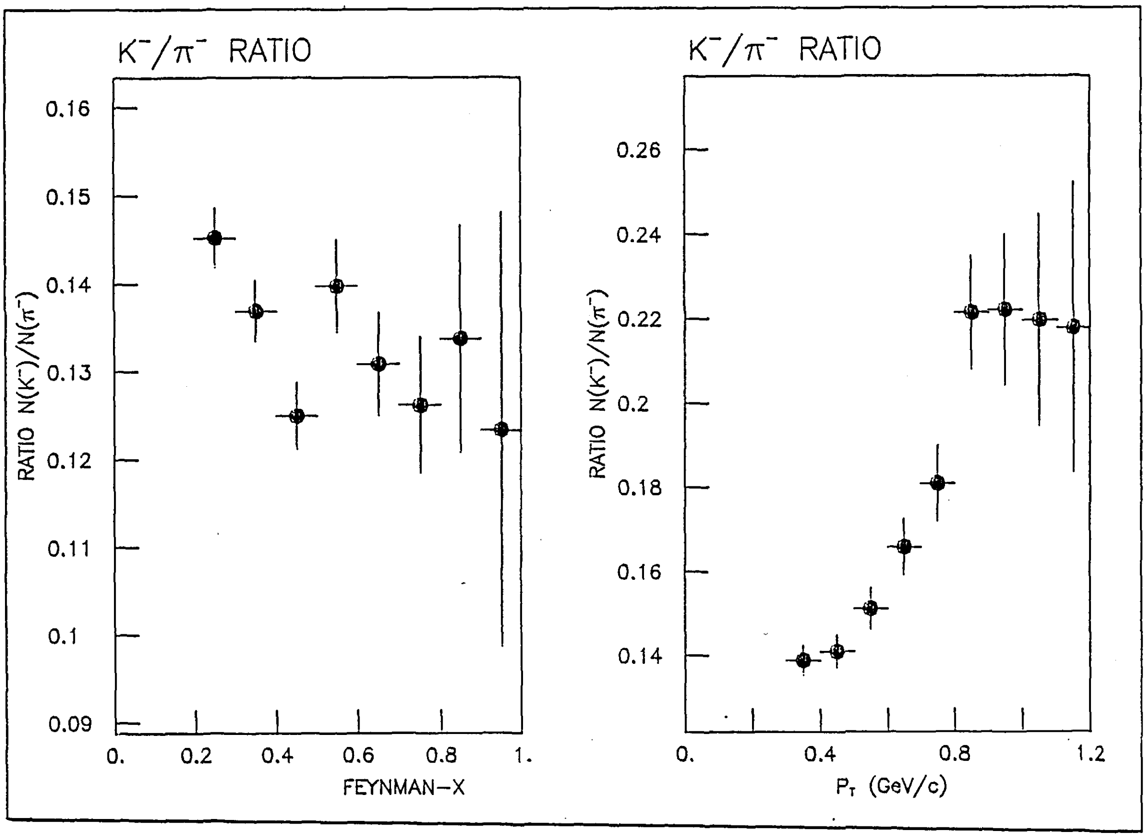

Figure 79: K^-/π^- ratios versus Feynman-x and Pt

7.4 FINAL COMMENTS: A PRELIMINARY JET SEARCH

To conclude this chapter, and this thesis, results of a search for forward jets in the beam fragmentation region are reported. This was motivated by both our observation of a forward going charge asymmetry, and also by a claim by the Omega Photon collaboration to have observed two forward jets in their beam fragmentation region [81], (at a comparable cms energy of $\sqrt{s} \sim 10.6$ GeV).

A consistent, qualitative picture of jets and parton fragmentation has been developed in e^+e^- collisions, deep inelastic scattering, and hard hadron-hadron scattering, and now there is increasing evidence for similarities between jets in soft hadronic and e^+e^- interactions when compared at the same cms energy. This may not be surprising since from VMD considerations one expects photon interactions to be similar to hadronic interactions. However, at some energy the unique pointlike component of the photon may be expected to modify distributions. In this respect, it is expected that (in the cms) "3-jet" events would occur, consisting of a backward target jet with two opposed high Pt jets in the forward region, leaving no particles in the beam direction (see figures 36 & 37). However, a similar 'background' signature would come from VMD and resonance decays.

7.4.1 A Sphericity Analysis

The procedure adopted here is a modified 'sphericity' analysis [82], where since only charged tracks were used, a full sphericity analysis was precluded. However, the Omega results indicate this to be a satisfactory approach since including neutrals did not change their results. The removal of resonances in our data (which could simulate forward jets) would be a monumental task in our data and therefore, as a first step, was not done. If an apparent jet structure had been observed then an 'iteration' on the data would have been performed to identify any obvious resonances. Further, since it is difficult to regard single charged tracks as jets, only events with 5 or more charged tracks were used (which also reduced the resonance content), giving a total sample of ~136k events.

The data were analysed on an event by event basis, in each case finding the 'Event axis' (that direction with respect to which ΣPt^2 was a minimum), and the 'Event plane' (that plane with respect to which $\Sigma Pt^2(out)$ was a minimum)[82]. The axis obtained is equivalent to the 'sphericity axis', and is distributed about the beam direction (figure 80). An alternative approach of using the beam direction is much simpler but smears the distributions in comparison to the sphericity axis. In general, the sphericity axis tended towards the beam direction. The ΣPt^2 IN the event plane and OUT of the event plane are shown to demonstrate the procedure (figure 81). The sphericity distribution peaks at ~(0.4±0.2). If there were no jets and all directions were equally probable then S→1, whereas for perfect jets all hadrons would be travelling along a given axis and S→0 [52.2].

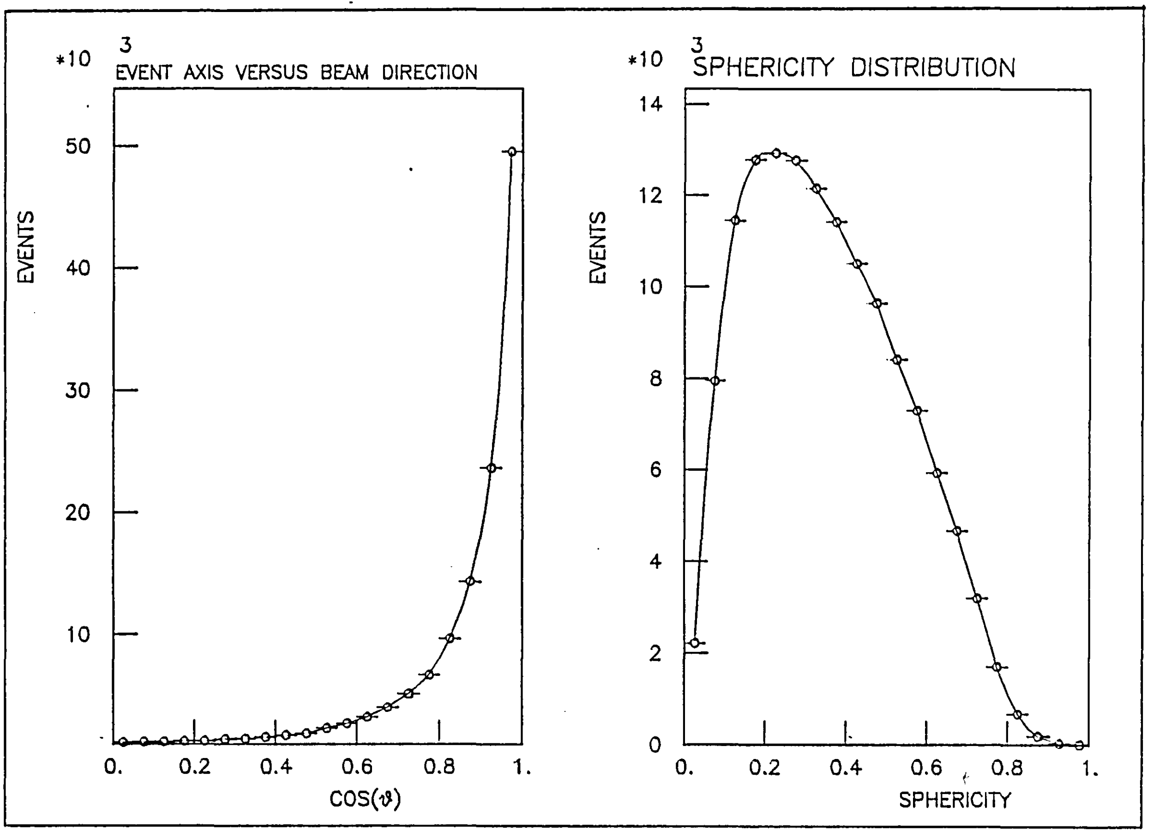

Figure 80: Sphericity axis and Sphericity Distribution
In general the sphericity axis tended towards the beam direction. Use of the beam direction as the event axis did not significantly change the following distributions nor the conclusions.

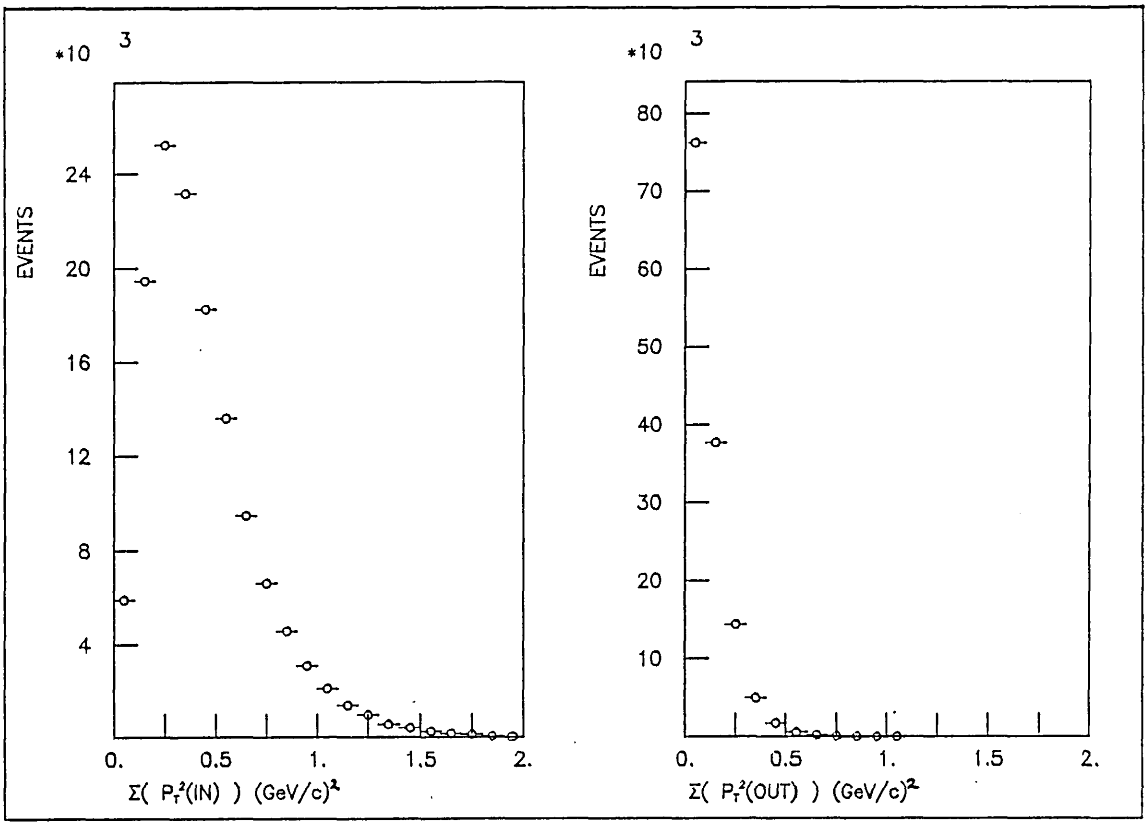

Figure 81: Sum Pt^2 IN and OUT of the Event plane

7.4.2 Results: Seagull Effect and Energy Flow

The average $\langle Pt^2 \rangle$ in the forward region is ~200 $(MeV/c)^2$ and is similar to that found in νp interactions at the same energy. This is plotted as a function of Feynman-x in figure 82, and compared to the Omega results, (which also include a comparison with K^+p interactions at a comparable energy). The data shown are for negative tracks only so as to minimise the considerable beam spread effects in the target region for the proton.

All the distributions are qualitatively the same, ie, they all show the Seagull effect quite clearly. However, the photon data differ in the region x ~ 0: the Omega (γp) data are harder than the results for this experiment, which are more in agreement with the K⁺p data. Whether this is a reflection of underlying physics is unknown, but the differences at higher x are much less significant since each experiment has different charged track multiplicities.

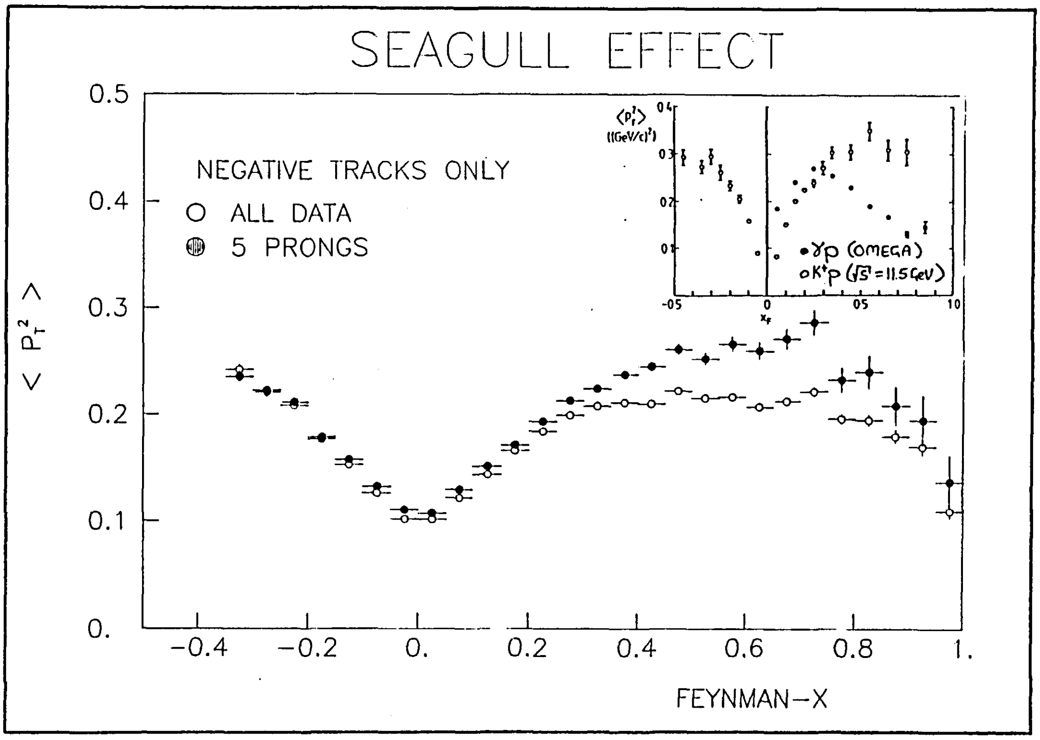

Figure 82: Seagull Effect in the x-distribution
This is for negative tracks only in this experiment.

The important plots are the distribution of tracks in the event plane about the event axis, ie, the so-called 'energy flow' plots. A true "3-jet" event (if present) should show a double-peaked structure in the forward region in these plots. The Omega collaboration made successive cuts on their data using: $\Sigma Pt^2(IN) >$ minimum, where the minimum was successively: 0 (ie, all events included), 1, 2, 3 $(\mathrm{GeV}/c)^2$, and indeed observed a double peak structure appearing stronger with each cut with a dip around $\theta=0°$.

These same 'energy flow' plots have been calculated for this experiment and are shown in figure 83, where due to the lower charged track multiplicity the statistics are lower. The plots are for cuts at 0, 1.0, 2.0 $(\mathrm{GeV}/c)^2$, and contain 100%, 34%, 0.2% of the data respectively, in comparison to the Omega plots which contained 100%, 18%, 2.6%, 0.5% for cuts at 0, 1, 2, 3 $(\mathrm{GeV}/c)^2$. Whereas Omega observed a central dip appearing with a cut as low as 1 $(\mathrm{GeV}/c)^2$, there is no evidence of such a dip in any of our data (despite the occurrence of resonances). Alongside each plot the 'planarity' of the events are shown, and as can be seen, the ΣPt^2 minimum cut is indeed selecting increasingly planar events, as required.

Assuming that beam spread has not smeared these plots, then, these plots demonstrate that there is no evidence for a two jetlike structure in the forward beam fragmentation region, which could have been ascribable to either resonance background, or indeed the QCD Compton effect [74]. Also, our observed forward charge asymmetry cannot be linked to any kind of 'jet' production. If there are genuine three-jet events in the data then either they are overwhelmed by the general hadronic production and/or the 'plumes' of any jets may be so wide such that they overlap and merge to become indistinguishable.

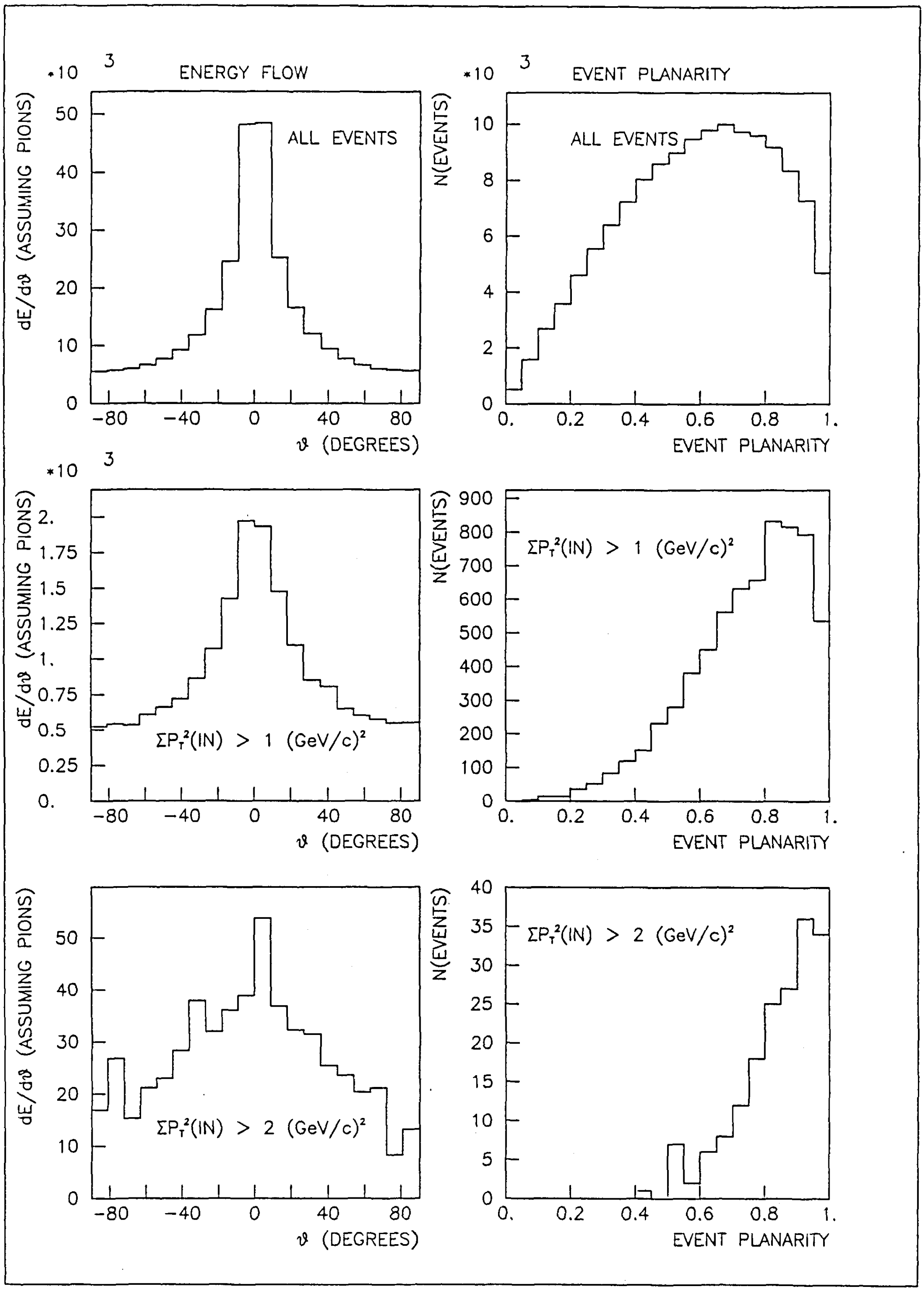

Figure 83: Forward Energy flow and Event Planarity

Appendix A

PHOTON BEAM PRODUCTION

Consider the incident laser photon beam scattering off the LINAC electron beam.

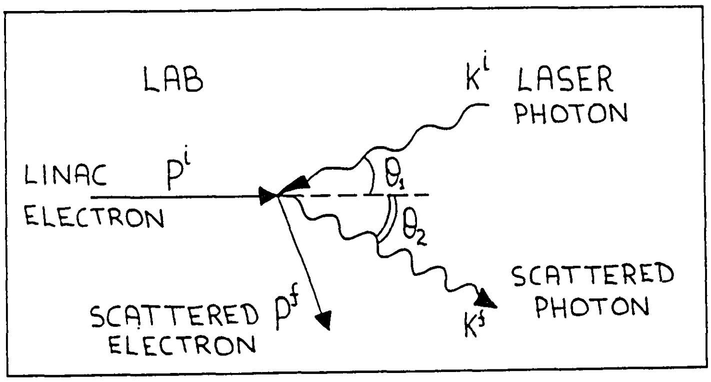

Figure 84: Electron Photon Collision

where

P = (E,p) initial 4-momentum of incoming electron mass m

P'= (E',p') final 4-momentum of scattered electron

K = (k,k) initial 4-momentum of incoming laser photon

K'= (k',k') final 4-momentum of scattered photon

and $S = (P+K)^2 = m^2 + 2Ek - 2pk\cos\alpha$ (centre of mass energy)

Conservation of energy and momentum requires:

$$P + K = P' + K'$$

$$\Rightarrow P' = P + K - K'$$

$$\Rightarrow (P')^2 = (P+K)^2 - 2K'(P+K) + (K')^2$$

but $(K')^2 = 0$ and $(P')^2 = m^2$ so

$$m^2 = S - 2K'(P+K)$$

$$\Rightarrow\ S - m^2 = 2K'P + 2K'K$$

$$= 2(k'E - \underline{k}'.\underline{p}) + 2(k'k - \underline{k}'.\underline{k})$$

now $\underline{k}'.\underline{p} = k'p\cos\theta_2$, and $\underline{k}'.\underline{k} = -k'k\cos(\theta_1+\theta_2)$

$$\Rightarrow\ S - m^2 = 2k'E - 2k'p\cos\theta_2 + 2k'k + 2k'k\cos(\theta_1+\theta_2)$$

which rearranged gives:

$$k' = (S - m^2) / 2[E - p\cos\theta_2 + k(1 + \cos(\theta_1+\theta_2))]$$

Now for k' to be a maximum (as in our experiment) we require:

a) S to be a maximum (which requires $\theta_1 \rightarrow 0$)

b) the denominator to be a minimum (which requires $\theta_2 \rightarrow 0$), so

$$\boxed{k'\ (max) = (S - m^2) / 2(E - p + 2k)}$$

However, with $\theta_1=\theta_2=0$, and since $E^2 \gg m^2$ then $p \sim E$ and $S \simeq m^2 + 4kE$. Further, using the binomial theorem $E-p \simeq m^2/2E$ so that:

$$\boxed{k'\ (max) = 4kE^2 / (m^2 + 4ke) \quad \simeq 4kE^2S^{-1}}$$

In our experiment:

E = LINAC electron beam energy ~30 GeV

k = laser photon beam energy ~4.68 eV

⇒ k' (max) = 20.48 GeV !!

It is interesting to note that in the rest frame of the incident electron beam the laser photon has energy ~0.55 MeV. Also, the accelerating electron beam perceives the two mile long LINAC as only about 20cm long!

Appendix B

CONSERVATION OF PHOTON SPIN IN PHOTOPRODUCTION

The interested reader is referred to Schilling et al[50] for the theoretical derivation of the following results.

The decay of ϕ mesons (or any vector meson) produced by linearly polarized photons is described by nine independent, measurable spin density matrix elements ρ_{ij} :

$$W(\cos\theta,\phi,\Phi) = W^0(\cos\theta,\phi) - P(\gamma)\cos2\Phi W^1(\cos\theta,\phi)$$

$$- P(\gamma)\sin2\Phi W^2(\cos\theta,\phi)$$

where

$$W^0 = 3/4\pi \ \{ \tfrac{1}{2}(1-\rho^0_{00}) + \tfrac{1}{2}(3\rho^0_{00}-1)\cos^2\theta - \surd(2)\mathrm{Re}\rho^0_{10}\sin2\theta\cos\phi$$

$$- \rho^0_{1-1}\sin^2\theta\cos2\phi \ \}$$

$$W^1 = 3/4\pi \ \{\rho^1_{11}\sin^2\theta + \rho^1_{00}\cos^2\theta - \surd(2)\mathrm{Re}\rho^1_{10}\sin2\theta\cos\phi$$

$$- \rho^1_{1-1}\sin^2\theta\cos2\phi \ \}$$

$$W^2 = 3/4\pi \ \{\surd(2)\mathrm{Im}\rho^2_{10}\sin2\theta\sin\phi + \mathrm{Im}\rho^2_{1-1}\sin^2\theta\sin2\phi \ \}$$

and where the angles are as defined in section 5.2.2. The incident photon has helicity ±1 and therefore, if the produced vector meson is also 'transverse' (ie helicity ±1) and linearly polarized as the incident photon, then there will be only two non-vanishing matrix elements in W, ie those that do not involve helicity flip:

$$\rho^1_{1-1} = -\mathrm{Im}(\ \rho^2_{1-1}\ ) = \tfrac{1}{2}$$

Consequently W reduces to

$$W(\cos\theta,\psi) = 3/8\pi \ \sin^2\theta \ (\ 1 + P(\gamma)\cos2\psi\ )$$

where $\psi = \phi - \Phi$ (as defined in section 5.2.2 see figure 39)

In general, it is necessary to calculate the ρ_{ij} in the rest frame of the ϕ (or whatever vector meson is under study) according to the following three frames to determine in which the spin properties of the photon are conserved. In each frame the y-axis is always chosen to be normal to the production plane whereas the choice of z depends on the model assumed for ϕ photoproduction (ie, where the photon spin is conserved), see figure 85 [51]:

a) Helicity frame (s-channel) If the vector meson is produced via an SCHC mechanism then z should be chosen to be the direction of V in the V rest frame. (In practise the direction opposite to the recoil proton is easier to use).

b) Gottfried-Jackson frame (t-channel) A TCHC mechanism would choose z as the direction of the incident γ in the V rest frame.

c) Adair frame (Overall γp CM) If it is the total CM spin which is conserved then z should be chosen as the direction of the γ in the overall CMS.

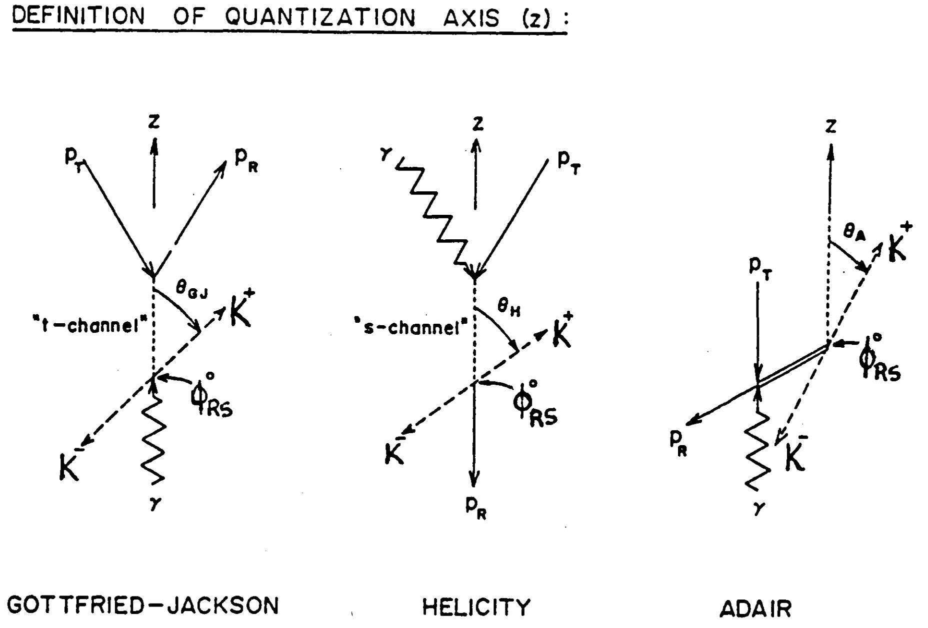

Figure 85: Frames for Photon Spin Studies

REFERENCES

1. Particle Physics Data Book (1984 edition)
Rev.Mod.Phys 56 No2 Part II (April 1984)
D.H.Perkins "Introduction to H.E.N.P" (1982)
"An Introduction to Quarks & Partons"
F.Close, Academic Press(1979)

2. "Gauge Theories in Particle Physics"
Aitchison & Hey, Adam-Hilger(1982)

3. W.Bardeen Fermilab-Conf-84/133-T(Dec 1984)
Busenitz and Sullivan, Phys.Rev.D,24,1794(1981)
Also see [40].

4. Bauer,Spital,Yennie and Pipkin Rev.Mod.Phys.50,261(1978)
"Photon-Hadron Interactions"
R.P.Feynman, Benjamin Inc.(1972)

5. Feynman Phys.Rev Lett 23,1415 (1969)

6. Andersson et al.: Phys.Lett. 69B 221; 71B 337 (1977)
Das and Hwa. Phys.Lett. 68B, 459 (1977)
Capella et al.: Phys.Lett. 81B 68; 93B 146 (1979)
Cohen-Tannoudji et al.: Phys.Rev.D 21, 2699 (1980)

7. W.Bacino et al.: Phys.Rev.Lett 45,329(1980)
R.H.Schindler et al.: Phys.Rev D24,78(1981)

8. Ph.D Thesis Carol Woods, Imperial College, 1984.

9. H.Rubinstein and L.Stodolsky, Phys.Lett.76B,479(1978)
SHF Photon Collaboration, Phys.Rev.D30,694(1984)

10. List of BC72/73/75/76 Journal Publications:
    1) Physical Review Letters 48,(1982) 1526
    2) Nuclear Instruments and Methods 203,(1982) 159
    3) Nuclear Instruments and Methods 203,(1982) 223
    4) Physical Review Letters 51,(1983) 156
    5) Physical Review 29D,(1984),1877
    6) Physical Review 30D,(1984),1
    7) Nuclear Instruments and Methods 221,(1984) 330
    8) Physical Review 30D,(1984),694
    9) Physical Review Letters 53,(1984) 751
    10) Physical Review D32, 2288 (1985)
    11) Physical Review D32, 2869 (1985)
    12) Physical Review D33, 1 (1986)
    13) Charge asymmetry: to be submitted to Physics Letters.

References

11. SLAC Energy Doubled Mode 1
Z.D.Farkas et al.: SLAC Pub 1453
IEEE Trans. Nucl. Sci NS-22 1299 and NS-24 1827 (1975)

12. Ph.D thesis Joel Kent, Berkeley, California (1983)
BC72/73 Beam Operator's Manual

13. Original concept of bubble chamber
D.A.Glaser Phys.Rev.87,667 (1952)
Hybrid Bubble Chamber Systems
J.Ballam & R.D.Watt SLAC-PUB 1954 (June 1977)

14. J.D.Ferrie & R.C.Field: Nucl.Inst & Methods 221(1984),330

15. R.C.Field et al.: Nucl.Inst. & Methods 200,237 (1982)

16. J.E.Brau et al.: Nucl.Inst & Methods 196,403 (1982)
Ph.D Thesis A.P.T Palounek Duke University, USA (1984)

17. D.O.Caldwell et al,:Phys.Rev.Lett 40,1222(1978)

18. J.T.Carroll et al.: SLAC-PUB 2726. CERN 81-07 17 July 1981.
Ph.D Thesis P.Rankin Imperial College London (1982)

19. D.Price et al.:IEEE Trans.Nucl.Sci. NS-32, 1313 (1985)

20. Hough Powell Device: CERN Yellow Report CERN 68-4

21. Reconstruction program: 'HYDRA Geometry' CERN program library. See CERN Report 71-6 by P.Villemoes.

22. G.Hall, IC-HENP/P.N/27 (1975) "Fast track fitting"
G.Hall, SHF Memo #27 (1976)

23. Kinematic fitting program GRIND: 'GRIND' CERN TC program library. Also Rutherford KINEMATICS.

24. D.J.M.Davies et al.: NIM 82, 54 (1970)

25. Berge,Solmitz and Taft, Review Sci. Inst. 32(1961),538
The stretch on a quantity X is given by:

$$S = (Xm - Xf) / \sqrt{(\text{error on } Xm)^2 - (\text{error on } Xf)^2}$$

where: Xm = measured value, Xf = fitted value

26. Ph.D Thesis I.M.Godfrey Imperial College (in preparation)

27. Derenzo & Hildebrand: Nucl.Inst. & Methods 69(1969),287
H.Geiger & A Werner: Zeit.F.Phys. 21,187 (1924)

28. Physical Review D33, 1 (1986)

29. M.J.Harwin, "ICSUMX" Internal I.C. H.E.N.P Memo (June 1984)

References

30. Cerenkov Radiation first studied by Mallet (1920s).
Cerenkov,(1934-1938), Phys.Rev 52,378(1937)
More recent references:
"Cerenkov Radiation" by J.V.Jelley(1958)
Litt and Meunier, Ann.Rev.Nucl.Sci. 23,1(1973)
Fabjan and Fischer, CERN-EP/80-27 (1980)
"Formulae and Methods in Experimental Data Evaluation"
Vol 2*,E1-E42 by Allison and Wright (August 1983)

31. Also see Jelley (1958).

32. A.V.Bevan et al.: Nucl.Inst. & Methods 200,159 (1982)

33. "CERSIM" written by G.Hall, IC/HENP/PN/13(1980)

34. M.J.Harwin Internal BC75 Note#34

35. G.Hall,V.Bevan Internal BC72/73 Note#122

36. V.Bevan Internal BC72/73 Note#218

37. Original subroutine written by G.Hall BC Note#185

38. Discussions with Dr.P.Rankin (SLAC June1984)

39. M.J.Harwin Internal BC75 Note#45

40. E.Witten, Nucl.Phys.B120(1970),189
C.Llewellyn-Smith Phys.Lett. 79B (1978),83

41. E.Paul, CERN-EP/85-130 (August 1985)

42. J.Ballam et al.: Phys.Rev.D5(1972),545

43. F.Gillman et al.: Phys.Lett 31B(1970),387

44. Okubo: Phys.Lett 5,165(1963)
Zweig: CERN Report 412 (1964) unpublished
D.Cohren et al.: Phys.Rev.Lett.38(1977),269

45. Behrend et al.: Nucl.Phys.B144(1978),22

46. The Optical Theorem relates the imaginary part of the forward elastic scattering amplitude to the total cross section:
$\mathrm{Im}A(0)\ (AN \rightarrow AN) = \surd(16\pi)^{-1}\ \sigma(AN)(\mathrm{total})$
which implies that
$d\sigma/dt\ (t=0)\ (\gamma p \rightarrow Vp) = (4\pi a/(16\pi\gamma_V^2))(1+\eta^2)\sigma^2(Vp)(\mathrm{total})$
where η is the ratio of the real to imaginary part of the forward scattering amplitude.

47. SHF Photon Collaboration, Phys.Rev.Lett.53(1984),751

References

48. Lipkin, Phys.Rev.Lett 16(1966),1015
    Joos, Phys.Lett. 24B(1967),103

49. 1965 CERN Easter School for Physicists

50. Schilling,Seyboth,Wolf, Nucl.Phys.B15(1970),397

51. Ph.D Thesis, K.Moffeit,Berkeley,California(1970)

52. Fialkowski & Kittel, Rep.Prog.in Physics 46(1983),1283
    Collins & Martin, Rep.Prog.in Physics 45(1982),335
    T.C.Bacon, Lectures at RAL School for Physicists (1978)
    Also see: (ACCMOR) MPI-PAE/Exp.El.143 (Nov 1984)

53. Anisovich & Shekhter, Nucl.Phys.B55(1973),455

54. Brodsky & Farrar Phys.Rev.Lett 31(1973),1153
    J.Gunion SLAC-PUB-2491(1980)

55. Goldberg, Nucl.Phys.B44,149(1972)
    Ochs, Nucl.Phys.B118,397(1977)

56. Takasugi et al.: Phys.Rev.D20(1979),211

57. Chang & Hwa, Physics Letters 85B(1979),285

58. Anisovich et al.: Phys.Lett.102B(1981),357
    Nucl.Phys.B133(1978),477

59. Hwa, Phys.Rev,D22(1980),759
    Hwa & Zahir, Zeit.Phys,C20(1983),27
    Chang & Hwa Phys.Lett.85B(1979),285
    Phys.Rev.Lett.44(1980),439
    Phys.Rev.D23(1981),728,439
    Chang et al.: Phys.Rev.D24(1981),1878

60. Frazer & Gunion, Phys.Rev.D20(1979),147
    Also see reference [18.2].

61. Buschbeck et al.: Zeit.Phys.C3,397(1979)
    Buschbeck et al.: Zeit.Phys.C7, 83(1980)

62. R.M.Egloff et al.: Phys.Rev.Lett 43,657(1979)
    C.Berger et al.: Phys.Lett 39B,659(1972)
    R.L.Anderson et al.: Phys.Rev.Lett 30,149(1973)
    J.Ballam et al.: Phys.Rev D7,3150(1973)
    H.J.Besch et al.: Nucl.Phys B70,257(1974)
    H.J.Behrend et al.: Nucl.Phys.B144,22(1978)
    D.P.Barber et al.: Phys.Lett 79B,150(1978)
    (OMEGA WA4) D.Aston et al.: Nucl.Phys.B172,1(1980)
    : Nucl.Phys.B179,215(1981)
    (OMEGA WA57) M.Atkinson et al.: CERN-EP/85-170 (Oct 1985)

63. J.D.Jackson Il Nuovo Cimento 34,1644(1964)

References

64. Internal BC72/73 Note#330 (July 1983)
Formulae: Phys.Rev.Lett. 10,75(1963)
Also see reference [12.1].

65. FOWL: CERN Computer Library Long-Write-Up W505 (1968)
F.James CERN 68-15 (May 1968)

66. E.Byckling & K.Kajantie "Particle Kinematics"
Pub John Wiley ISBN 0 471 12885 6

67. Skjeggestad et al.: Volume II CERN 64-13 (Feb/May 1964)
Drijard et al.:CERN/EP 84-15 (February 1984)

68. Example references:
J.Perrier: SLAC-PUB-3436 (SLAC 1984)
S.Lindenbaum: BNL-34592 (Brookhaven Nat.Lab. 1984)
F.Close: CERN Courier,6,Jan/Feb(1984)
Fredriksson et al: Phys.Rev.Lett 51,2179(1983)

69. Various background distributions are possible, including:

a) An n'th order polynomial, or

b) A so called "Weeble":
$BG(m) = A.(m-m_0)^B.\exp(C.(m-m_0))$ where m_0 = threshold mass and A,B,C are parameters to be determined,

c) A third possibility:
$BG(m) = A.V^B.(1 - V)^C$ where $0 < V < 1$ (covering the mass range) and A,B,C are parameters to be determined.

Difficulties encountered with a polynomial led to the use of the Weeble.

70. G.Kalmus, J.Phys.43,Suppl.12,C-3,431(1982)
R.Klanner: XXII International Conference on High Energy Physics Leipzig July 19-25 1984

71. (CLEO) A.Chew et al.: Phys.Rev.Lett 51,634(1983)
(ARGUS) H.Albrecht et al.: Phys.Lett 153B,343(1985)
(TASSO) M.Althoff et al.: Phys.Lett.B136,130(1984)
(ACCMOR) R.Bailey et al.:CERN-EP 84-18 (February 1984)
(OMEGA WA4) D.Aston et al.:Nucl.Phys.B189,205(1981)
D.Aston et al.:Zeit.Phys.C17,1,(1983)

72. F.E.Close & H.J.Lipkin, Phys.Rev.Lett 41,1263(1978)

73. Talk presented by V.R.O'Dell (Brown University USA)
Summarized: Internal BC72/73 Note#355

References

74. The 'QCD Compton' effect has been calculated to be too small to explain our asymmetry (<10nb)
Private communications P.Rankin (1985)

75. K.Braune Internal BC72/73 Note#345 (January 1984)
Monte Carlo program written by K.Braune (SLAC).
P.Soding: Phys.Lett 19,702(1966)

76. Ph.D thesis, S.Wolbers, University of California (1984)
Also: S.Wolbers.SLAC-PUB-3634(1985)

77. (EMC) J.P.Albanese et al.: CERN-EP/84-63 (May 1984)

78. Concepts motivated by G.Yost (Berkeley) 1985
Private communications G.Yost (1985)

79. The NA14 Monte Carlo (called 'QCD') has, to the best of knowledge, not been published but is based on a QED program written by:
P.Aurenche et al.: Z.Phys C 24 (1984) 309
My thanks to Dr.Chris Seez for his help in running the program.

80. Ph.D Thesis J.Dixon Imperial College (in preparation)
Also see:
(Fermilab E258) Frisch et al.:Phys.Rev.D27,1001(1983)
Boyarski et al.:Phys.Rev.D14,1733(1976)

81. (OMEGA WA57) M.Atkinson et al.: Zeit.Phys.C26,19(1984)

82. To measure the "jettyness" of an event, e^+e^- experiments have constructed the 'sphericity' variable. The direction of a jet $\underline{J}$ is found by minimising Pt wrt $\underline{J}$ and maximising P_l wrt $\underline{J}$ in the cms:

$$\text{sphericity} = \text{minimum } (\underline{J})\ \tfrac{3}{2}.(\Sigma Pt^2)/(\Sigma P_l^2)$$

also,

$$\text{planarity} = (\Sigma Pt^2(\text{in}) - \Sigma Pt^2(\text{out}))\ /\ (\Sigma Pt^2(\text{in}) + \Sigma Pt^2(\text{out}))$$

My thanks to Fereidoun Hamisi (Imperial College) for his help and advice in writing the jet analysis program.

83. Programming packages:
1) HBOOK User Guide CERN Program Library Y250
2) HPLOT User Guide CERN Program Library Y251
3) MINUIT User Guide CERN Program Library D506
4) SUPADRAW User Guide G.Hall Imperial College
5) IOPACK User Guide CERN Program Library Z300
6) All Ph.D software was written in FORTRAN
and ran on an IBM 4341 running CMS under VM

SLAC Hybrid Facility Photon Collaboration

K.Abe[g], R. Armenteros[f†], T.C. Bacon[c], J. Ballam[f], H.H. Bingham[i], J.E. Brau[j], K. Braune[f], D. Brick[b], W.M. Bugg[j], J.M. Butler[f], W. Cameron[c], H.O. Cohn[d], D.C. Colley[a], G.T. Condo[j], P. Dingus[i], R. Erickson[f], R.C. Field[f], B. Franek[e], R. Gearhart[f], T. Glanzman[f], I. M. Godfrey[c], J. J. Goldberg[f]‡, G. Hall[c], E.R. Hancock[e], H.J. Hargis[j], E.L. Hart[j], M. J. Harwin[c], K. Hasegawa[g], M. Jobes[a], T. Kafka[h], G.E. Kalmus[e], D.P. Kelsey[e†], T. Kitagaki[g], W.A. Mann[h], R. Merenyi[ho], R. Milburn[h], K.C. Moffeit[f], J.J. Murray[f], A. Napier[h], V.R. O'Dell[b], P. Rankin[f], H. Sagawa[g], J. Schneps[h], S.J. Sewell[e], J. Shank[i], A.M. Shapiro[b], J. Shimony[j], K. Tamai[g], S. Tanaka[g], D. A. Waide[a], M. Widgoff[b], S. Wolbers[i◇], C.A. Woods[c♯],. A. Yamaguchi[g], G.P. Yost[i], H. Yuta[g]

a. Birmingham University, Birmingham, B15 2TT, U.K.
b. Brown University, Providence, Rhode Island, 02912
c. Imperial College, London, SW7 2BZ, U.K.
d. Oak Ridge National Laboratory, Oak Ridge, Tennessee, 37830
e. Rutherford Appleton Laboratory, Chilton, Didcot, Oxon OX11 OQX, U.K.
f. Stanford Linear Accelerator Center, Stanford University, Stanford, California, 94305
g. Tohoku University, Sendai 980, Japan
h. Tufts University, Medford, Massachusetts, 02155
i. University of California, Berkeley, California, 94720
j. University of Tennessee, Knoxville, Tennessee, 37996

---

[*] Work supported in part by the Department of Energy, contract DE-AC03-76SF00515, the Japan-U.S. Co-operative Research Project on High Energy Physics under the Japanese Ministry of Education, Science and Culture; the UK Science and Engineering Research Council; the U.S. National Science Foundation.

† Present address: CERN, Geneva, Switzerland

‡ On leave from Technion-Israel Institute of Technology, Haifa, Israel

♯ Present address: Langton EPS, London, England

o Present address: The Analytical Sciences Corporation, Reading, MA 01867

◇ Present address: FERMILAB, Batavia, IL 60510

"All other physical sciences, and probably all life sciences, must ultimately rest on the findings of elementary particle physics. It would indeed violate all our past experience in the progress of science if nature had created a family of phenomena which governs the behavior of elementary particles without at the same time establishing any links between these phenomena and the large-scale world which is built from those very particles .... We cannot afford to be ignorant of the most fundamental type of structure on which everything else depends."

... SLAC Director W.K.H. Panofsky